

**DENSITY FUNCTIONAL STUDY OF ELECTRONIC  
PROPERTIES OF MONOLAYER BLACK AND BLUE  
PHOSPHORUS**

*By*  
**AJANTA MAITY**  
**PHYS08201104010**

**Harish-Chandra Research Institute, Allahabad**

*A thesis submitted to the*  
*Board of Studies in Physical Sciences*  
*In partial fulfillment of requirements*  
*for the Degree of*  
**DOCTOR OF PHILOSOPHY**  
*of*  
**HOMI BHABHA NATIONAL INSTITUTE**



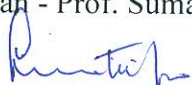
**August, 2018**

# Homi Bhabha National Institute<sup>1</sup>

## Recommendations of the Viva Voce Committee

As members of the Viva Voce Committee, we certify that we have read the dissertation prepared by Ajanta Maity entitled "Density functional study of electronic properties of monolayer black and blue phosphorus" and recommend that it may be accepted as fulfilling the thesis requirement for the award of Degree of Doctor of Philosophy.

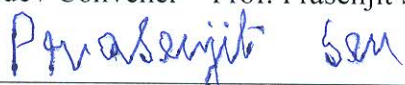
Chairman - Prof. Sumathi Rao



Date:

7/5/2019

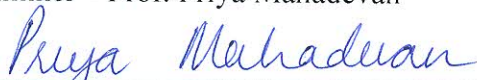
Guide / Convener – Prof. Prasenjit Sen



Date:

7/5/2019

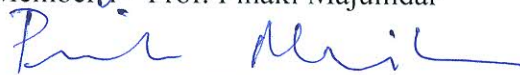
Examiner – Prof. Priya Mahadevan



Date:

7/5/19

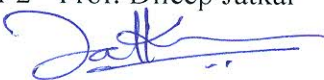
Member 1- Prof. Pinaki Majumdar



Date:

7/5/19.

Member 2- Prof. Dileep Jatkar



Date:

7/5/19

Member 3- Prof. Aditi Sen (De)



Date: 07.05.19

Final approval and acceptance of this thesis is contingent upon the candidate's submission of the final copies of the thesis to HBNI.

I/We hereby certify that I/we have read this thesis prepared under my/our direction and recommend that it may be accepted as fulfilling the thesis requirement.

Date: 07.05.2019

Place: Allahabad



Prof. Prasenjit Sen  
Guide

<sup>1</sup> This page is to be included only for final submission after successful completion of viva voce.

## **STATEMENT BY AUTHOR**

This dissertation has been submitted in partial fulfillment of requirements for an advanced degree at Homi Bhabha National Institute (HBNI) and is deposited in the Library to be made available to borrowers under rules of the HBNI.

Brief quotations from this dissertation are allowable without special permission, provided that accurate acknowledgement of source is made. Requests for permission for extended quotation from or reproduction of this manuscript in whole or in part may be granted by the Competent Authority of HBNI when in his or her judgment the proposed use of the material is in the interests of scholarship. In all other instances, however, permission must be obtained from the author.

Ajanta Maity

## **DECLARATION**

I, hereby declare that the investigation presented in the thesis has been carried out by me. The work is original and has not been submitted earlier as a whole or in part for a degree / diploma at this or any other Institution / University.

Ajanta Maity

## List of Publications arising from the thesis

### Journal

1. “Structural, electronic, mechanical and transport properties of phosphorene nanoribbons: Negative differential resistance behavior”, A. Maity, A. Singh, P. Sen, A. Kibey, A. Kshirsagar, D. G. Kanhere, *Phys. Rev. B*, **2016**, *94*, 075422.
2. “Density functional study metal- phosphorene interfaces”, A. Maity, P. Sen, *Int. J. Modern Phys. B*, **2017**, *11*, 1750077

### Conference

1. “Schottky barrier height and tunnel barrier height at metal-phosphorene interface, a density functional study”, School on Nanoscale Electronic Transport and Magnetism: Fundamentals to Applications, Harish Chandra Research Institute, Allahabad, India, 22<sup>nd</sup> Feb- 3<sup>rd</sup> Mar, 2016.
2. “Study of mobility by strain engineering in monolayer black phosphorus”, School on Topological Quantum Matter, Harish Chandra Research Institute, Allahabad, India, 09-21 Feb, 2015.

Ajanta Maity

*To my parents*



# Acknowledgments

I am thankful to Prof. Prasenjit Sen for giving me the opportunity to work with him. I express my deep gratitude to Prof. Ashoke Sen, Prof. Rajesh Gopakumar, Prof. Pinaki Majumdar, Prof. Sumathi Rao, Prof. V. Ravindran for giving me unparalleled courses on basic physics. I am grateful to HRI cluster facility which help me in doing computation. I am thankful to my parents for supporting me. Outside HRI, I am immensely grateful to my best friend Om Prakash for his encouragement and support.



# Contents

<b>Summary</b>	<b>1</b>
<b>List of Figures</b>	<b>3</b>
<b>List of Tables</b>	<b>9</b>
<b>1 Introduction</b>	<b>11</b>
1.1 Two dimensional materials . . . . .	11
1.2 Production of bulk black phosphorus . . . . .	16
1.3 Synthesis of 2D black phosphorus . . . . .	17
1.3.1 Mechanical exfoliation . . . . .	17
1.3.2 Organic-phase exfoliation . . . . .	17
1.3.3 Water-phase exfoliation . . . . .	18
1.3.4 Other synthesis routes . . . . .	18
1.4 Structural properties of black phosphorus . . . . .	18
1.4.1 Experimental crystal structural parameters . . . . .	19
1.5 Electronic band structure and tunable band gap . . . . .	20
1.6 In plane anisotropy in black phosphorus . . . . .	20
1.7 Device applications . . . . .	23
1.8 Nanoribbons . . . . .	25
1.9 Blue phosphorus . . . . .	27

1.10	Structure of the thesis . . . . .	27
<b>2</b>	<b>Methods</b>	<b>29</b>
2.1	Born-Oppenheimer approximation . . . . .	30
2.2	Density functional theory . . . . .	31
2.3	Hohenberg-Kohn Theorems . . . . .	31
2.3.1	The Kohn-Sham (KS) Equations . . . . .	32
2.4	The Exchange-correlation functional . . . . .	35
2.5	HSE06 functional . . . . .	37
2.6	The Plane wave expansion . . . . .	37
2.7	The pseudopotential theory . . . . .	40
2.7.1	Projected Augmented Wave Method (PAW) . . . . .	43
2.8	van der Waals corrections . . . . .	47
2.9	Charge carrier mobility . . . . .	49
2.9.1	Boltzmann transport theory . . . . .	49
<b>3</b>	<b>Strain engineering in mobility in monolayer black phosphorus</b>	<b>55</b>
3.1	Computational details . . . . .	56
3.2	Results . . . . .	57
3.3	Data of deformation potential, effective mass and mobility . . . . .	66
<b>4</b>	<b>Density functional study of metal/Black phosphorus interface</b>	<b>75</b>
4.1	Motivation . . . . .	75
4.2	Metal adatom on phosphorene . . . . .	77
4.3	Atomic and electronic structure of MPI . . . . .	79
4.4	SBHs at the interfaces . . . . .	83
4.5	TBHs at the interfaces . . . . .	88
4.6	Discussions . . . . .	91

<b>5</b>	<b>Phosphorene Nanoribbon</b>	<b>93</b>
5.1	Computational details . . . . .	93
5.2	Electronic structure of phosphorene and PNRs . . . . .	94
5.3	Conclusion . . . . .	104
<b>6</b>	<b>Density functional study of metal/blue phosphorene interface</b>	<b>107</b>
6.1	Computational method . . . . .	107
6.2	Results . . . . .	109
6.2.1	Pristine blue phosphorene . . . . .	109
6.2.2	Metal adatom on blue phosphorene . . . . .	109
6.2.3	Atomic and electronic structure of metal/blue phosphorene interface . . . . .	112
6.2.4	Schottky barrier height at metal/blue phosphorene interface . . . . .	115
6.2.5	Tunnel barrier height at metal/blue phosphorene interface . . . . .	120
6.3	Discussion . . . . .	121
6.4	Conclusion . . . . .	121



# Summary

Over past several years two dimensional (2D) materials have drawn attention due to their unique physical and electronic properties. Being the thinnest material, graphene shows extraordinary properties. Although the carrier mobility of graphene is very large ( $2,00,000 \text{ cm}^2/\text{V.s}$ ), but it is not suitable as a channel material for lack of a band gap in its electronic structure. Thus interest arose to move beyond graphene and seek new 2D materials with an intrinsic bandgap. Transition metal dichalcogenides (TMDC) have attracted attention due to their sizable band gaps. Phosphorene, the recently exfoliated monolayer of bulk black phosphorus (BP), seems to be a promising candidate in electronic applications. BP, one of the three main allotropes of phosphorus, is thermodynamically the most stable.

A phosphorus atom has five electrons in its 3p orbitals. In phosphorene each phosphorus atom is covalently bonded with three other phosphorus atoms leaving one lone pair. Phosphorene shows anisotropic mechanical and transport properties.

The specific property of BP which governs the transport behavior as channel material in FETs is its carrier mobility. Although effective mass is an important factor in determining mobility, it is not the only one. Within a phonon-limited scattering model, mobility also depends on the so called deformation potential. Deformation potential describes electron-phonon interaction by calculating the shift of band edges with strain. Therefore, a proper analysis of strain engineering of mobility requires the calculation of effective mass as well as deformation potential as a function of strain.

In first principles calculations both effective mass and deformation potential depend critically on the band structure. Self interaction in the Kohn-Sham potential gives inaccurate band gap. This problem can be partially overcome by HSE06 functional by including a fraction of the Hartree-Fock non local exchange potential. Therefore we have employed HSE06 functional proposed by Heyd, Scuseria and Ernzerhof which is expected to give a better description of the electronic bands and hence mobility.

Another essential aspect of FET based devices is the interface between the semiconductor channel and metal electrodes. In the experiments performed so far on phosphorene based FETs

Ti, Cr, Ni, Pd and Au metal electrodes have been used. Behavior of metal-phosphorene interfaces depends on the metal as well as thickness of the phosphorene channel.

We have studied the metal/phosphorene interface structure and contact behavior using DFT based first principles calculations.

In addition to phosphorene nanosheet, phosphorene nanoribbons (PNR) have also been studied theoretically. The channel material used in FETs are finite in the direction of the perpendicular to the current, which gives a motivation in studying PNR. Another motivation behind studying PNR was to have an additional control over the band gap through manipulation of their width. We have studied three different types of PNR: linear, zigzag and armchair.

A new allotrope of phosphorus called blue phosphorus was predicted by Zhu et. al.. Recently it has become possible to synthesize monolayer blue phosphorus on Au(111) substrate by molecular beam epitaxy technique. We have studied the metal/blue phosphorene interface using DFT calculation.

Variation of both electron and hole mobility due to uniaxial strain along armchair and zigzag directions are studied. We have found that hole mobility is larger than electronic mobility along zigzag direction when the strain is along zigzag direction and the armchair direction is fixed. Electron mobility is larger along armchair direction than hole mobility when the zigzag direction is relaxed and strain is along armchair direction.

We have calculated Schottky barrier height and tunnel barrier height at the metal/phosphorene interface. We have chosen low index surfaces Pd(111), Pd(100), Pd(110), Au(110), Ni(110) and Ti(0001). Ti(0001)/phosphorene interface was found to be good for hole injection.

Among the linear, zigzag and armchair nanoribbons, the armchair PNR is semiconductor, while both linear and zigzag PNR are metallic. A small band gap opens up in linear and zigzag PNR after edge reconstruction.

We have studied metal/blue phosphorene interfaces and Schottky barrier height and tunnel barrier height. In this study we have chosen Pd(111), Pd(110), Pd(100), Au(110), Ni(100) and Al(111). Al(111)/blue phosphorene interface is found to be good for electron injection.

# List of Figures

- 1.1 Typical structures of layered transition metal dichalcogenides. Cleavable 2H, 1T and 1T structures in layered TMD are shown. Figure is taken from Materials Today, 20, 3 (2017) . . . . . 14
- 1.2 (a) Atomic structure of multi-layer black phosphorus and (b) monolayer phosphorene. Figure is taken from J. Mater. Chem. C, 2015,3, 8760-8775 . . . . . 19
- 1.3 Band structure of bulk black P mapped out by ARPES measurements. A band gap around 0.3 eV is clearly observed. Superimposed on top are the calculated bands of the bulk crystal. Blue solid and red dashed lines denote empty and filled bands, respectively. The directions of the ARPES mapping are along U (LZ) and T, as indicated in the first Brillion zone shown in Inset.  $E_f$  is the Fermi energy (Figure is taken from (Nat Nanotechnol 9(5):372377) . . . . . 21
- 1.4 (a) Armchair and zigzag in-plane thermal conductivities ( $k_{armchair}$  and  $k_{zigzag}$ ) of multiple BP films. Dashed lines are results of theoretical modelling. The grey error bars account for the uncertainty of SiN substrate thermal conductivity  $k_{SiN}$ , whereas the blue/red error bars do no. (b) The anisotropic ratio  $k_{zigzag}/k_{armchair}$  at different BP thicknesses. The ratio at 12-nm thickness is calculated using linearly interpolated armchair thermal conductivity from adjacent thicknesses (Figure is taken from ref.(Nature Communications 6, 1 (2015) . . . . . 22

1.5	Polar representation of the absorption coefficient and experimental extinction spectra of the 40-nm intrinsic black phosphorus film. Absorption coefficient is represented with two different interband coupling strength $\beta$ which gives different band gap value $\omega$ . Extinction spectra are obtained from FTIR spectroscopy with black phosphorus on SiO <sub>2</sub> substrate(Figure is taken from ref.(Phys. Rev. B 90, 075434) .	23
1.6	Hall mobility measured along x (armchair) and y (zigzag) direction on 8 nm and 15 nm black phosphorus film with constant hole doping concentration of $6.7 \times 10^{12}$ cm <sup>2</sup> (ACS Nano volume: 8, 4033 (2014). . . . .	24
1.7	Schematic of the device structure for determining the angle-dependent transport behavior and angular dependence of the drain current and the transconductance of a device. Device is composed of electrodes and black phosphorus film with 10 nm thickness (ACS Nano volume: 8, 4033 (2014) . . . . .	24
2.1	(a) Schematic diagram of all-electron (solid lines) and pseudoelectron (dashed lines) potentials and their corresponding wave functions. The radius at which all-electron and pseudoelectron values match is designated $r_c$ (b) Oxygen 2p radial wave function (solid line) and corresponding norm-conserving (PRL 43, 1494(1979)) (dotted line) and ultrasoft (dashed line) pseudo wave functions. The figure is reproduced from Ref. PRB 41, 7892(1990). . . . .	41
2.2	Schematic representation of the PAW transformation. The auxiliary wave function is constructed from the full wave function by subtracting the oscillatory part close to an atom and replacing it by a smooth function . . . . .	45
3.1	Structure of monolayer black phosphorus. Armchair and zigzag directions are marked . . . . .	57
3.2	Variation of band gap with strain along different direction when (a) transverse directions are fixed, (b)transverse directions are relaxed . . . . .	60

3.3	Band structure of mono-layer phosphorene under different strain conditions along the zigzag direction. . . . .	60
3.4	Variation of electron and hole effective mass with strain along different direction when transverse directions are fixed. Effective masses are calculated along the strain directions in each case. . . . .	61
3.5	Variation of electron and hole effective mass with strain along different direction when transverse directions are relaxed. Effective masses are calculated along the strain directions in each case. . . . .	61
3.6	Deformation potential of (a) electron and (b) hole along armchair direction when strain is along armchair direction and zigzag direction is fixed. . . . .	62
3.7	Deformation potential of (a) electron and (b) hole along zigzag direction when strain is along zigzag direction and armchair direction is fixed. . . . .	62
3.8	Deformation potential of (a) electron and (b) hole along armchair direction when strain is along armchair direction and zigzag direction is relaxed. . . . .	62
3.9	Deformation potential of (a) electron and (b) hole along zigzag direction when strain is along zigzag direction and armchair direction is relaxed. . . . .	63
3.10	Variation of electron and hole mobility with strain along armchair and zigzag directions while transverse direction is fixed. . . . .	65
3.11	Variation of electron and hole mobility with strain along armchair and zigzag directions while transverse direction is relaxed. . . . .	65
4.1	Metal atom on (a) top site, (b) bridge site and (c) hollow site of a phosphorene monolayer . . . . .	78
4.2	Side views of atomic structure of a phosphorene monolayer on various metal surfaces	81
4.3	DOS for metalphosphorene systems. Total and atom projected DOSs are shown. Energies are plotted relative to the Fermi energy . . . . .	82

4.4	Variation of $V_{eff}(z)$ within the Pd slab, and in the vacuum region. Value of $V_{eff}(z)$ in the middle of the vacuum region, marked by the dotted vertical line, is the vacuum level energy. Difference between the vacuum level energy and $E_f$ is the work function. . . . .	85
4.5	Location of the Fermi level in phosphorene-metal systems, and phosphorene VBM and CBM after aligning the vacuum levels. Electron and hole SBH can be inferred from these figures . . . . .	87
4.6	Location of the Fermi energy (dotted lines), and variation of the electrostatic potential for metalphosphorene systems . . . . .	89
4.7	Charge density in a plane perpendicular to the MPI. Top two layers are phosphorus atoms, the lower ones are the metal atoms . . . . .	90
5.1	Structure of monolayer phosphorene. . . . .	95
5.2	(a) Structure of a a-PNR of width 4. The arrow is the direction of periodicity. . . .	96
5.3	band structure of (a) 1 unit cell wide, (b) 2 unit cell wide and (c) 3 unit cell wide a-PNR . . . . .	97
5.4	band structure of 8 unit cell wide a-PNR . . . . .	98
5.5	Structure of (a) layer-terminated l-PNR, (b) edge reconstructed l-PNR, (c) layer-terminated z-PNR, (d) Peierls distorted z-PNR. Arrow shows the direction of periodicity. . . . .	99
5.6	band structure of (a) one unit cell (b) two unit cell and (c) three unit cell wide z-PNR	99
5.7	Isosurfaces of charge density from (a) the half-filled bands in the layer-terminated and (b) VBM and CBM of edge reconstructed z-PNR. These figures show that the charge density is localized at the edges. . . . .	100
5.8	band structure of (a) one unit cell (b) two unit cell wide l-PNR . . . . .	102
5.9	Isosurfaces of charge density from (a) the partially filled band in the layer-terminated and (b) VBM and CBM of edge reconstructed l-PNR. These figures show that the charge density is localized at the edges. . . . .	103

6.1	Monolayer blue phosphorus (a) top view, (b) side view, (c) band structure with PBE	110
6.2	The adsorption sites for metal atom on (a) bridge site, (b) hollow site, (c) top site, (d) valley site . . . . .	111
6.3	side views of blue phosphorene on different metal surfaces . . . . .	113
6.4	Density of states of metal/blue phosphorene system. Projected density of states of metal are shown. Energies are drawn with respect to Fermi system . . . . .	114
6.5	Electron and hole lateral SBH are shown in figure. Green lines are fermi level for the metal/blue P composite system, Blue and red lines are conduction band minima and valence band maxima of blue phosphorene . . . . .	117
6.6	Variation of average electrostatic potential normal to interface, black dotted line is Fermi energy and red dotted lines are showing interface . . . . .	118
6.7	Variation of average charge density normal to interface, red dotted lines are show- ing interface . . . . .	119



# List of Tables

3.1	Deformation potential while transeverse direction is fixed . . . . .	67
3.2	Deformation potential while transeverse direction is relaxed . . . . .	67
3.3	Effective mass of hole ( $m_h$ ) when strain is along x direction and y direction is fixed	67
3.4	Effective mass of electron ( $m_e$ ) when strain is along x direction and y direction is fixed . . . . .	68
3.5	Effective mass of hole ( $m_h$ ) when strain is along y direction and x direction is fixed	68
3.6	Effective mass of electron ( $m_e$ ) when strain is along y direction and x direction is fixed . . . . .	69
3.7	Effective mass of hole ( $m_h$ ) when strain is along x direction and y direction is relaxed	69
3.8	Effective mass of electron ( $m_e$ ) when strain is along x direction and y direction is relaxed . . . . .	70
3.9	Effective mass of hole ( $m_h$ ) when strain is along y direction and x direction is relaxed	70
3.10	Effective mass of electron ( $m_e$ ) along y direction and x direction is relaxed . . . . .	71
3.11	Mobility of electron ( $\mu_e$ ) in the unit $\text{cm}^2/\text{V.s}$ when transverse direction is fixed . . . . .	71
3.12	Mobility of hole ( $\mu_h$ ) in the unit $\text{cm}^2/\text{V.s}$ when transverse direction is fixed . . . . .	72
3.13	Mobility of electron ( $\mu_e$ ) in the unit $\text{cm}^2/\text{V.s}$ when transverse direction is relaxed . . . . .	72
3.14	Mobility of hole ( $\mu_h$ ) in the unit $\text{cm}^2/\text{V.s}$ when transverse direction is relaxed . . . . .	73
4.1	Strain in supercell of phosphorene along x direction ( $\epsilon_x$ ) and y direcction ( $\epsilon_y$ ) when contact is made with metal surface . . . . .	78
4.2	Adsorption energy of metal atom on phopshorene surface using different method . . . . .	79

4.3	Adsorption energy of per P atom (eV) of monolayer phosphorene on metal surfaces and the nearest metal phosphorus distance( $\text{\AA}$ ) . . . . .	81
4.4	electron schottky barrier height ( $e_{SBH}$ in eV) and hole schottky barrier height ( $h_{SBH}$ in eV) at metal/phosphorene interface . . . . .	86
5.1	Lattice constants and calculated band gaps of a-PNRs of various widths . . . . .	96
5.2	Energy gain (meV/edge dimer) and gap value (eV) for edge reconstructed z-PNRs of different widths. . . . .	97
6.1	Strain in supercell of phosphorene along x direction ( $\epsilon_x$ ) and y direction ( $\epsilon_y$ ) when contact is made with metal surface . . . . .	109
6.2	Adsorption energy of metal atom on blue P surface using different method . . . . .	111
6.3	Adsorption energy of per P atom (eV) of blue P on metal surfaces and the nearest metal phosphorus distance( $\text{\AA}$ ) . . . . .	113
6.4	electron schottky barrier height ( $e_{SBH}$ in eV) and hole schottky barrier height ( $h_{SBH}$ in eV) at metal/blue phosphorene interface . . . . .	116
6.5	Tunnel barrier height (TBH in eV) and tunnel barrier width (TBW in $\text{\AA}$ ) in metal surface/ blue phosphorene interface . . . . .	116

# Chapter 1

## Introduction

### 1.1 Two dimensional materials

Over past few years two dimensional (2D) materials are interesting research topic for their outstanding potential applications in many fields such as flexible electronics, sensing and optics, due to their desirable physical and structural properties. The transports of charge carriers, heat will be strongly confined in the 2D plane. A rich variety of electronic properties, including metals, semimetals, insulators, and semiconductors with direct and indirect bandgaps ranging from ultra-violet to infrared throughout the visible range has been exhibited. Even more, the 2D geometry has excellent compatibility with current thin film manufacture techniques in the semiconductor industry, which can facilitate the 2D materials to be integrated with traditional electronic materials, such as Si, and to be placed on various substrates. Being just one or few atoms thick, 2D materials immediately appear as the most suitable candidate to create a new generation of electronic devices.

2D materials have strong in-plane chemical bonds and weak van-der Waals coupling between the layers, which we call 2D layered materials. These layered structures provide the opportunity for the bulk counterparts to be cleaved into individual freestanding atomic layers. 2D materials can also own crystal structures of chemical bonding in three dimension (3D), which we call 2D non-layered materials. The emerging surface-assisted nonlayered materials are artificially synthesized

on a substrate via chemical vapor deposition (CVD) and epitaxial growth or assembly.

Graphene is the first among the 2D materials which has been exfoliated from graphite in 2004 [1] and has received attention due to its extraordinary properties. A series of methods were developed to prepare graphene, including mechanical exfoliation, liquid-phase exfoliation, SiC epitaxy, CVD growth, and molecular assembly.

One of the most interesting aspects of the graphene problem is that its low-energy excitations are massless, chiral, Dirac fermions[2]. In neutral graphene, the chemical potential crosses exactly the Dirac point. This particular dispersion, that is only valid at low energies, mimics the physics of quantum electrodynamics (QED) for massless fermions except for the fact that in graphene the Dirac fermions move with a speed  $v_F$  (Fermi velocity), which is 300 times smaller than the speed of light  $c$ . Hence, many of the unusual properties of QED can show up in graphene but at much smaller speeds. Dirac fermions behave in unusual ways when compared to ordinary electrons if subjected to magnetic fields, leading to new physical phenomena such as the anomalous integer quantum Hall effect (IQHE) measured experimentally[3]. The IQHE in graphene can be observed at room temperature because of the large cyclotron energies for relativistic electrons. In fact, the anomalous IQHE is the trademark of Dirac fermion behavior.

Other intriguing properties of graphene are excellent carrier mobility[4] (200,000 cm<sup>2</sup>/V.s.), stunning thermal conductivity (5300 W/m K)[5], large Young's modulus (1 TPa)[6]. Besides, graphene also exhibits large theoretical specific surface area (2630 m<sup>2</sup>/g), high optical transmittance ( $\sim 97.7\%$ ), and good electrical conductivity. Due to such excellent properties, graphene shows great application potentials in many fields, such as electronics, optoelectronics, energy storage, and conversion.

Except carbon, other elementary substances of group IVA have 2D non-layered structure, such as silicene, germanene, and stanene. But unlike graphene, the atoms of silicene and germanene are bonded with each other via  $sp^3$  hybrid orbitals, which are more stable than  $sp^2$  hybrid orbitals. They do not form a van der Waals layered structure in their bulk phase. Although they do not exist as freestanding sheets, the layered structures can still be successfully obtained. In addition

to this, the most commonly used method to synthesize silicene is the vacuum deposition on different substrates, including Ag(111)[7], Ag(110)[8], Au(110)[9], Ir(111)[10], MoS<sub>2</sub>[11], ZrB<sub>2</sub>[12], and h-MoSi<sub>2</sub>[13], with the home-built low-temperature STM. Some physical properties of silicene were predicted by theoretical calculations of structural and electronic properties[14], including quantum spin Hall effect[15, 16], ferromagnetism[17, 18], tunable thermal conductivity by germanium doping[19], and half-metallic properties[20].

Germanene can be synthesized by CaGe<sub>2</sub>-based chemical exfoliation[21] and vacuum deposition[22–24]. Germanene has properties, such as structural stability[25], half-metallic behavior[26], strong excitonic resonances[27, 28], large carrier mobility[29], Dirac features[30, 31], phonon properties in the ground state[32, 33], negative thermal expansion[34], spin-polarized electronic transport[35], controllable magnetic properties[36], infrared adsorption[37, 38], and high thermoelectricity properties in room temperature[39]. The electronic structures of silicene and germanene are quite similar to that of graphene and their charge carriers are also massless fermions. A vertical electric field is able to open a band gap in single-layer buckled silicene and germanene[40].

Stanene is composed of a biatomic layer of Sn(111), in which two triangular sublattices stack together, forming a buckled honeycomb lattice. The preparation of stanene was achieved by molecular beam epitaxy (MBE) on a Bi<sub>2</sub>Te<sub>3</sub>(111) substrate[41]. Theoretical calculation showed that stanene has interesting properties, such as tension-induced mechanical properties[42], low thermal conductivity, and diffusive nature of thermal transport[43, 44], special electronic properties (Dirac cone with zero-gap at the Fermi level and a Fermi velocity of  $v_F = 0.97 \times 10^6$  m/s)[45], topological to trivial insulating phase transition[46], giant magnetoresistance (MR)[47], superconductivity[48], quantum spin Hall effect[49], and so on.

Transition metal dichalcogenides (TMDs) have structure like zinc blende or wurtzite while layered TMDs are commonly restricted to metals in groups IV-VI and X. Depending on the coordination and oxidation state of the metal atoms, 2D layered TMDs can be semiconductors (MoS<sub>2</sub>, WS<sub>2</sub>), semimetals (WTe<sub>2</sub>, TiSe<sub>2</sub>), metals (NbS<sub>2</sub>, VSe<sub>2</sub>), and superconductors (NbSe<sub>2</sub>, TaS<sub>2</sub>). TMDs (such as MoS<sub>2</sub>, WS<sub>2</sub>, and WSe<sub>2</sub>) consist of a sandwiched structure of a transition metal layer

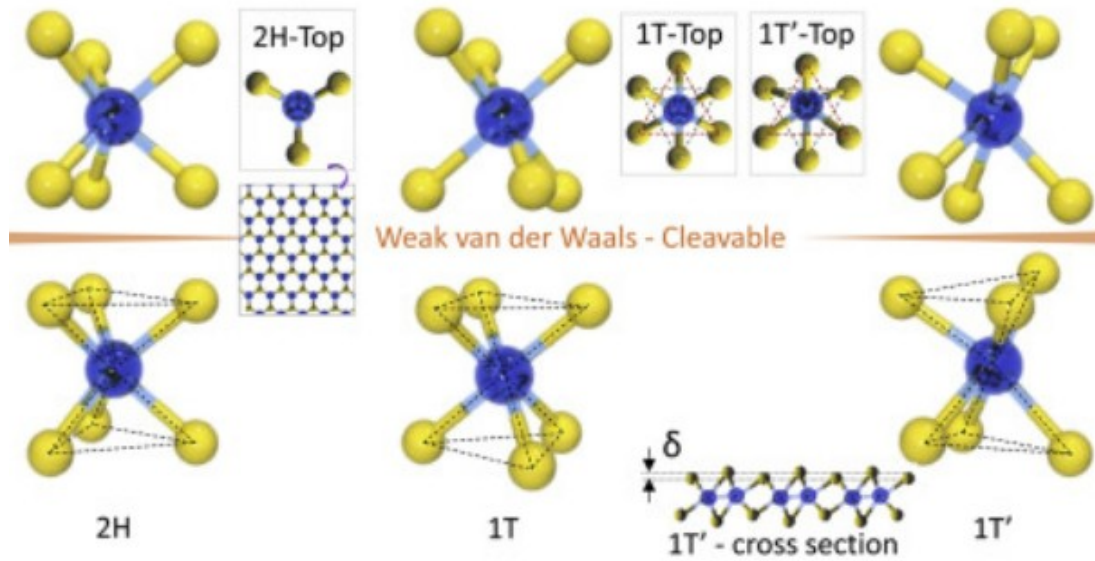


Figure 1.1: Typical structures of layered transition metal dichalcogenides. Cleavable 2H, 1T and 1T' structures in layered TMD are shown. Figure is taken from Materials Today, 20, 3 (2017)

between two chalcogen layers. Depending on the atomic stacking configurations,  $\text{MX}_2$  (M=Metal, X=Chalcogen) can form two kinds of typical crystal structures: a trigonal prismatic (2H) phase and an octahedral (1T) phase and their distorted phase (T') shown in fig.1.1. In 2H-phase of TMD, each metal atom puts six chalcogen atoms out to two tetrahedrons in +z and z directions while the hexagonal symmetry. Therefore, chalcogen-metal-chalcogen arrangement along z-direction is considered as single layer, and weak vdW interactions between layers (chalcogen-chalcogen) enable mechanical exfoliation from bulk TMDs to obtain single layer flake. T-phase has a trigonal chalcogen layer on the top and 180° rotated structure (so-called trigonal antiprism) at the bottom in a single layer and results in hexagonal arrangement of chalcogen atoms. Metal atoms are distorted further (or dimerized in one direction), called T-phase, resulting in the modification of atomic displacement of chalcogen atoms along z-direction ( $\delta$ ). 2D TMDs exhibit unique electrical and optical properties that evolve from the quantum confinement and surface effects. The tunable bandgap in TMDs is accompanied by a strong photoluminescence (PL) and large exciton binding energy, making them promising candidates for a variety of optoelectronic devices, including solar

cells, photo-detectors, light-emitting diodes, and photo-transistors. For example, unique properties of MoS<sub>2</sub> include direct bandgap ( $\sim 1.8$  eV), good mobility ( $\sim 700$  cm<sup>2</sup>/V.s), high current on/off ratio  $\sim 10^7 - 10^8$ , large optical absorption ( $\sim 10^7$  m<sup>-1</sup> in the visible range) and a giant PL arising from the direct bandgap (1.8 eV) in monolayer; thus, it has been studied widely for electronics and optoelectronics applications.

Borophene is a group IIIA elemental 2D non-layered material which is prepared by vacuum deposition[50, 51] and two zone chemical vapor deposition (CVD)[52]. Theoretical calculations indicated that borophene has the properties, such as high work function[53], magnetic properties[54], and ultrahigh hydrogen storage capacity[55]. Besides, 2D borophene has application potential in power generation, electricity transmittance, energy storage, and electric catalytic field[56, 57].

VA group elemental 2D materials include black phosphorus (BP), arsenene, antimonene, and bismuthene. Among these black phosphorus is 2D layered material. Arsenene is described as a single-atomic layer of gray arsenic with a rhombohedral structure. Arsenene has been prepared by the plasma-assisted process on the InAs substrate, and the thickness is 14 nm[58]. The theoretical calculation predicted that arsenene possesses unique properties, including highly anisotropic thermal conductivity[59] and topological phase transitions to TI via suitable strain modulation[60].

Antimonene could also be defined as the monolayer gray antimony, which is the most stable phase among all its allotropes. The preparation methods of antimonene mainly include mechanical exfoliation[61], liquid exfoliation[62], molecular beam epitaxy[63], and chemical vapor deposition[64]. Some theoretical calculations show that antimonene has some interesting properties, such as spin-orbit coupling effect[65], thermal conductivity effected by size and edge roughness[66], electronic properties influenced by Stone-Wales defects[67], and ultraviolet light absorption[68]. A small strain applied to a monolayer antimonene will lead to the transformation from the indirect bandgap to the direct one, which could further promote its application prospect in optoelectronics[69, 70].

Bismuthene is another group VA elemental material, which was first prepared on a silicon sub-

strate with atomically smooth surface in 2005[71]. Few other 2D materials are mono-chalcogenides (GaS, GaSe, ZnSe, and SnSe), tri-chalcogenides (TiS<sub>3</sub> and ZrS<sub>3</sub>), group-IV, III-V binary compounds etc.

Recently few layer black phosphorus (BP), a layered material like graphene and TMDs, has drawn attention due to its unique physical and electronic properties. The electronic bandgap of BP would increase from 0.3 to 2 eV[72] with the thickness down to monolayer. In addition, it was demonstrated that the experimental (at room temperature) carrier mobility of BP is up to 1000 cm<sup>2</sup>/V.s in few-layer quasi 2D phosphorene. The wide range of band gap by varying number of layers of black phosphorus and moderately high carrier mobility make it a potential candidate in electronic and optoelectronic applications. The production technique, structure, electronic properties and a few applications are discussed in the subsequent sections.

## 1.2 Production of bulk black phosphorus

Phosphorus can take the form of several polytypes, which fall into three allotropes; white, red, and black (BP). The low dimensional molecular structures (0D, white phosphorus) as well as the polymer structures (1D, phosphorus nanorods), the layered (2D, BP), and tubular structures (2D and 3D, crystalline forms of red phosphorus) contain covalent structure motifs that are interconnected by van der Waals interactions.

In 1914, Bridgman[73] first reported a method to convert white phosphorus to black phosphorus at a moderate temperature of 200°C and a high pressure of 1.2 GPa within 5 – 30 min. Recently Rissi et al.[74] has reported that amorphous red phosphorus could be transformed into crystalline black phosphorus at  $7.5 \pm 0.5$  GPa even at room temperature. By melting black phosphorus at a temperature of 900° C and under a pressure of 1 GPa, black phosphorus single crystals larger than  $5 \times 5 \times 10$  mm<sup>3</sup> can be synthesized, as reported in this ref[75]. Alternative techniques without using high pressure have also been developed, such as the technique involving mercury as catalyst, developed by Krebs et al.[76], the bismuth-flux-based method by Brown et al.[77], and the method

based on a chemical transport reaction by Lange et al.[78] that can use a relatively simple setup while avoiding toxic catalysts or "dirty" flux methods[79, 80].

## 1.3 Synthesis of 2D black phosphorus

### 1.3.1 Mechanical exfoliation

The mechanical exfoliation method, usually operated with a Scotch tape, has been successfully used to prepare single- and few-layer black phosphorus nanosheets[81]. After transferring onto Si/SiO<sub>2</sub> substrate, few layer BP is cleaned with acetone, isopropyl alcohol and methanol to remove any scotch tape residue. And finally, the exfoliated sample needs to be heated to 180°C to remove solvent residue[82].

Mechanical exfoliation is only suitable for small-scale production for fundamental research purpose and by its nature, not a scalable process. Moreover, it is reported that mechanically exfoliated 2D BP flakes are susceptible to ambient exposure, leading to an irreversible degradation to oxidize phosphorus compounds[83]. In order to harvest the material's predominant properties, optimized synthesis strategies are demanded to produce large quantities of exfoliated nanoflakes.

### 1.3.2 Organic-phase exfoliation

The most popular and common way of liquid exfoliation to produce mono- or few-layer black phosphorus from bulk black phosphorus adopts an organic phase as solvent. A few organic reagents have been chosen as good solvent for liquid exfoliation, including N-methyl-2-pyrrolidone (NMP)[84], dimethylformamide (DMF)[85], dimethyl sulfoxide (DMSO)[86], Isopropanol (IPA)[87], N-Cylohexyl-2-pyrrolidone (CHP)[88] etc. For example, Brent presented a simple and scalable route to exfoliate one-to five-layer phosphorene nanosheets with significant lateral dimensions in NMP[89].

### 1.3.3 Water-phase exfoliation

Although those organic solvents can efficiently exfoliate bulk black phosphorus into thin nanoflakes, their adsorption on the surface of as-exfoliated nanosheets is too intimate to be removed. The organic residue may be a great threat when concerning the feasibility of using phosphorene in future bio-analysis. Very recently, Wang successfully prepared ultrathin black phosphorus nanosheets by exfoliating bulk samples in water[90]. In brief, bulk black phosphorus was first dispersed in distilled water that bubbled with argon to eliminate the dissolved oxygen molecules for avoiding oxidation, and then swelled by H<sub>2</sub>O as intercalated molecule, stepped by sonication in ice water for 8 hour. Suspensions were centrifuged for 10 min at 1500 rpm to remove the residual unexfoliated particles, and the supernatant was collected for further use. The as-exfoliated product turns out to be a free-standing nanosheet with diameter of about several hundred nanometers. The thickness of those nanosheet measured by atomic force microscopy (AFM) presents a height of about 2.0 nm, which corresponds to four individual black phosphorus layers.

### 1.3.4 Other synthesis routes

Besides mechanical exfoliation and liquid exfoliation, several other methods are developed as well, such as plasma treatment[91]. With a subsequent Ar<sup>+</sup> plasma treatment after tape-exfoliation, not only the thickness of exfoliated black phosphorus films can be controlled by performing an optimized plasma etching process on the top surface of the black phosphorus film, but it also removes the chemical degradation of the exposed black phosphorus surface by passivation with PMMA after plasma treatment as well.

## 1.4 Structural properties of black phosphorus

Black phosphorus forms a layered structure (fig 1.2) with single element, phosphorus, just like graphene. However, it has several differences when compared with other layered materials consisting of group IV elements. A phosphorene monolayer, however, is puckered with the P atoms

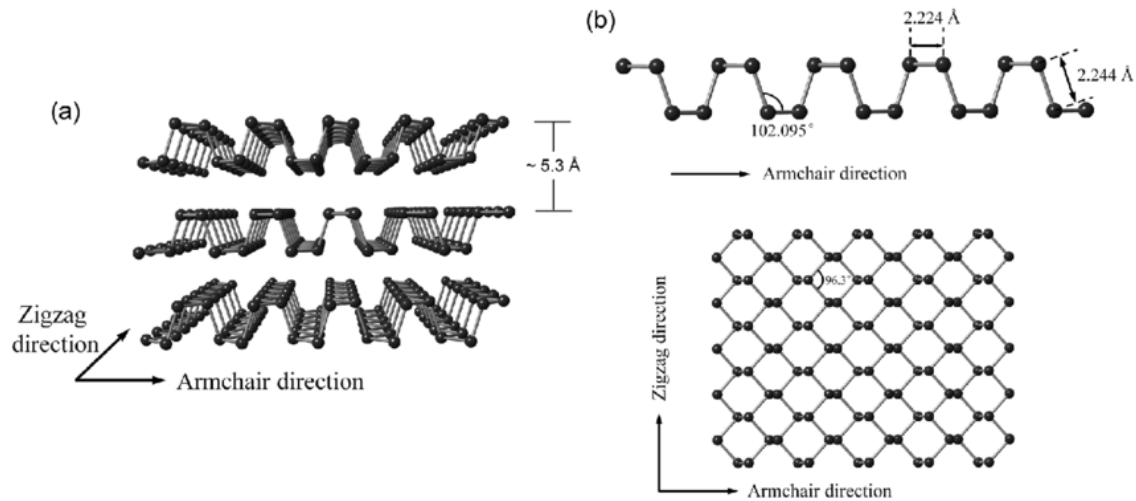


Figure 1.2: (a) Atomic structure of multi-layer black phosphorus and (b) monolayer phosphorene. Figure is taken from J. Mater. Chem. C, 2015,3, 8760-8775

being  $sp^3$  hybridized. Each of them is covalently bonded to three neighbors, and has one lone pair of electrons in the fourth hybrid orbital. Because of its puckered structure, a single layer of black phosphorus consists of two atomic sub-layers and includes two kinds of interatomic bonds.

### 1.4.1 Experimental crystal structural parameters

The experimental lattice constants of black phosphorus in its orthorhombic crystal structure are<sup>[77]</sup>  $\mathbf{a}=4.3763 \text{ \AA}$ ,  $\mathbf{b}=3.3134 \text{ \AA}$ ,  $\mathbf{c}=10.478 \text{ \AA}$ . The shorter bond with length  $2.224 \text{ \AA}$  connects phosphorus in the same layer and the longer bond with length  $2.244 \text{ \AA}$  connects phosphorus at top and bottom in single layer. Individual puckered layers are stacked together by weak van der Waals forces with separation of  $\sim 5.3 \text{ \AA}$ , thereby creating the bulk black phosphorus multilayer structure. The theoretical lattice constants of monolayer black phosphorus using different exchange-correlations will be mentioned in the subsequent chapters according to its relevance.

Black P has three crystalline structures<sup>[92]</sup>. Black phosphorus can be reversibly converted into a rhombohedral phase under high pressure of 5 GPa (layered structure type of gray As) and further at 10 GPa to a simple cubic structure ( $\alpha$ -Po structure type). No further structural changes were reported up to 60 GPa.

## 1.5 Electronic band structure and tunable band gap

The band structure of bulk black phosphorus (BP) was verified by angle-resolved photoemission spectroscopy (ARPES) measurements, as well as ab-initio calculations. The filled bands of freshly cleaved bulk crystal measured by ARPES are shown in Fig. 1.3, and largely agree with screened hybrid functional calculations with no material-dependent empirical parameter. Similar to transition metal dichalcogenides, the band gap of BP shows thickness dependence, increasing from  $\sim 0.3$  eV for the bulk to  $\sim 2$  eV for the monolayer[93]. The semiconducting transition metal dichalcogenides only have indirect bandgaps in multilayers, while the bandgap of black phosphorus is direct for all thicknesses. The increase of bandgap for single-layer phosphorene is predicted to be caused by the absence of interlayer hybridization near the top of the valence and bottom of the conduction band. In addition, compressive and tensile strain can lead to a significant modification of the black phosphorus band structure especially in its single- and few-layer forms. The appealing small but tunable bandgap of BP can therefore bridge the space between zero-gap graphene and large-gap TMDs (1 – 2 eV), making it an ideal material for near and mid-infrared optoelectronics. Moreover, due to the small bandgap resulted from the large excitation binding energy, both p-type and n-type configurations can be tuned in BP, while few-layer MoS<sub>2</sub> can just be tuned into n-type semiconductor. Single-layer to thin film BP can cover a very broad energy spectrum and interact strongly with electromagnetic waves in the mid-infrared, near-infrared, and visible frequency range where many important applications in defense, medicine, and communication lie, such as night vision, thermal imaging, and optical communication networks.

## 1.6 In plane anisotropy in black phosphorus

Anisotropic properties of black phosphorus are mainly due to its crystal structure. The anisotropy of black phosphorus is much stronger than other two-dimensional materials such as graphene or Mo- and W-based TMDCs. There are properties which show anisotropy and they can be divided into mechanical property, optical property and electronic property.

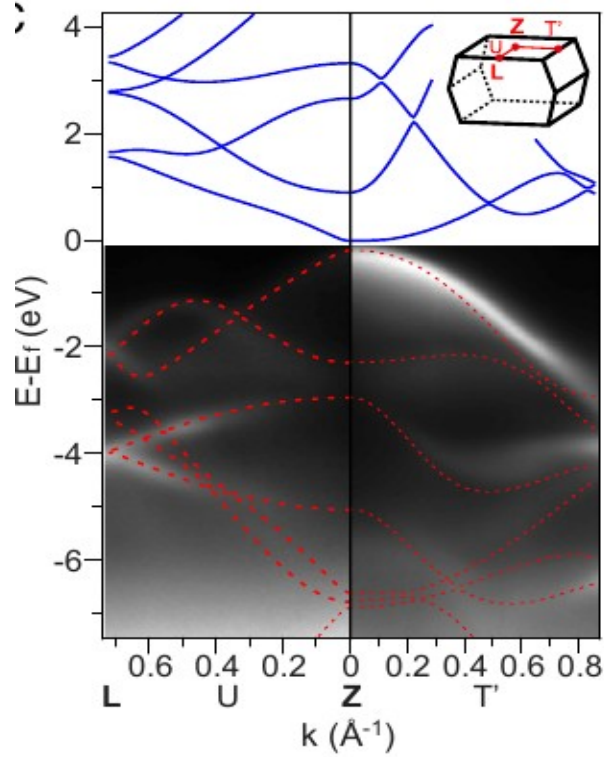


Figure 1.3: Band structure of bulk black P mapped out by ARPES measurements. A band gap around 0.3 eV is clearly observed. Superimposed on top are the calculated bands of the bulk crystal. Blue solid and red dashed lines denote empty and filled bands, respectively. The directions of the ARPES mapping are along U (LZ) and T, as indicated in the first Brillouin zone shown in Inset.  $E_f$  is the Fermi energy (Figure is taken from (Nat Nanotechnol 9(5):372377))

Jiang and Park<sup>[94]</sup> performed first-principles calculations and revealed that black phosphorus has different Young's modulus value for the armchair direction and the zigzag direction (the directions are shown in fig 1.1). In single layer black phosphorus, Young's modulus for the armchair direction has the value of 21.9 N/m, while the zigzag direction has more than twice larger value, 56.3 N/m.

In the same manner, thermal conductivity shows similar tendency with the study of Lee et al<sup>[95]</sup>. They compared the thermal conductivity along zigzag and armchair directions with suspended-pad micro-devices under the condition of steady-state longitudinal heat flow. The anisotropy is clearly distinguished when temperature is above 100 K. In addition, by solving the phonon Boltzmann transport equation based on first-principles calculations, Qin et al. <sup>[96]</sup> calculated the thermal conductivity of black phosphorus. At 300 K, the thermal conductivities of zigzag direction and

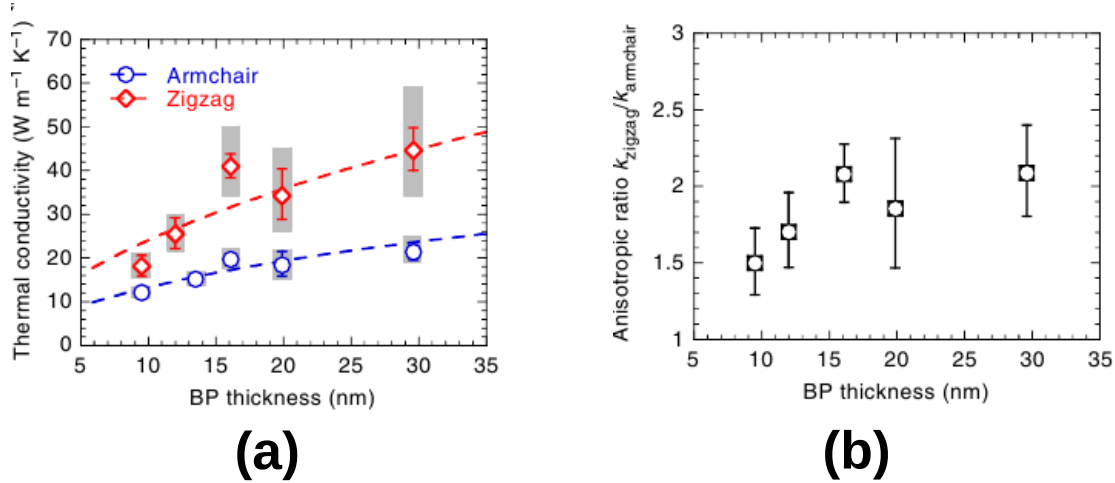


Figure 1.4: (a) Armchair and zigzag in-plane thermal conductivities ( $k_{armchair}$  and  $k_{zigzag}$ ) of multiple BP films. Dashed lines are results of theoretical modelling. The grey error bars account for the uncertainty of SiN substrate thermal conductivity  $k_{SiN}$ , whereas the blue/red error bars do no. (b) The anisotropic ratio  $k_{zigzag}/k_{armchair}$  at different BP thicknesses. The ratio at 12-nm thickness is calculated using linearly interpolated armchair thermal conductivity from adjacent thicknesses (Figure is taken from ref.(Nature Communications 6, 1 (2015))

armchair directions are 30.15 W/mK and 13.65 W/mK, respectively. Luo et al.[97] has measured the anisotropic thermal conductivity experimentally at different thickness of black phosphorus as shown in Fig1.4. Figure 1.5 plots the angular dependency of absorption coefficient and extinction spectra. The plot of absorption coefficient and extinction spectra both shows the dumbbell shape. Along the armchair direction (x-axis), black phosphorus represents high absorption and extinction. For zigzag direction, there is not any absorption or extinction relative to its perpendicular direction[98]. These optical property anisotropies are strongly induced by some extrinsic factors, such as structural deformation, corrugations or defects. Figure 1.6 shows the Hall mobility of the black phosphorus along the armchair (x-axis) and zigzag (y-axis) directions. For both thicknesses, 8 nm and 15 nm, mobilities along the armchair direction are approximately double compared with those along the zigzag direction. The anisotropic behavior of electric property was also measured in a multi-electrode transistor based on black phosphorus. The schematic in fig. 1.7 represents that a transistor consisting of Ti/Au contact and few-layer phosphorene was fabricated. Contacts are allocated in round shape with an angular interval, 45°. The maximum drain current at a 30 V back gate bias and a 0.5 V drain bias is displayed in fig. 1.7. The maximum drain current shows a

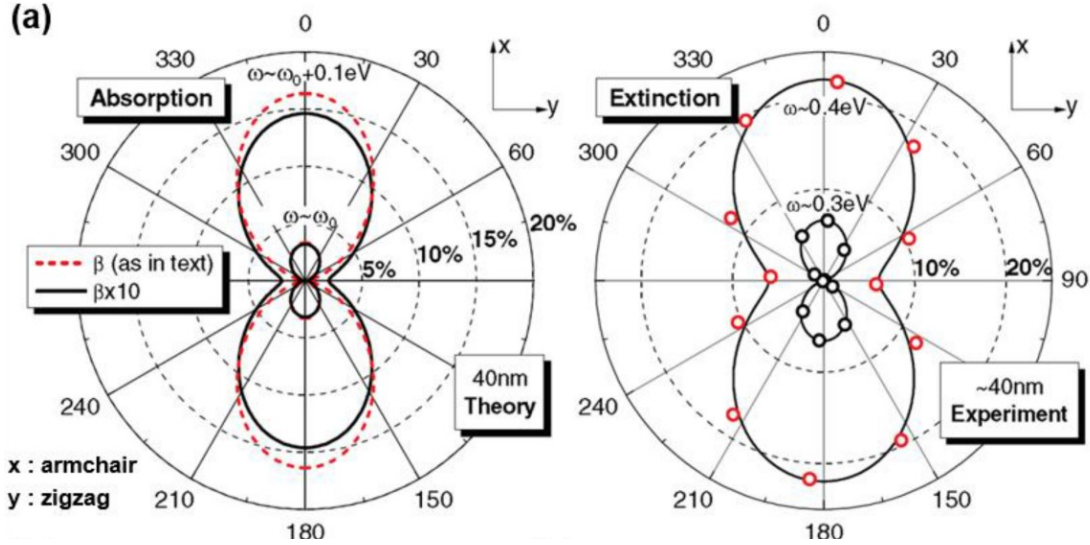


Figure 1.5: Polar representation of the absorption coefficient and experimental extinction spectra of the 40-nm intrinsic black phosphorus film. Absorption coefficient is represented with two different interband coupling strength  $\beta$  which gives different band gap value  $\omega$ . Extinction spectra are obtained from FTIR spectroscopy with black phosphorus on  $\text{SiO}_2$  substrate (Figure is taken from ref. (Phys. Rev. B 90, 075434))

sinusoidal-like curve with obvious angle dependent property. The maximum drain current has its minimum value of 85 mA/mm at  $45^\circ$  and  $225^\circ$  and maximum value of 137 mA/mm at  $135^\circ$  and  $315^\circ$  [99].

## 1.7 Device applications

Some potential applications of black phosphorus are gas sensor [100], water splitting photocatalyst [101], thermoelectrics [102], battery material [103] etc. Transistor is one of the most basic and important applications in electronics. For the outstanding performance of transistor, the channel material should possess high carrier mobility, high on/off ratio and high conductivity with low conductance when it is turned. Other two-dimensional materials such as graphene or TMDs are suggested as a candidate for the channel material. Graphene has a remarkable carrier mobility from  $3000 \text{ cm}^2/\text{V.s}$  to  $27,000 \text{ cm}^2/\text{V.s}$ . However, because of its metallic behavior with its zero band gap, it is impossible to achieve low off-state current. In the case of TMDs, they possess high on/off ratios but relatively low carrier mobilities, which interfere with enhancing transistor performance. On the

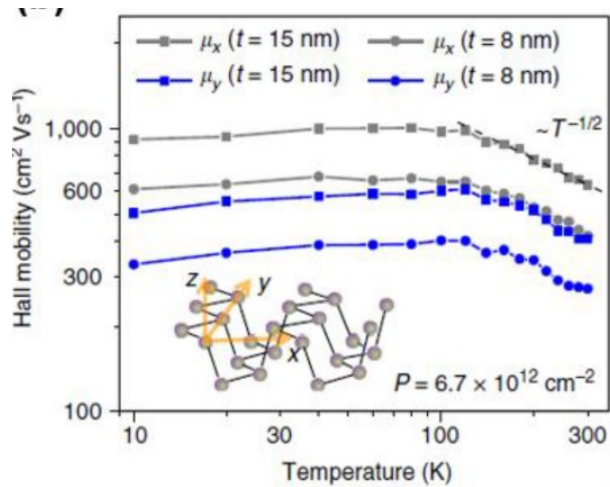


Figure 1.6: Hall mobility measured along x (armchair) and y (zigzag) direction on 8 nm and 15 nm black phosphorus film with constant hole doping concentration of  $6.7 \times 10^{12} \text{ cm}^{-2}$  (ACS Nano volume: 8, 4033 (2014)).

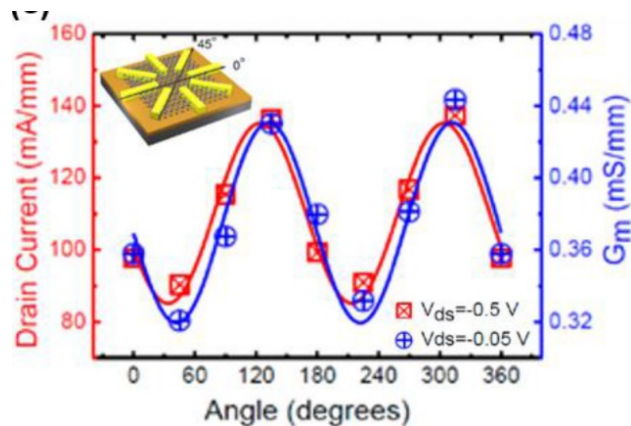


Figure 1.7: Schematic of the device structure for determining the angle-dependent transport behavior and angular dependence of the drain current and the transconductance of a device. Device is composed of electrodes and black phosphorus film with 10 nm thickness (ACS Nano volume: 8, 4033 (2014))

other hand, black phosphorus is able to satisfy required properties. Its mobility can reach up to  $\sim 1000 \text{ cm}^2/\text{V.s}$  when the direction is regulated and high on/off ratios, superior to that of TMDs, can be achieved.

In transistor application metal contact with semiconductor plays a vital role to determine the type of carrier to carry the current. Here we will mention few experimental observation of metal/black phosphorus contact in field effect transistor (FET) devices.

Du et al.[104] found Pd to form better contact with few layer phosphorene channels compared to Ni. With Ni electrodes, the FET behaved as an ambipolar one, but for Pd it showed p-type characteristics. Das et al.[105] found both p-type FET and n-type FET with Ti and Pd electrodes under different gate-bias conditions. Pd electrodes were found to be efficient hole injectors into phosphorene while Ti electrodes were more efficient electron injectors. Perello et al.[106] also found channel-thickness and metal-electrode-dependent behavior of phosphorene FETs. With Al electrodes, thinner channels showed n-type FET behavior while thicker ones showed ambipolar behavior. For Pd electrodes, phosphorene behaved as ambipolar FET, contrary to what was claimed by Du et al. In one of the first studies on phosphorene FETs, Li et al.[107] used Cr/Au and Ti/Au electrodes. Schottky barrier formation for electron injection was detected at the metal phosphorene interfaces(MPIs), and phosphorene behaved as ambipolar FET in these devices. The MPI was Ohmic for hole injection. Liu et al.[108] on the other hand, used Ti/Au electrodes and found phosphorene to behave as a p-type FET. A Schottky barrier formation for hole injection was also detected at the MPI.

## 1.8 Nanoribbons

While two-dimensional (2D) thin crystals limit the physical phenomena into a plane, in a one-dimensional (1D) quantum structure (nanowires, nanotubes, and nanoribbons (NRs)), charge carriers and excitations have only one degree of freedom. These crystal structures have been the focus of interest due to their unique properties such as very high electronic density of states, enhanced ex-

citon binding energy, diameter-dependent bandgap, increased surface scattering for electrons and phonons, and chirality-dependent electronic band structure. Nanoribbons (NRs), made of single- or few-atom-thick lamellar crystals, are novel forms of 1D nanoscale materials and are ideal systems for investigation of the size and dimensionality dependence of the fundamental properties. After successful synthesis of many 2D monolayer materials, their 1D NR form came into prominence due to their necessity in nanoscale applications.

Graphene nanoribbons (GNRs) is the first in the 1D NR which is fabricated in experimental methods: (i) cutting graphene along special directions by using lithography, (ii) bottom-up synthesis from precursor molecules, and (iii) unzipping of carbon nanotubes (CNTs). NRs of graphene can form zigzag and armchair shaped edges which directly determine their magnetic and electronic properties. 2D graphene has zero band gap, which can be opened up by fabricating nanoribbon. Fabricating GNRs with well-ordered edges and controllable widths is an important issue for their applications in nanoscale devices. Modification of electronic properties in GNRs can also be done by edge functionalization or applying external electric field.

Unlike graphene,  $\text{MoS}_2$  has finite band gap. Fabricating the 1D NR form, the gap is tunable by its width and therefore this structure can be expected to be a promising material for technological applications. Other examples of NRs are made from 2D materials which are  $\text{WS}_2$ ,  $\text{ReS}_2$ ,  $\text{ReSe}_2$ ,  $\text{TiSe}_2$ ,  $\text{GaS}$ ,  $\text{GaSe}$ ,  $\text{ZnSe}$ ,  $\text{SnSe}$ ,  $\text{TiS}_3$ ,  $\text{ZrS}_3$ , silicene, germanene, h-BN.

Recently exfoliated 2D material, black phosphorus(BP) motivates researchers to study the properties of nanoribbons made from BP. Das et al.[109] demonstrated the formation of few-nanometer-wide black phosphorus NRs (BPNRs) with both zigzag and armchair edges with controlled structural modification of few layer black phosphorus. Using a top-down method, it is possible to fabricate NR from suspended few-layer black phosphorus flakes. The fabricated BPNRs were about 10 nm on width and few layers on thickness. We will discuss electronic structure of different edge-types of phosphorene (monolayer black phosphorus) NR using density functional theory calculations and some its properties in chapter 5.

## 1.9 Blue phosphorus

The exciting properties of black phosphorus led researchers to discover new 2D allotropes of phosphorus. A new allotrope of phosphorus called blue phosphorus was predicted by Zhu et al.[110]. Recently, it has become possible to synthesize monolayer blue phosphorus on Au(111) substrate by molecular beam epitaxy (MBE) technique[111]. A free standing monolayer blue phosphorus was found to be metastable but it retains its stability on Au substrate[112].

The wide band gap of 2 eV of monolayer blue phosphorus (blue phosphorene) makes it useful in field effect transistor (FET) devices. Though, blue phosphorene has small carrier mobility (electron mobility is  $20 \text{ cm}^2/\text{V.s}$ )[112], it can be tuned by applying strain[113]. Like mobility, carrier concentration is also an important ingredient in controlling the conductivity. The carrier concentration of blue phosphorene can be tuned by applying external electric field or impurity inclusion, as a result the conductivity can also be tuned. The quality of contact between blue phosphorene and metal surfaces is an important parameter in controlling the FET device efficiency. Metal electrodes form an electrostatic barrier at the contact of blue phosphorene. The charge carrier injection in the semiconductor from metal can be controlled by the intrinsic electronic properties of metal and semiconductor viz. work function of metal and electron affinity and ionization potential of semiconductor. The contact barrier has been studied by making heterostructures of blue phosphorene with TMD (transition metal dichalcogenides)[114], graphene, graphene like GaN.

## 1.10 Structure of the thesis

Motivated by the interesting properties of phosphorene, my thesis is devoted to few aspects of phosphorene. Growing attention of phosphorene encourages us to study its characteristics. The plan of my thesis is as follows.

**Chapter 2** is devoted to the methods and techniques used to perform the simulations in this thesis. The basic theoretical framework is DFT, which allows to solve the many-particle problem through independent electron approximation. Next we have discussed the techniques for solving

the Kohn-Sham equations using plane-wave basis sets, and construction of PAW potentials. In this end, we have shown the derivation of the charge carrier mobility expression in two dimensional structures.

**Chapter 3** includes the variation of mobility with strain. The property of a semiconductor that ultimately governs its transport behavior is carrier mobility. Although effective mass is an important factor determining mobility, it is not the only one. Even within the simple model of phonon scattering, mobility depends on the so-called deformation potential (DP). Therefore, a proper analysis of variation of mobility with strain requires more than just the calculation of effective mass. We will discuss variation of mobility using HSE06 method with uniaxial strain along armchair and zigzag direction.

**Chapter 4** is devoted to the study of metal/phosphorene interface. We have calculated Schottky barrier height and tunnel barrier height at the metal/phosphorene interface. We have chosen low index surfaces Pd(111), Pd(100), Pd(110), Au(110), Ni(110) and Ti(0001).

**Chapter 5** is concerned about the electronic properties of three types of phosphorene nanoribbon (PNRs) having three types of edges: armchair, linear and zigzag.

**Chapter 6** gives the results of metal/blue phosphorene interfaces and Schottky barrier height and tunnel barrier height. In this study we have chosen Pd(111), Pd(110), Pd(100), Au(110), Ni(100) and Al(111).

# Chapter 2

## Methods

The starting point of a quantitative theoretical investigation of the properties of solids is the many-body Schrodinger equation. The many-body Hamilton operator of the solid is given by

$$\hat{H} = - \sum_{I=1}^P \frac{1}{2M_I} \nabla_I^2 - \sum_{i=1}^N \frac{1}{2} \nabla_i^2 + \frac{1}{2} \sum_{I=1}^P \sum_{J \neq I}^P \frac{Z_I Z_J}{|\mathbf{R}_I - \mathbf{R}_J|} + \frac{1}{2} \sum_{i=1}^N \sum_{j \neq i}^N \frac{1}{|\mathbf{r}_i - \mathbf{r}_j|} - \sum_{I=1}^P \sum_{i=1}^N \frac{Z_I}{|\mathbf{R}_I - \mathbf{r}_i|} \quad (2.A)$$

Here  $\mathbf{R} = \{\mathbf{R}_I, I = 1, \dots, P\}$  is a set of  $P$  nuclear coordinates, and  $\mathbf{r} = \{\mathbf{r}_i, i = 1, \dots, N\}$  is a set of  $N$  electronic coordinates.  $Z_I$  and  $M_I$  are the nuclear charges and masses, respectively. The first and second terms represent the kinetic energy contributions ( $T_n$  and  $T_e$ ) of the nuclei and electrons, the third and fourth terms represent the electron-electron and nucleus-nucleus repulsive interactions ( $V_{nn}$  and  $V_{ee}$ ) respectively. The last term represents the attractive potential ( $V_{ne}$ ) between the nuclei and electrons. In principle, the total energy of the system can be obtained by solving the Schrödinger equation.

$$\hat{H}\xi(\mathbf{R}, \mathbf{r}, t) = E_{tot}\xi(\mathbf{R}, \mathbf{r}, t) \quad (2.B)$$

where  $E_{tot}$  is the total energy and  $\xi(\mathbf{R}, \mathbf{r}, t)$  are the many-body wavefunction of electron-nuclei system. The many-body wave function depends on the coordinates of all the atoms  $\mathbf{R}_I$ , and on the space and spin coordinates of all electrons  $\mathbf{r}_i$ .

## 2.1 Born-Oppenheimer approximation

Considering that nuclei are much heavier than electrons, one can assume that electrons react to an external field much faster than nuclei. Thus, it seems to be reasonable to assume that electrons adjust without noticeable delay to the current positions of the atoms  $R_I$ . Formulated more precisely, it can be said that electrons in general react to a perturbation on a time scale of femtoseconds ( $10^{-15}$  s), while nuclei require times of the order of picoseconds ( $10^{-12}$  s). Thus, we may assume that from the electrons point of view the nuclei do not move (or move sufficiently slowly). If the kinetic energy of the nuclei would be zero (or  $M_I/m \rightarrow \infty$ ), the electrons could be described by the equation

$$\hat{H}_e = \hat{T}_e + \hat{V}_{ne} + \hat{V}_{ee} \quad (2.1)$$

We assume that at each time, i.e., for each lattice geometry  $\mathbf{R}_I$ , the electrons are in an eigenstate of  $\hat{H}_e$ . The electrons do not feel the nuclear motion and are always in the electronic ground state. This is called the **Born-Oppenheimer approximation**.

Many traditional approaches to solving this difficult many-body problem [2.1](#) begin with the HartreeFock (HF) approximation, in which electronic wave function is approximated by a single Slater determinant (an antisymmetrized product) of orbitals (single-particle wavefunctions) and the energy is minimized. These include configuration interaction, coupled cluster, and Moller-Plesset perturbation theory, and are mostly used for finite systems, such as molecules in the gas phase. Other approaches use reduced descriptions, such as the density matrix or Greens function, but leading to an infinite set of coupled equations that must somehow be truncated, and these are more common in applications to solids. More accurate methods usually require more sophisticated calculations, which takes longer on a computer. Thus, there is a compelling need to solve ground-state electronic structure problems reasonably accurately, but with a cost in computer time that does not become prohibitive as the number of atoms (and therefore electrons) becomes large.

## 2.2 Density functional theory

The density functional theory (DFT) treats the electron density as the central variable rather than the many-body wavefunction. This conceptual difference leads to a remarkable reduction in difficulty: the density is a function of three variables, i.e. the three Cartesian directions, rather than  $3N$  variables as the full many-body wavefunction is.

## 2.3 Hohenberg-Kohn Theorems

In 1964 Hohenberg and Kohn [115] developed an exact formal variational principle to determine the ground energy of many-body system, where electron density is chosen to be the basic variable. They gave two theorems that laid the foundation of the DFT.

**Theorem I:** The external potential  $v(\mathbf{r})$  is uniquely determined by the ground-state electron density  $\rho(\mathbf{r})$ , within a trivial additive constant. Thus the ground state density determines the full Hamiltonian, except for a constant shift of the energy.

Hence all the properties of the many-body electronic system such as total energy and kinetic energy are also functionals of the ground state electron density  $\rho(\mathbf{r})$ .

**Theorem II:** For a trial density  $\tilde{\rho}(\mathbf{r})$ , such that  $\tilde{\rho}(\mathbf{r}) \geq 0$  and  $\int \tilde{\rho}(\mathbf{r}) d\mathbf{r} = N$ , the total energy functional  $E[\tilde{\rho}]$  has a lower bound equal to the ground state energy  $E[\rho(\mathbf{r})]$  of the system:

$$E[\rho(\mathbf{r})] \leq E[\tilde{\rho}(\mathbf{r})] \quad (2.1)$$

where  $\rho(\mathbf{r})$  is the ground state electron density of the system.

Using the first theorem, the total energy functionals for a electronic system at a certain external potential  $v(\mathbf{r})$  can be written as,

$$E_v[\rho] = T_e[\rho] + V_{ne}[\rho] + V_{ee}[\rho] = F_{HK}[\rho] + \int \rho(\mathbf{r})v(\mathbf{r})d\mathbf{r} \quad (2.2)$$

$$F_{HK}[\rho] = T_e[\rho] + V_{ee}[\rho] \quad (2.3)$$

Where  $F_{HK}$  is a universal functional of  $\rho(\mathbf{r})$  because it is independent of the external potential. It includes kinetic energy of the electrons  $T_e[\rho]$  and the interaction energy between the electrons  $V_{ee}[\rho]$ .

The second KS theorem provides a variational principle for  $E_v[\rho(\mathbf{r})]$  with  $\rho(\mathbf{r})$  as the basic variable. The minimization of the total energy functional  $E_v[\tilde{\rho}(\mathbf{r})]$  with respect to a trial density  $\tilde{\rho}(\mathbf{r})$  gives the ground state density  $\rho(\mathbf{r})$  which in turn determine ground state energy  $E[\rho(\mathbf{r})]$  of the system. Hence ground state density  $\rho(\mathbf{r})$  which minimizes  $E[\rho(\mathbf{r})]$  can be obtained via stationary principle

$$\delta\{E_v[\rho] - \mu[\int \rho(\mathbf{r})d\mathbf{r} - N]\} = 0, \quad (2.4)$$

where  $\mu$  is the Lagrange multiplier for the constraint  $\int \rho(\mathbf{r})d\mathbf{r} = N$ . Equation (2.4) gives the Euler-Lagrange equation,

$$\mu = \frac{\delta E_v[\rho]}{\delta \rho(\mathbf{r})} = v(\mathbf{r}) + \frac{\delta F_{HK}[\rho]}{\delta \rho(\mathbf{r})} \quad (2.5)$$

where  $\mu$  is the chemical potential of the  $N$ -electron system.

### 2.3.1 The Kohn-Sham (KS) Equations

In principle, if we knew the exact functional  $F_{HK}$ , equation (2.2) would be an exact equation for the ground-state properties. Unfortunately, the exact  $F_{HK}$  is unknown, leaving the Hohenberg-Kohn theorems without much practical relevance. In 1965 Kohn and Sham [116] gave an ansatz which state that the ground state density of an interacting system can be represented by the ground state density of a reference system of non-interacting electrons. This maps the problem of the system of interacting electrons onto a reference system of non-interacting electrons and introduces a set of single particle equations known as Kohn-Sham equations.

Within this approach, the ground state density of the interacting system  $\rho(\mathbf{r})$ , can be written as

$$\rho(\mathbf{r}) = \sum_i^N |\psi_i(\mathbf{r})|^2 \quad (2.6)$$

where  $\psi_i(\mathbf{r})$  are the spin orbitals known as Kohn-Sham orbitals. The Hamiltonian for non-interacting reference system with the same ground state density  $\rho(\mathbf{r})$  can be written as

$$\hat{H}_R = \sum_i^N \left[ -\frac{1}{2} \nabla_i^2 + v_{eff}(\mathbf{r}_i) \right] \quad (2.7)$$

Here the effective potential  $v_{eff}(\mathbf{r})$  is such that the ground state density of  $\hat{H}_R$  is the same as  $\rho(\mathbf{r})$ . Since  $\hat{H}_R$  is non-interacting, the ground state wave function can be represented by a Slater determinant of the  $N$  lowest-energy eigenfunctions.

The kinetic energy  $T_s[\rho]$  of the reference system can be written as

$$T_s[\rho] = -\frac{1}{2} \sum_i^N \langle \psi_i | \nabla^2 | \psi_i \rangle \quad (2.8)$$

The one-electron orbitals  $\psi_i(\mathbf{r})$  can be obtained by solving the one-electron Schrödinger equation

$$\left[ -\frac{1}{2} \nabla^2 + v_{eff}(\mathbf{r}) \right] \psi_i(\mathbf{r}) = \hat{H}_{KS} \psi_i(\mathbf{r}) = \varepsilon_i \psi_i(\mathbf{r}) \quad (2.9)$$

where  $\hat{H}_{KS}$  are the one-electron Hamiltonian and  $\varepsilon_i$  are the Kohn-Sham orbital energies. Hence an interacting system is transformed to a noninteracting system, where electrons move in an effective potential  $v_{eff}(\mathbf{r})$ . Using equation(2.8) and equation(2.3), the universal functional  $F_{HK}$  can be written as

$$F_{HK}[\rho] = T_s[\rho] + J[\rho] + E_{xc}[\rho] \quad (2.10)$$

where  $J[\rho]$  is classical Coulomb energy term, defined as,

$$J[\rho] = \frac{1}{2} \iint \frac{\rho(\mathbf{r})\rho(\mathbf{r}')}{|\mathbf{r}-\mathbf{r}'|} d\mathbf{r}d\mathbf{r}' \quad (2.11)$$

$E_{xc}[\rho]$  is exchange-correlation energy, defined as,

$$E_{xc}[\rho] = (T_e[\rho] - T_s[\rho]) + (E_{ee}[\rho] - J[\rho]) \quad (2.12)$$

$T_e$  and  $T_s$  are the kinetic energy of interacting and non-interacting electrons respectively. The exchange-correlation energy contains the kinetic correlations which are ignored in  $T_s[\rho]$  and the non-classical contributions of the interacting electrons. By substituting  $F_{HK}[\rho]$  in the total energy functional Eq (2.2), the Kohn-Sham energy functional is obtained as

$$E_{KS}[\rho] = \int \rho(\mathbf{r})v(\mathbf{r})d\mathbf{r} + T_s[\rho] + J[\rho] + E_{xc}[\rho] \quad (2.13)$$

Now minimizing the Kohn-Sham energy functional  $E_{KS}[\rho]$  with respect to density  $\rho(\mathbf{r})$ , under the constraint  $\int \rho(\mathbf{r})d\mathbf{r} = N$ , we get the Euler equation as

$$\mu = v(\mathbf{r}) + \frac{\delta T_s[\rho]}{\delta \rho(\mathbf{r})} + \frac{\delta J[\rho]}{\delta \rho(\mathbf{r})} + \frac{\delta E_{xc}[\rho]}{\delta \rho(\mathbf{r})} \quad (2.14)$$

Here  $\mu$  is the chemical potential of the non-interacting system, which should coincide with the the chemical potential of the interacting system. Hence comparing equations (2.14) and (2.5), we can obtain the KS effective potential.

$$v_{eff}(\mathbf{r}) = v(\mathbf{r}) + \frac{\delta J[\rho]}{\delta \rho(\mathbf{r})} + \frac{\delta E_{xc}[\rho]}{\delta \rho(\mathbf{r})} = v(\mathbf{r}) + \int \frac{\rho(\mathbf{r}')}{|\mathbf{r} - \mathbf{r}'|} d\mathbf{r}' + v_{xc}(\mathbf{r}) \quad (2.15)$$

where the exchange-correlation potential  $v_{xc}(\mathbf{r})$  is defined as

$$v_{xc}(\mathbf{r}) = \frac{\delta E_{xc}[\rho]}{\delta \rho(\mathbf{r})} \quad (2.16)$$

In the Kohn-sham formalism electrons move in an effective potential  $v_{eff}(\mathbf{r})$ , which depends on the classical Coulomb potential, exchange-correlation potential and the external potential  $V(\mathbf{r})$ .

Hence the total energy of the system can be written as

$$E[\rho] = \sum_i^N \varepsilon_i - \frac{1}{2} \int \frac{\rho(\mathbf{r})\rho(\mathbf{r}')}{|\mathbf{r} - \mathbf{r}'|} d\mathbf{r}d\mathbf{r}' + E_{xc}[\rho] - \int \rho(\mathbf{r})v_{xc}(\mathbf{r})d\mathbf{r} \quad (2.17)$$

where  $\varepsilon_i = \langle \psi_i | -\frac{\nabla^2}{2} + v_{eff}(\mathbf{r}) | \psi_i \rangle$ . Since  $v_{eff}(\mathbf{r})$  depends on the density  $\rho(\mathbf{r})$  through the

Coulomb potential, which in turn depends on the  $\psi_i(\mathbf{r})$ 's, hence the solution of equation (2.9) can only be achieved by self-consistency. To solve these equations, for a given nuclei configuration, we start with some trial charge density and generate  $v_{eff}$ . Then the Kohn-Sham equations are solved to get  $\psi_i$ 's and the new  $\rho(\mathbf{r})$  is calculated. The same process is repeated iteratively till the old and new charge densities are same or the difference in energies obtained in two consecutive cycles is below some tolerance value. If the exact form of  $E_{xc}[\rho]$  were known, the Kohn-Sham formalism would lead to the exact energy, i.e. the correct eigenvalue of the Hamilton operator  $\hat{H}$  of the Schrödinger equation. The Kohn-Sham approach is thus in principle exact. The approximation only enters when we have an explicit form for the unknown functional for the exchange-correlation energy  $E_{xc}$  and its corresponding potential  $v_{xc}$ . A major goal of modern density-functional theory is therefore to find better and better approximations to the exchange-correlation energy.

## 2.4 The Exchange-correlation functional

The simplest approximation to  $E_{xc}$  was introduced by Kohn and Sham and is known as the local density approximation (LDA). The idea is to construct the exchange-correlation energy for an inhomogeneous gas from the electron density of the homogeneous gas  $\rho(\mathbf{r})$ . This can be done by assuming electron density as locally homogeneous at each point in space. In this way the LDA exchange-correlation energy will have the form,

$$E_{xc}^{LDA}[\rho] = \int \rho(\mathbf{r}) \varepsilon_{xc}(\rho(\mathbf{r})) d\mathbf{r} \quad (2.18)$$

where  $\varepsilon_{xc}(\rho(\mathbf{r}))$  is the exchange and correlation energy per particle of a homogeneous electron gas of density  $\rho(\mathbf{r})$ . The corresponding exchange-correlation potential becomes,

$$v_{xc}^{LDA}(\rho(\mathbf{r})) = \frac{\delta E_{xc}^{LDA}[\rho]}{\delta \rho(\mathbf{r})} = \varepsilon_{xc}[\rho(\mathbf{r})] + \rho(\mathbf{r}) \frac{\partial \varepsilon_{xc}^{LDA}[\rho]}{\partial \rho} \quad (2.19)$$

Further,  $\epsilon_{xc}(\rho(\mathbf{r}))$  can be divided into exchange and correlation contributions

$$\epsilon_{xc}(\rho) = \epsilon_x(\rho) + \epsilon_c(\rho) \quad (2.20)$$

The exchange part is given by Dirac as

$$\epsilon_x(\rho) = -C_x \rho(\mathbf{r})^{1/3}, \quad C_x = \frac{3}{4} \left( \frac{3}{\pi} \right)^{1/3} \quad (2.21)$$

The correlation part  $\epsilon_c(\rho)$  cannot be expressed by such an explicit functional form. Only numerical values are known from the highly accurate quantum Monte Carlo calculation of Ceperly and Alder[117]. This has been fitted to parameterize suitable expressions [118], which are used in most of the current electronic structure calculations.

The extension of LDA for spin-polarized systems with charge densities  $\rho_\uparrow(\mathbf{r})$  and  $\rho_\downarrow(\mathbf{r})$  (for up and down electrons respectively) can be written as.

$$E_{xc}^{LSDA} = -\frac{3}{2} \left( \frac{3}{4\pi} \right)^{1/3} \int \left[ \rho_\uparrow(\mathbf{r})^{4/3} + \rho_\downarrow(\mathbf{r})^{4/3} \right] d\mathbf{r} + \int \rho(\mathbf{r}) \epsilon_c(\rho_\uparrow(\mathbf{r}), \rho_\downarrow(\mathbf{r})) d\mathbf{r} \quad (2.22)$$

This is called local spin density approximation (LSDA). Here  $\epsilon_c(\rho_\uparrow(\mathbf{r}), \rho_\downarrow(\mathbf{r}))$  is the correlation energy per electron in a homogeneous electron gas.

From the above discussion, it seems that LDA should be a good approximation if the electron density  $\rho(\mathbf{r})$  is slowly varying. However, it gives good results even in cases where the density is not slowly varying. This theory does extremely well for metals. It underestimates the band gaps in semiconductors by a factor of  $1/2 - 1/3$ . Also it does not properly describe strongly correlated systems, particularly Mott insulators. Intense efforts have been devoted to improve upon LDA. A straightforward correction to the LDA is to construct an exchange-correlation functional, based on electron density as well as its gradient. This approximation is known as the generalized gradient

approximation (GGA).

$$E_{xc}^{GGA}[\rho_{\uparrow}, \rho_{\downarrow}] = \int f(\rho_{\uparrow}(\mathbf{r}), \rho_{\downarrow}(\mathbf{r}), \nabla\rho_{\uparrow}(\mathbf{r}), \nabla\rho_{\downarrow}(\mathbf{r})) d\mathbf{r} \quad (2.23)$$

with the function  $f$  being chosen by some set of criteria. There are a large number of distinct GGA functionals depending on the form of the function  $f$ . Two of the most widely used functionals in the literature are the Perdew-Wang functional (PW91)[119] and the Perdew-Burke-Ernzerhof functional (PBE)[120].

## 2.5 HSE06 functional

HSE06 functional was proposed by J. Heyd, G.E. Scuseria and M. Ernzerhof[121]. In HSE06 functional the short range part of exchange is a mix of Hartree-Fock (HF) nonlocal and PBE semilocal functionals. The long range parts of exchange and correlation are taken exactly as in PBE. The full exchange-correlation functional in HSE06 is written as

$$E_{xc}^{HSE} = eE_x^{HF,SR}(\omega) + (1 - e)E_x^{PBE,SR}(\omega) + E_x^{PBE,LR}(\omega) + E_c^{PBE} \quad (2.2)$$

where  $E_x^{HF,SR}$ ,  $E_x^{PBE,SR}$  and  $E_x^{PBE,LR}$  are the short- and long- range parts of the HF and PBE exchange energies, respectively.  $E_c^{PBE}$  is the PBE correlation energy.  $\omega$  gives the inverse length that separates the short- and long - range Coulomb interactions.  $e$  determines the fraction of short-range HF exchange. We used  $e=0.25$  and  $\omega=0.2\text{\AA}^{-1}$ , the default values in HSE06.

## 2.6 The Plane wave expansion

The most common approach to solve the Kohn Sham (KS) equations is to expand the single-particle eigenstates in terms of a set of basis functions. The KS equations then transform into equations for the expansion coefficient which may be solved by various well-established numerical methods.

Plane waves are orthonormal. Hence, upon a basis set expansion the KS equations transform into a simple matrix eigenvalue problem for the expansion coefficients. A further advantage of plane waves is that they are not biased to any particular atom. Any region in space is treated on an equal footing so that calculations do not have to be corrected for a basis set superposition error. Since plane waves do not depend on the positions of the atoms, the Hellman-Feynman theorem can be applied directly to calculate atomic forces. Even for a non-complete basis set the Pulay terms are identically zero.

A plane wave expansion of the Kohn-Sham orbitals can be achieved as follows :

$$\psi_i(\mathbf{r}) = \frac{1}{\sqrt{\Omega}} \sum_{\mathbf{q}} c_{i,\mathbf{q}} e^{i\mathbf{q}\cdot\mathbf{r}} = \sum_{\mathbf{q}} c_{i,\mathbf{q}} |\mathbf{q}\rangle \quad (2.24)$$

where  $\Omega$  is the volume of the crystal composed of  $N_{cell}$  primitive cells each of volume  $\Omega_{cell}$ . The  $c_{i,\mathbf{q}}$  are the expansion coefficients of the wave function in the basis of orthonormal plane wave  $|\mathbf{q}\rangle$  satisfying,  $\langle \mathbf{q}' | \mathbf{q} \rangle = \delta_{\mathbf{q},\mathbf{q}'}$ . Now inserting this in equation (2.7), taking the product with  $\langle \mathbf{q}' |$  and integrating in the real space gives

$$\sum_{\mathbf{q}} \langle \mathbf{q}' | \hat{H}_{eff} | \mathbf{q} \rangle c_{i,\mathbf{q}} = \epsilon_i \sum_{\mathbf{q}} \langle \mathbf{q}' | \mathbf{q} \rangle c_{i,\mathbf{q}} = \epsilon_i c_{i,\mathbf{q}'} \quad (2.25)$$

The matrix element of the kinetic energy operator can be written as

$$\langle \mathbf{q}' | -\frac{1}{2} \nabla^2 | \mathbf{q} \rangle = \frac{1}{2} |\mathbf{q}|^2 \delta_{\mathbf{q},\mathbf{q}'} \quad (2.26)$$

The effective potential,  $V_{eff}$  has the periodicity of the lattice and therefore the only allowed Fourier components are those with the reciprocal lattice vectors of the lattice. We thus have

$$V_{eff}(\mathbf{r}) = \sum_m V_{eff}(\mathbf{G}_m) \exp(i\mathbf{G}_m \cdot \mathbf{r}), \quad (2.27)$$

where  $\mathbf{G}_m$ 's are the reciprocal lattice vectors and  $V_{eff}(\mathbf{G}_m)$ 's are the Fourier components of  $V_{eff}(\mathbf{r})$ .

$$V_{eff}(\mathbf{G}) = \frac{1}{\Omega_{cell}} \int_{\Omega_{cell}} V_{eff}(\mathbf{r}) \exp(-i\mathbf{G}\cdot\mathbf{r}) d\mathbf{r}. \quad (2.28)$$

Thus the matrix element of the potential can be written as

$$\langle \mathbf{q}' | V_{eff} | \mathbf{q} \rangle = \sum_m V_{eff}(\mathbf{G}_m) \delta_{\mathbf{q}'-\mathbf{q}, \mathbf{G}_m}. \quad (2.29)$$

Thus, the matrix elements of the  $V_{eff}$  are nonzero only if  $\mathbf{q}$  and  $\mathbf{q}'$  differ by a reciprocal lattice vector  $\mathbf{G}_m$ . Assume  $\mathbf{q} = \mathbf{k} + \mathbf{G}_m$  and  $\mathbf{q}' = \mathbf{k} + \mathbf{G}_{m'}$ . Then for any given  $\mathbf{k}$ , the Schrödinger-like equation is given by

$$\sum_{m'} \left[ |\mathbf{k} + \mathbf{G}_m|^2 \delta_{m,m'} + V_{eff}(\mathbf{G}_m - \mathbf{G}_{m'}) \right] c_{i,m'}(\mathbf{k}) = \varepsilon_i(\mathbf{k}) c_{i,m}(\mathbf{k}) \quad (2.30)$$

where  $\delta_{m,m'}$  reflects that the kinetic energy is diagonal,  $\varepsilon_i$  are the electronic energies. The above equation is the basic Schrödinger-like equation of a periodic crystal with a plane wave basis set. Eigenfunctions of equation (2.30), for a given  $\mathbf{k}$  are given by equation (2.24), with the sum over  $\mathbf{q}$  restricted to  $\mathbf{q} = \mathbf{k} + \mathbf{G}_m$ . Hence

$$\begin{aligned} \psi_{i,\mathbf{k}}(\mathbf{r}) &= \frac{1}{\sqrt{\Omega}} \sum_m c_{i,m} \exp(i(\mathbf{k} + \mathbf{G}_m)\cdot\mathbf{r}) \\ &= \exp(i\mathbf{k}\cdot\mathbf{r}) \frac{1}{\sqrt{N_{cell}}} u_{i,\mathbf{k}}(\mathbf{r}) \end{aligned} \quad (2.31)$$

where

$$u_{i,\mathbf{k}}(\mathbf{r}) = \frac{1}{\sqrt{\Omega_{cell}}} \sum_m c_{i,m} \exp(i\mathbf{G}_m\cdot\mathbf{r}); \quad \Omega = N_{cell} \Omega_{cell} \quad (2.3)$$

This is the Bloch's theorem, where  $u_{i,\mathbf{k}}(\mathbf{r})$  carries the periodicity of the crystal. Here for each  $\mathbf{k}$ , the number of allowed reciprocal vectors  $\mathbf{G}$  is infinite. Hence, in principle infinite number of plane waves are required to represent the wave functions with infinite accuracy. However, the coefficients  $c_{i,m'}(\mathbf{k})$  for the plane waves with small kinetic energy are typically more important than those with

large kinetic energy. Thus the plane wave basis set can be truncated to include only plane waves that have kinetic energies less than a particular energy cutoff  $E_{cut}$ ,

$$\frac{1}{2}|\vec{k} + \vec{G}|^2 \leq E_{cut} \quad (2.32)$$

Employing a finite basis set may introduce some inaccuracy, therefore, appropriate convergence tests have to be performed in order to find an  $E_{cut}$  that is sufficient to compute the property of interest with the required accuracy.

## 2.7 The pseudopotential theory

Most physical and chemical properties of crystals depend to a very good approximation only on the distribution of the valence electrons. The core electrons do not participate in the chemical bonds and they are strongly localized around the nucleus. On the other hand, the deeply bound core electrons require a huge number of plane wave basis functions for their description which increase the computational cost. The pseudopotential approximation allows the electronic wave functions to be expanded using a much smaller number of plane waves, by replacing the strong ionic potential with a weaker and screened pseudopotential. In this approach only the chemically active valence electrons are considered explicitly, while the inert core electrons are eliminated using the "frozen-core approximation". All the electrostatic and quantum-mechanical interactions of the valence electrons with the cores, such as the nuclear Coulomb attraction screened by the core electrons, Pauli repulsion, and exchange and correlation between core and valence electrons, are accounted for an angular momentum-dependent pseudopotential. The concept of pseudopotentials is illustrated in fig 2.1, where true valence wave function  $\Psi$  is peaked far away from the nucleus (dotted curve). It has a lot of oscillations near the nucleus which ensures its orthogonality to the core states. The description of these nodes by plane wave demands high energy cutoffs. Since the all-electron valence wave function  $\Psi$  within the core region does not contribute significantly to the bonding properties, it can be approximated by a smooth and nodeless wave function  $\Psi_{ps}$  within

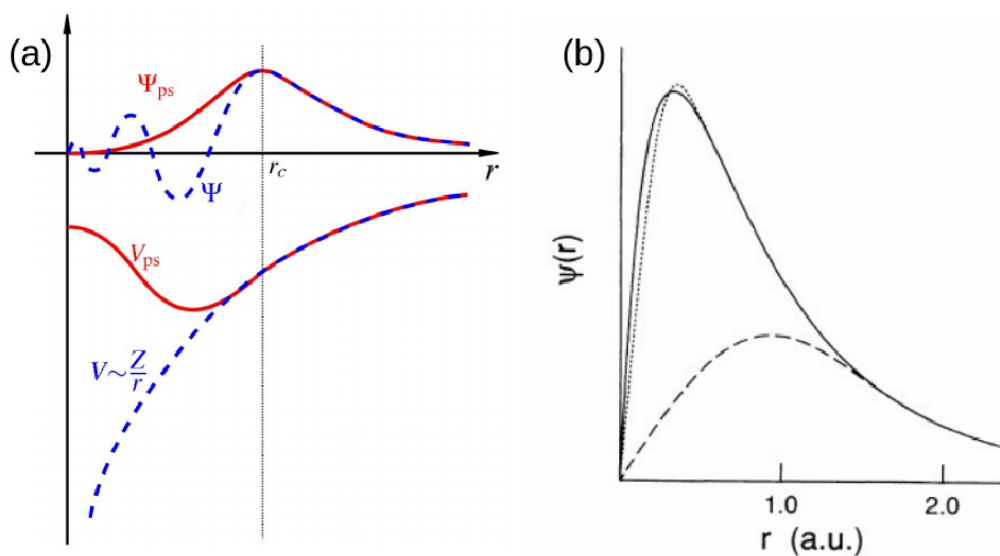


Figure 2.1: (a) Schematic diagram of all-electron (solid lines) and pseudoelectron (dashed lines) potentials and their corresponding wave functions. The radius at which all-electron and pseudoelectron values match is designated  $r_c$  (b) Oxygen 2p radial wave function (solid line) and corresponding norm-conserving (PRL 43, 1494(1979)) (dotted line) and ultrasoft (dashed line) pseudo wave functions. The figure is reproduced from Ref. PRB 41, 7892(1990).

the core region. The core region is defined by a cut-off radius  $r_c$  which includes all the nodes of the true valence wave functions. Thus  $\Psi_{ps}$  is constructed in such a way that it matches with the true valence wave function outside the core radius and nodeless inside the core radius.

The effective potential corresponding to this pseudo wave function  $\Psi_{ps}$  within the core region is called the pseudopotential  $V_{ps}$ . There are many schemes for construction of pseudopotentials from different authors such as Troullier and Martins[122, 123], Kerker[124], Hamann, Schlüter, and Chiang[125], Vanderbilt[126], Goedecker-Teter-Hutter[127].

In general, the construction of the pseudopotentials should be such that

(1) the eigen values of the pseudo-wave functions and all-electron wave functions should be identical for a chosen electronic configuration of the atom,

(2) both wave functions should be identical outside a cutoff radius  $r_c$ ,

(3) the pseudo-wave function should be node-less,

(4) the logarithmic derivative of both the wave functions should agree for  $r \geq r_c$ .

If the norm of the pseudo-wave function is equal to the norm of the all electron wave function within the core region, such pseudopotentials are called norm-conserving pseudopotentials. These are more accurate and have good transferability properties, *i.e.* the pseudopotential constructed in one environment (usually the atom) can faithfully describe the valence properties in different environments including atom, ions, molecules, and solids.

The main constraint with the norm-conserving pseudopotentials is that good transferability requires a core radius around the outermost maximum of the all-electron wave function, because only then the charge distribution and the moments of the all-electron wave function are well reproduced by the pseudo wave function. Therefore, for elements with strongly localized orbitals such as transition metals and rare-earth elements, the resulting pseudopotentials require large plane wave basis sets. Thus require a much more computational time and efforts. Vanderbilt[126] showed that this problem can be solved by relaxing the norm-conservation condition. This greatly reduced the energy cutoff because a large value of cut-off radius  $r_c$  could be used. The pseudo wave function  $\Psi_{ps}$  can be made much softer within the core region. However this results in the charge deficit

in the core region. To compensate for this deficit, the augmentation charges which are defined as the charge density difference between true and pseudo-wave functions, are introduced in the core region. The core radius  $r_c$  can now be chosen quite large independently of the position of the maximum of the all-electron wave function. Only for the augmentation charges, a small cutoff radius must be used to restore the moments and the charge distribution of the all-electron wave function accurately. These pseudopotentials are termed as ultra-soft pseudopotentials.

### 2.7.1 Projected Augmented Wave Method (PAW)

The major drawback of pseudopotential methods is that all information on the full wave function close to the nuclei is lost. This can influence the calculation of certain properties, such as hyperfine parameters, and electric field gradients. In 1994 Blöchl[128] developed the PAW method, which in principle is a frozen-core all electron method. It combines the advantage and accuracy of all-electron methods to computationally less expensive pseudopotential methods. Its close connection to the ultra-soft pseudopotential was derived by Kresse and Joubert in 1999[129].

The PAW method is based on the division of the whole space  $\Omega_w$  into distinct regions: a collection of non-overlapping spherical regions (the augmentation sphere) around each atom  $\Omega_a$  and the remainder, the interstitial region  $\Omega_1$ .

$$\Omega_w = \Omega_1 + \bigcup_a \Omega_a \quad (2.33)$$

The plane wave basis sets, which are ideal for the interstitial region  $\Omega_1$ , are difficult to use for the description of wave function in the augmentation spheres. This problem can be circumvented by introducing auxiliary smooth wave functions  $\tilde{\Psi}_i(\mathbf{r})$  which can be obtained from the all-electron wave function  $\Psi_i(\mathbf{r})$  via an invertible linear transformation  $\mathcal{T}$ .

$$|\Psi_i\rangle = \mathcal{T}|\tilde{\Psi}_i\rangle \quad (2.34)$$

where  $i$  is composite index for the band  $\mathbf{k}$  and spin. This transformation yields the transformed KS

equations.

$$\hat{H}_{KS}\Psi_i = \varepsilon_i\Psi_i \quad (2.35)$$

$$\hat{H}_{KS}\mathcal{T}\Psi_i = \varepsilon_i\mathcal{T}\Psi_i \quad (2.36)$$

$$\mathcal{T}^\dagger\hat{H}_{KS}\mathcal{T}\Psi_i = \mathcal{T}^\dagger\mathcal{T}\varepsilon_i\Psi_i \quad (2.37)$$

Auxiliary wave functions are obtained by solving eq. (2.37) and then transforming them back to true wave function using Eq. (2.35). The operator  $\mathcal{T}$  modifies the smooth auxiliary wave function in each atomic region, so that the resulting all-electron wave function has the correct nodal structure. It can be written as,

$$\mathcal{T} = 1 + \sum_a \mathcal{T}^a \quad (2.38)$$

where  $\mathcal{T}^a$  is the atom centered transformation and has no effect outside a certain atom specific augmentation region  $|\mathbf{r} - \mathbf{R}^a| < r_c^a$ . Here  $\mathbf{R}^a$  specify each lattice site. Hence the auxiliary and all-electron wave functions are identical outside the augmentation spheres. The cutoff region of radius  $r_c^a$  should be chosen such that there is no overlap between the augmentation spheres. Inside the augmentation spheres, the true wave function  $\Psi_i$  can be expanded in terms of partial waves  $\phi_i$ . For each of these partial waves, we can define a corresponding auxiliary smooth partial wave  $\tilde{\phi}_i$ , and write,

$$|\phi_i\rangle = (1 + \mathcal{T}^a)|\tilde{\phi}_i\rangle \quad (2.39)$$

$$\mathcal{T}^a|\tilde{\phi}_i\rangle = |\phi_i\rangle - |\tilde{\phi}_i\rangle \quad (2.40)$$

Hence for every atom, the local operator  $\mathcal{T}^a$  adds the difference between the true and auxiliary partial wave functions. This is schematically shown in fig.2.2. Any physical quantity can be evaluated by calculating the expectation value of the operator in terms of either the true or auxiliary wave function.

$$\langle A \rangle = \sum_n f_n \langle \Psi_i | A | \Psi_i \rangle = \sum_n f_n \langle \tilde{\Psi}_i | \mathcal{T}^\dagger A \mathcal{T} | \tilde{\Psi}_i \rangle \quad (2.41)$$

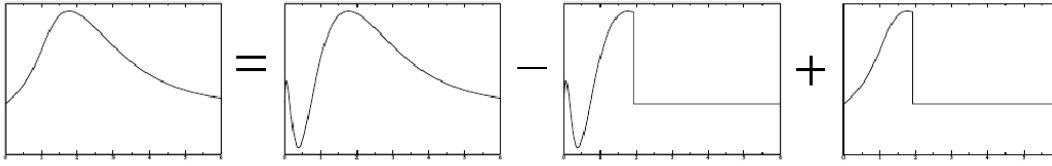


Figure 2.2: Schematic representation of the PAW transformation. The auxiliary wave function is constructed from the full wave function by subtracting the oscillatory part close to an atom and replacing it by a smooth function

where  $f_n$  are the occupation of the valence states.

Thus the PAW method an all-electron method and not a traditional pseudopotential method. It uses the information of full density and potential. The converged results of the PAW method do not depend on a reference system such as an isolated atom. There are no transferability errors and the high spin atoms can be described efficiently. Like other all-electron methods, the PAW method provides access to the full charge and spin density, which is relevant for many properties *e.g* hyperfine parameters.

## Geometry optimization

The main purpose of geometry optimization is to find the lowest energy structure of a system from an arbitrary starting geometry. Within Born-Oppenheimer approximation, the motion of the nuclei and the electrons can be separated, hence a geometry optimization is a two step process. (1) The electronic self consistent calculation for a given geometry, (2) the ionic relaxation of the nuclei according to the Hellmann-Feynman theorem[130].

The Hellmann-Feynman force acting on the  $I^{th}$  atom can be written as

$$\mathbf{F}_I = -\frac{\partial E_{total}}{\partial \mathbf{R}_I} = -\left[\frac{\partial E_N}{\partial \mathbf{R}_I} + \frac{\partial E}{\partial \mathbf{R}_I}\right] \quad (2.42)$$

$\mathbf{R}_I$  's is the position of the  $I^{th}$  atom. The forces due the electrons  $\mathbf{F}^e$  on the  $I^{th}$  nuclei can be written

as

$$\begin{aligned}
\mathbf{F}_I^e &= -\frac{\partial}{\partial \mathbf{R}_I} \langle \Psi_s | \hat{H}_e | \Psi_s \rangle \\
&= -\langle \Psi_s | \frac{\partial \hat{H}_e}{\partial \mathbf{R}_I} | \Psi_s \rangle - \langle \frac{\partial \Psi_s}{\partial \mathbf{R}_I} | \hat{H}_e | \Psi_s \rangle - \langle \Psi_s | \hat{H}_e | \frac{\partial \Psi_s}{\partial \mathbf{R}_I} \rangle
\end{aligned} \tag{2.43}$$

Since  $\Psi_s$  is an eigenfunction of  $\hat{H}_e$ ,

$$\begin{aligned}
\mathbf{F}_I^e &= -\langle \Psi_s | \frac{\partial \hat{H}_e}{\partial \mathbf{R}_I} | \Psi_s \rangle - E \langle \frac{\partial \Psi_s}{\partial \mathbf{R}_I} | \Psi_s \rangle - E \langle \Psi_s | \frac{\partial \Psi_s}{\partial \mathbf{R}_I} \rangle \\
&= -\langle \Psi_s | \frac{\partial \hat{H}_e}{\partial \mathbf{R}_I} | \Psi_s \rangle - E \frac{\partial}{\partial \mathbf{R}_I} \langle \Psi_s | \Psi_s \rangle
\end{aligned} \tag{2.44}$$

However  $\Psi_s$  are normalized  $\langle \Psi_s | \Psi_s \rangle = 1$  and last term in the above vanishes. Then total force on the  $I^{\text{th}}$  atom can be written as

$$\mathbf{F}_I = -\frac{\partial E_N}{\partial \mathbf{R}_I} - \langle \Psi_s | \frac{\partial \hat{H}_e}{\partial \mathbf{R}_I} | \Psi_s \rangle \tag{2.45}$$

Hence the forces on the nuclei can be calculated using Eq. (2.45). Once the forces are known, one can use optimization techniques such as the steepest descent (SD) or conjugate gradient (CG) method to move the nuclei towards the local minimum. This will generate a new nuclear configuration and the same process (electronic self-consistent cycle) will be repeated to calculate the forces in the new nuclear configuration using Eq. (2.50). Based on the new forces, again the nuclei are moved to new positions. The process continues till the force on each atom is below a given threshold value. At the end of this process, the nuclei reach an equilibrium configuration which is a local minimum of their potential energy surface (PES).

## 2.8 van der Waals corrections

It is well known that most popular DFT functionals such as LDA or GGA do not describe the long-range electron correlation that are responsible for the van der Waals (vdW) interactions. The dispersion interactions are viewed as non-local electron correlations, which cannot be captured by standard exchange-correlation functionals. An accurate and efficient estimation of vdW forces in conjunction with DFT functionals is non-trivial and is still a matter of discussion. One of the dispersion-corrected DFT approach was proposed by Grimme known as DFT-D2 (or DFT-D) method[131]. In this method, a semi-empirical attractive term is added to the DFT energy to account for medium and long-distance dispersive forces, so that total energy is now written as

$$E_{tot} = E_{DFT} + E_{disp} \quad (2.46)$$

where  $E_{DFT}$  is the DFT total energy computed with a given exchange-correlation functional and  $E_{disp}$  is a semi-empirical pair-wise dispersion correction given by

$$E_{disp} = -s_6 \sum_{i=1}^{N_{at}-1} \sum_{j=i+1}^{N_{at}} \frac{C_6^{ij}}{R_{ij}^6} f_{damp}(R_{ij}, R_0^{ij}) \quad (2.47)$$

Here  $N_{at}$  is the number of atoms in the system,  $s_6$  is a global scaling factor and depends on the exchange-correlation functional,  $C_6^{ij}$  s are the dispersion coefficients for the atom-pair  $ij$  and  $R_{ij}$  is the interatomic distance. For a pair of different elements, the value of  $C_6^{ij}$  s is taken as the geometric mean of the coefficients of individual elements.  $f_{damp}$  is a damping function which avoids divergence of the  $R_{ij}^6$  term at small distances and double-counting effects of correlation at intermediate distance. It determines the range of the dispersion correction.

$$f_{damp}(R_{ij}, R_0^{ij}) = \frac{1}{1 + \exp(-d \frac{R_{ij}}{s_{rn} R_0^{ij}} - 1)} \quad (2.48)$$

where  $R_0^{ij}$  is cutoff radius for the atom pair which is taken as the average of the empirical atomic vdW radii.  $d$  is the global constant that determines the steepness of the damping function (the higher the value of  $d$ , the closer it is to a step function), and  $s_{r,n}$  is a scaling factor and determines the range of interaction covered by the given DFT exchange-correlation functional. While using the DFT-D2 method, we used the PBE exchange correlation functional in the DFT part and the value of  $s_6$  is taken as 0.75. For all our calculation, we considered pair interactions up to a radius of 8 Å and used the default values of other parameters given in VASP.

In another approach the dispersion forces are treated within the DFT formalism by means of a non-local correlation functional. Dispersion forces result due to interactions between multipole moments arising out of charge density fluctuations around the atoms. DFT-D2 method only includes dipole-dipole interaction through a semi-empirical approach. Higher order interactions are, however, neglected. Dion et al.[132], have proposed a method which calculates the dispersion energy solely based on the electron density. Within this approach the exchange-correlation energy  $E_{xc}$  is calculated as

$$E_{xc} = E_x^{GGA} + E_c^{LDA} + E_c^{nl} \quad (2.49)$$

where  $E_x^{GGA}$  is the exchange energy in the revPBE approximation,  $E_c^{LDA}$  is the local correlation energy calculated within LDA, and  $E_c^{nl}$  represents the non-local term describing the dispersion energy and can be calculated as

$$E_c^{nl}[\rho] = \int d\mathbf{r}_1 d\mathbf{r}_2 \rho(\mathbf{r}_1) \phi(\mathbf{r}_1, \mathbf{r}_2) \rho(\mathbf{r}_2) \quad (2.50)$$

The kernel  $\phi(\mathbf{r}_1, \mathbf{r}_2)$  depends on the distance  $|\vec{r}_1 - \vec{r}_2|$ , charge density  $\rho$  and its gradient. This method is called as van der Waals density functional (vdW-DF) method. It adds the description of dispersion interactions within the DFT formalism and calculate the correlation of all ranges self-consistently. The biggest advantage of vdW-DF method over DFT-D2 method is that in this method dispersion effects are included naturally via the charge density and do not depend on any parameters.

## 2.9 Charge carrier mobility

An expression for mobility of charge carriers in a crystalline material can be derived based on the Boltzmann transport formalism and the relaxation time approximation. The relaxation time can be obtained by applying the deformation potential theory. The effective mass approximation and the first-principles derivation of the parameters in the mobility expression are discussed.

### 2.9.1 Boltzmann transport theory

The electron distribution  $f_i(\mathbf{r}, \mathbf{k}, t)$  undergoes deformation with an external field and the Boltzmann transport theory assumes that the scatterings restore the distribution function to the original one. Under the steady state condition, we have

$$\frac{\partial f_i(\mathbf{r}, \mathbf{k}, t)}{\partial t} \Big|_{diffusion} + \frac{\partial f_i(\mathbf{r}, \mathbf{k}, t)}{\partial t} \Big|_{drift} + \frac{\partial f_i(\mathbf{r}, \mathbf{k}, t)}{\partial t} \Big|_{scattering} = 0. \quad (2.51)$$

If we only consider the weak external direct current (DC) electric field

$$\frac{\partial f_i(\mathbf{r}, \mathbf{k}, t)}{\partial t} \Big|_{drift} = -\mathbf{k} \cdot \frac{\partial f}{\partial \mathbf{k}} = -\frac{e}{\hbar} \mathbf{E} \cdot \nabla_{\mathbf{k}} f_i(\mathbf{r}, \mathbf{k}, t) \quad (2.52)$$

and we ignore the diffusion term, then eqn (2.51) becomes

$$-\frac{e}{\hbar} \mathbf{E} \cdot \nabla_{\mathbf{k}} f_i(\mathbf{k}) = \frac{\partial f_i(\mathbf{k})}{\partial t} \Big|_{scattering}, \quad (2.53)$$

where  $\mathbf{r}, t$  are omitted for simplicity,  $\mathbf{E}$  is the external electric field and  $i$  is the band index. The relaxation-time approximation assumes

$$\frac{\partial f_i(\mathbf{k})}{\partial t} \Big|_{scattering} = \frac{f_i(\mathbf{k}) - f_i^0(\mathbf{k})}{\tau_i(\mathbf{k})} \quad (2.54)$$

where  $f_i^0(\mathbf{k})$  is the equilibrium Fermi-Dirac distribution, while  $f_i(\mathbf{k})$  is the local concentration of electron in the state  $(i, \mathbf{k})$  in the neighbourhood of the point  $\mathbf{r}$  in the space and is assumed to deviate

not far from  $f_i(\mathbf{k})$ .  $\tau_i(\mathbf{k})$  is the relaxation-time from the deviated electron distribution function to equilibrium distribution function (from  $f_i(\mathbf{k})$  to  $f_i^0(\mathbf{k})$ ) when the external field is removed. Substituting eqn (3) into eqn (4), and neglecting the second-order term, we get

$$f_i(\mathbf{k}) \approx f_i^0(\mathbf{k}) + e\tau_i(\mathbf{k}) \frac{\partial f_i^0(\mathbf{k})}{\partial \varepsilon_i(\mathbf{k})} \mathbf{E} \cdot \mathbf{v}_{ik} \quad (2.55)$$

By definition, the mobility  $\mu_\beta$  is the ratio between the drift velocity  $\langle v_\beta \rangle$ , and the electric field  $E_\beta$  in the  $\beta$  direction,

$$\mu_\beta^{e(h)} = \frac{\langle v_\beta \rangle}{E_\beta} = \frac{\sum_{i \in CB(VB)} \int v_\beta(i, \mathbf{k}) f_i(\mathbf{k}) d\mathbf{k}}{E_\beta \sum_{i \in CB(VB)} \int f_i(\mathbf{k}) d\mathbf{k}} \quad (2.56)$$

The integral in the denominator of eqn (2.56) for electrons and holes can be expressed as

$$\int f(\mathbf{k}) d\mathbf{k} \approx \sum_{i \in CB} \int f_0[\varepsilon_i(\mathbf{k}) - \mu] d\mathbf{k} \quad (2.57)$$

and

$$\int f(\mathbf{k}) d\mathbf{k} \approx \sum_{i \in VB} \int (1 - f_0[\varepsilon_i(\mathbf{k}) - \mu]) d\mathbf{k} \quad (2.58)$$

where  $\mu$  is the chemical potential. Correspondingly, substituting eqn (2.55) into eqn (2.56) and normally the band gap is much larger than  $k_B T$ , we can replace the Fermi-Dirac distribution with the Boltzmann distribution. Finally the electron (hole) mobility can be expressed as

$$\mu_\beta^{e(h)} = \frac{e}{k_B T} \frac{\sum_{i \in CB(VB)} \int \tau_\beta(i, \mathbf{k}) v_\beta^2(i, \mathbf{k}) \exp[\mp \frac{\varepsilon_i(\mathbf{k})}{k_B T}] d\mathbf{k}}{\sum_{i \in CB(VB)} \int \exp[\mp \frac{\varepsilon_i(\mathbf{k})}{k_B T}] d\mathbf{k}} \quad (2.59)$$

where the - (+) sign is for electron (hole). The group velocity  $v_\beta(i, \mathbf{k})$  and band energy  $\varepsilon_i(\mathbf{k})$  can be determined from DFT calculations. The key is to calculate the electron (hole) relaxation-time  $\tau_\beta(i, \mathbf{k})$ . The scattering term can be expressed as

$$\frac{\partial f_i(\mathbf{k})}{\partial t} \Big|_{scattering} = \sum_{\mathbf{k}', j} (W(j\mathbf{k}', i\mathbf{k}) f_j(\mathbf{k}') [1 - f_i(\mathbf{k})] - W(i\mathbf{k}, j\mathbf{k}') f_i(\mathbf{k}) [1 - f_j(\mathbf{k}')]) \quad (2.60)$$

where  $W(i\mathbf{k}, j\mathbf{k}')$  is the transition probability from electronic state  $(i, \mathbf{k})$  to  $(j, \mathbf{k}')$  and is given by

$$\sum_{\mathbf{k}', j} W(i\mathbf{k}, j\mathbf{k}') = \frac{2\pi}{\hbar} \sum_{\mathbf{k}', j} |M(i\mathbf{k}, j\mathbf{k}')|^2 \delta[\varepsilon_i(\mathbf{k}) - \varepsilon_i(\mathbf{k}')] \quad (2.61)$$

Here  $i, j$  are the band indexes and  $\mathbf{k}, \mathbf{k}'$  are the electron wave vectors. The matrix element  $M(i\mathbf{k}, j\mathbf{k}') = \langle j, \mathbf{k}' | \Delta V | i, \mathbf{k} \rangle$  describes the scattering from state  $(i, \mathbf{k})$  to state  $(j, \mathbf{k}')$  by the deviation potential arising from the atomic displacement associated with the phonons or the perturbation potential caused by defects or impurities. At the thermal equilibrium,

$$W(j\mathbf{k}', i\mathbf{k}) f_j^0(\mathbf{k}') [1 - f_i^0(\mathbf{k})] = W(i\mathbf{k}, j\mathbf{k}') f_i^0(\mathbf{k}) [1 - f_j^0(\mathbf{k}')] \quad (2.62)$$

Using Fermi-Dirac distribution, it can be further simplified as:

$$W(j\mathbf{k}', i\mathbf{k}) \exp(\varepsilon_i(\mathbf{k})/k_B T) = W(i\mathbf{k}, j\mathbf{k}') \exp(\varepsilon_i(\mathbf{k}')/k_B T) \quad (2.63)$$

For elastic scattering  $\varepsilon_i(\mathbf{k}) = \varepsilon_i(\mathbf{k}')$ , we can have  $W(j\mathbf{k}', i\mathbf{k}) = W(i\mathbf{k}, j\mathbf{k}')$ , thus equation (2.60) can be expressed as

$$\frac{\partial f_i(\mathbf{k})}{\partial t} \Big|_{scattering} = \sum_{\mathbf{k}', j} W(i\mathbf{k}, j\mathbf{k}') [f_i(\mathbf{k}') - f_i(\mathbf{k})] \quad (2.64)$$

Combining equation (2.60), (2.53), (2.54), (2.63), the relaxation-time is expressed as

$$\frac{1}{\tau(i, \mathbf{k})} = \frac{2\pi}{\hbar} \sum_{\mathbf{k}', j} |M(i\mathbf{k}, j\mathbf{k}')|^2 \delta[\varepsilon_i(\mathbf{k}) - \varepsilon_i(\mathbf{k}')] \left[ 1 - \frac{\tau(j, \mathbf{k}') v(j, \mathbf{k}') \cdot \mathbf{e}_E}{\tau(i, \mathbf{k}') v(i, \mathbf{k}') \cdot \mathbf{e}_E} \right] \quad (2.65)$$

where  $\mathbf{e}_E$  is the unit vector along the electric field. In principle, eqn (2.65) can be solved iteratively.

To avoid the iteration, eqn (2.65) is approximated as

$$\frac{1}{\tau_\beta(i, \mathbf{k})} = \frac{2\pi}{\hbar} \sum_{\mathbf{k}', j} |M(i\mathbf{k}, j\mathbf{k}')|^2 \delta[\varepsilon_i(\mathbf{k}) - \varepsilon_i(\mathbf{k}')] \left[ 1 - \frac{v_\beta(j, \mathbf{k}')}{v_\beta(i, \mathbf{k})} \right] \quad (2.66)$$

$[1-v_{\beta}(j,\mathbf{k}')/v_{\beta}(i,\mathbf{k})]$  describes the scattering angle weighting factor in the external field direction of  $\beta$ . Now, the difficulty is to calculate the scattering matrix element. Here we only consider the dominant scattering of a thermal electron or hole by acoustic phonon within the DP theory.

The DP theory was proposed by Bardeen and Shockley in 1950s to describe the charge transport in non-polar semiconductors. Since the electron velocity with energy  $k_B T$  at 300 K is about  $10^7$  cm/s, and the corresponding wavelength is 7 nm, according to  $\lambda = h/(mv)$ , which is much larger than the lattice constant, thus the electron is scattered mainly by the acoustic phonons.

The DP theory assumes that the lattice potential perturbation due to thermal motions  $\Delta V(\mathbf{r})$  has a linear dependence on the relative volume change  $\Delta(\mathbf{r})$ . Namely,  $\Delta V(\mathbf{r}) = E_1 \Delta(\mathbf{r})$ , where  $E_1$  is defined as the DP constant. The displacement at lattice site associated with the acoustic phonon with wave-vector  $\mathbf{q}$  is

$$u(\mathbf{r}) = \frac{1}{\sqrt{N}} \mathbf{e}_{\mathbf{q}} [a_{\mathbf{q}} e^{i\mathbf{q}\cdot\mathbf{r}} + a_{\mathbf{q}}^* e^{-i\mathbf{q}\cdot\mathbf{r}}] \quad (2.67)$$

where  $N$  is the number of lattice sites in the unit volume.  $\mathbf{e}_{\mathbf{q}}$  and  $a_{\mathbf{q}}$  are the unit vector and amplitude of the acoustic phonon  $\mathbf{q}$ . The relative volume change can be expressed as

$$\Delta(\mathbf{r}) \equiv \frac{\partial u(\mathbf{r})}{\partial \mathbf{r}} = \frac{i}{\sqrt{N}} \mathbf{q} \cdot \mathbf{e}_{\mathbf{q}} [a_{\mathbf{q}} e^{i\mathbf{q}\cdot\mathbf{r}} - a_{\mathbf{q}}^* e^{-i\mathbf{q}\cdot\mathbf{r}}] \quad (2.68)$$

From eqn (2.68), it is found that only the LA wave contributes to the deformation. So the matrix element for electron (hole) to be scattered from Bloch state  $|i, \mathbf{k}\rangle$  to  $|i, \mathbf{k}'\rangle$  can be expressed as

$$|M(i\mathbf{k}, i\mathbf{k}')|^2 = |\langle i, \mathbf{k} | \Delta V | i, \mathbf{k}' \rangle|^2 = \frac{1}{N} (E_1^i)^2 q^2 a_{\mathbf{q}}^2 \quad (2.69)$$

where  $\mathbf{q} = \pm(\mathbf{k}' - \mathbf{k})$ . At high temperature, when the lattice waves are fully excited, the amplitude of the wave is given by  $a_{\mathbf{q}} = k_B T / (2mq^2 v_a^2)$  according to the uniform energy partition theory, where  $m$  is the total mass of lattice in the unit volume, and  $v_a$  is the velocity of the acoustic wave. Finally,

the average scattering probability becomes

$$\langle |M(i\mathbf{k}, i\mathbf{k}')|^2 \rangle = \frac{k_B T (E_\beta^i)^2}{C_\beta} \quad (2.70)$$

where  $C_\beta = \rho v_a^2 = N m v_a^2$  is the elastic constant for the longitudinal strain in the direction of propagation of the LA wave ( $\beta$ ).  $E_\beta^i$  is the DP constant of the  $i$ -th band. We assume that the scattering matrix element is independent of state  $\mathbf{k}$  or  $\mathbf{k}'$ , and the charge transport direction (electric field direction) is parallel to the wave vector of LA phonon. The relaxation-time of the LA phonon scattering by DP theory can be expressed as

$$\frac{1}{\tau_\beta(i, \mathbf{k})} = \frac{2\pi k_B T (E_\beta^i)^2}{\hbar} \sum_{\mathbf{k}'} \delta[\varepsilon_i(\mathbf{k}) - \varepsilon_i(\mathbf{k}')] \left[ 1 - \frac{v_\beta(j, \mathbf{k}')}{v_\beta(i, \mathbf{k})} \right] \quad (2.71)$$

Combining eqn (2.59) and (2.71), the charge relaxation-time  $\tau$  and mobility  $\mu$  can be calculated once the band structure, DP constant  $E_i^\beta$  and the elastic constant  $C_\beta$  are determined.

Density of states effective mass in two dimension is  $m_a = \sqrt{m_\parallel m_\perp}$ .

The mobility in 2D system is

$$\mu_{2D} = \frac{e \langle \tau_\beta \rangle}{m_\parallel^*} = \frac{e \hbar^3 C_{2D}}{k_B T m_\parallel^* m_a^* (E_1)^2} \quad (2.72)$$



## Chapter 3

# Strain engineering in mobility in monolayer black phosphorus

Since the interest in phosphorene is because of its favorable properties for electronic applications, a fundamental quantity of interest is carrier mobility. Qiao et al [133] have calculated mobility in mono-layer to five-layer phosphorene samples using a simple phonon-limited scattering model. In agreement with the experiments of Liu et al.[108], they find both electron and hole mobility to be highly anisotropic. The anisotropy is particularly strong in a mono-layer, and decreases significantly in a five-layer sample. The hole mobility in a mono-layer shows a particularly strong anisotropy with a very large value ( $10,000 - 26,000 \text{ cm}^2 / \text{V.s}$ ) in the zigzag (shown in fig 3.1) direction.

While pristine phosphorene already has useful properties, further ability to tune these would render it suitable for specific applications. Strain engineering has proved to be a useful practical way of tuning electronic, transport and optical properties of semiconductors. Theoretical studies have been undertaken to understand effects of strain on the properties of phosphorene.

Elahi et al[134] have studied variation of effective mass with strain, but have not calculated change of mobility. Mobility as a function of strain is calculated by a couple of groups [135, 136]. They also found that electron mobility is anisotropic in both mono-layer and bi- layer phospho-

rene. Application of both uniaxial and biaxial tensile strain eventually reverses the direction of easy transport. In a pristine phosphorene sheet, electron mobility is much higher in the armchair direction than that in the zigzag direction. 3 – 4% biaxial tensile strain or 5 – 6% uniaxial tensile strain along the zigzag direction makes the electron mobility along this direction larger than the mobility along the armchair direction.

As we mentioned earlier, in a mono-layer phosphorene, hole mobility is far higher than electron mobility, and hence may play a dominant role. Variation of electron mobility with strain along the armchair direction, or with compressive strain was also not studied. These authors have not given values of the DP, or how these have been calculated.

In this chapter we perform a thorough study of variation of both electron and hole mobility in a mono-layer phosphorene sheet along the zigzag, armchair directions, with compressive as well as tensile strain. In general one expects mobility to increase (decrease) with increasing compressive (tensile) strain. Since mobility has an inverse relation to the carrier effective mass, increase in the latter leads to a decrease in the latter. This is what happens for uniaxial strain along armchair direction for both electron and hole mobilities. But strain along the zigzag direction leads to unexpected changes in the hole and electron effective masses and DPs. This leads to non-monotonic variation of carrier mobility with strain along zigzag direction. Hole mobility can also be tuned by two orders of magnitude along this direction using only few percent strain. These two properties make phosphorene an attractive candidate material for tunable 2D electronics.

### **3.1 Computational details**

The results of mobility under various strain are obtained using Vienna ab-initio simulation package (VASP) based on plane wave basis set. The kinetic energy cut off is set 500 eV for plane wave basis set. Interactions between valence electrons and the ion cores are represented by projector augmented wave (PAW) potentials. Mobility, a model based quantity depend on effective mass and deformation potential. Both the effective mass and deformation potential has dependence on

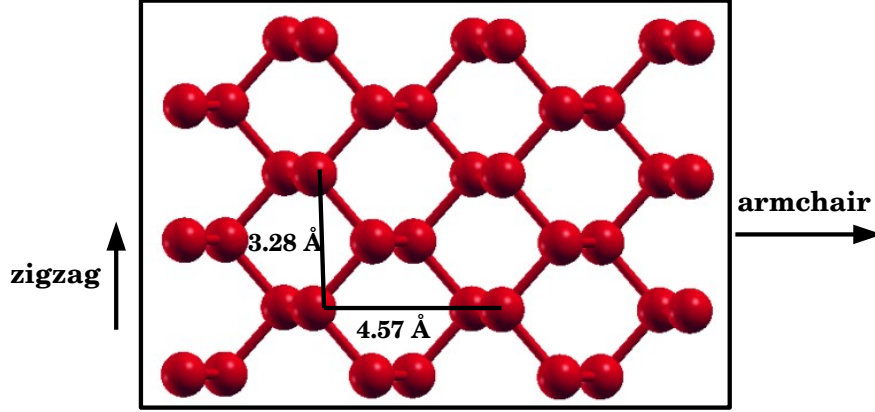


Figure 3.1: Structure of monolayer black phosphorus. Armchair and zigzag directions are marked

band structure of phosphorene. Therefore we have employed HSE06 functional to calculate band structure. We have performed the structure relaxation calculation for all strains using hybrid corrected PBE exchange correlation functional (HSE06). Both the electronic structure and structural relaxation in all strains we have used HSE06 method. In all strain calculation the atoms are relaxed until the force on atoms are less than  $0.01 \text{ eV/\AA}$ .

Brillouin zone integration is performed with Monkhorst-pack k-mesh of size  $10 \times 12 \times 1$ . We have used k space mesh gap of value  $0.006 \text{ \AA}^{-1}$  for band structure calculation. A single phosphorene sheet is represented in a repeated slab geometry. The simulation cell contains a single sheet and a vacuum of  $24 \text{ \AA}$  so that there are no interactions between periodic images.

## 3.2 Results

Before doing calculations at finite strain, we calculated structural and electronic properties of a pristine phosphorene sheet. Phosphorene has a rectangular unit cell with four atoms in the cell. The edges of the unit cell along these two directions have armchair and zigzag structures respectively. We will take the x and y Cartesian directions along the armchair and zigzag directions. Our calculated lattice constants along x and y in HSE06 are  $4.57 \text{ \AA}$  and  $3.28 \text{ \AA}$  respectively. Structure of a mono-layer phosphorene is shown in fig 3.1. We have marked the armchair and zigzag directions for ease of further discussion. For uniaxial strain  $\varepsilon = \Delta l/l_0$ .  $\Delta l$  is the change in the lattice

constant due to strain, and  $l_0$  is the equilibrium lattice constant ( $a_0$  along armchair direction and  $b_0$  along zigzag direction).

$$\Delta l = (a_{strain} - a_0) / a_0 \text{ along armchair direction and}$$

$$\Delta l = (b_{strain} - b_0) / b_0 \text{ along zigzag direction}$$

where  $a_{strain}$  and  $b_{strain}$  are strained lattice constants along armchair and zigzag directions respectively.

Within a phonon-limited scattering model, carrier mobility in a 2D materials calculated using the following relation as discussed in chapter 2.

$$\mu_{2D} = \frac{e\hbar^3 C_{2D}}{k_B T m_{\parallel}^* m_a^* (E_1)^2}. \quad (3.1)$$

In this relation  $m_{\parallel}^*$  is the effective mass of the carrier (electrons or holes) in the transport direction, and  $m_a^* = \sqrt{m_{\parallel}^* m_{\perp}^*}$  is the geometric mean of the effective masses along the two directions,  $m_{\perp}^*$  being the effective mass perpendicular to the transport direction.  $E_1$  the DP of the valence band maximum (VBM) for hole conduction, or of the conduction band minimum (CBM) for electron conduction.  $E_1$  is calculated as

$$E_1 = \frac{\Delta E_e}{\epsilon} \quad (3.2)$$

where  $\Delta E_e$  is the shift of the band edge (VBM or CBM) due to a strain  $\epsilon$ . Position of the band edges ( $E_e$ ) are calculated relative to the vacuum energy. Although the vacuum energy in a finite simulation cell does not become zero, the location of the band edges relative to the vacuum energy converged at a vacuum length of 12 Å. We always consider transport in the uniaxial strain direction.  $C_{2D}$  is the elastic modulus of the 2D sheet, and is calculated using the relation,

$$\frac{\Delta E}{S_0} = \frac{1}{2} C_{2D} \epsilon^2. \quad (3.3)$$

Here  $\Delta E$  is the change in total energy of the phosphorene sheet of area  $S_0$  at equilibrium due to a uniaxial strain  $\epsilon$ . The elastic constants along armchair and zigzag directions are 26.6 and 105.86

$\text{J/m}^2$ .

Carrier effective masses are obtained from a quadratic fit to the topmost valence band (for holes) or the lowermost conduction band (for electrons) energies as a function of wave number  $k$ . As reported by us and other workers, in pristine phosphorene, and also under compressive strains, the VBM occurs slightly away from the  $\Gamma$ -point of the 2D BZ, while the CBM occurs exactly at the  $\Gamma$ -point. The situation changes at about 2% of tensile strain, beyond which the VBM moves to the  $\Gamma$ -point. For fit to the valence band, energies are always taken relative to the VBM whether that is at the  $\Gamma$ -point, or away from it. The DP is obtained from a linear fit of  $\Delta E_e$  to the strain  $\varepsilon$ . Slope of the best linear fit is taken as  $E_1$ . In this work we consider uniaxial strain in the range of  $-6\%$  to  $6\%$  along two directions (zigzag and armchair). The negative (positive) sign corresponds to the compressive (tensile) strain. Based on physical understanding the compressive (tensile) uniaxial strain along one direction increases(decreases) the lattice constant along transverse direction. The Poisson's ratio is 0.18 and 0.57 along zigzag and armchair direction respectively. We have studied uniaxial strain on phosphorene under two different conditions (i) transverse direction is fixed and (ii) transverse direction is relaxed using energy minimization technique. In both cases we have some common variation of features in the band structure and eventually in the effective mass and DP, which we will discuss in the subsequent paragraph.

First we discuss effects of strain on the band structure. The variation of band gap with uniaxial strain is shown in fig 3.2. As already mentioned, in pristine phosphorene, and in phosphorene under uniaxial compressive strain along two directions, the band gap is indirect. The situation remains the same for tensile strains up to 6% along the armchair direction. But interesting changes in the electronic structure take place for tensile strain  $\sim 2\%$  along the zigzag direction. The VBM moves to the  $\Gamma$ -point beyond this strain. Associated with this a significant change in the valence band dispersion that affects the hole effective mass. A more significant effect of tensile strain along the zigzag direction is seen in the conduction band. Fig 3.3 shows the band structures of phosphorene under various strain conditions. Band structure for pristine phosphorene is plotted in fig 3.3 (a). Along with the CBM, there is a second band at the  $\Gamma$ -point which is  $\sim 0.68$  eV

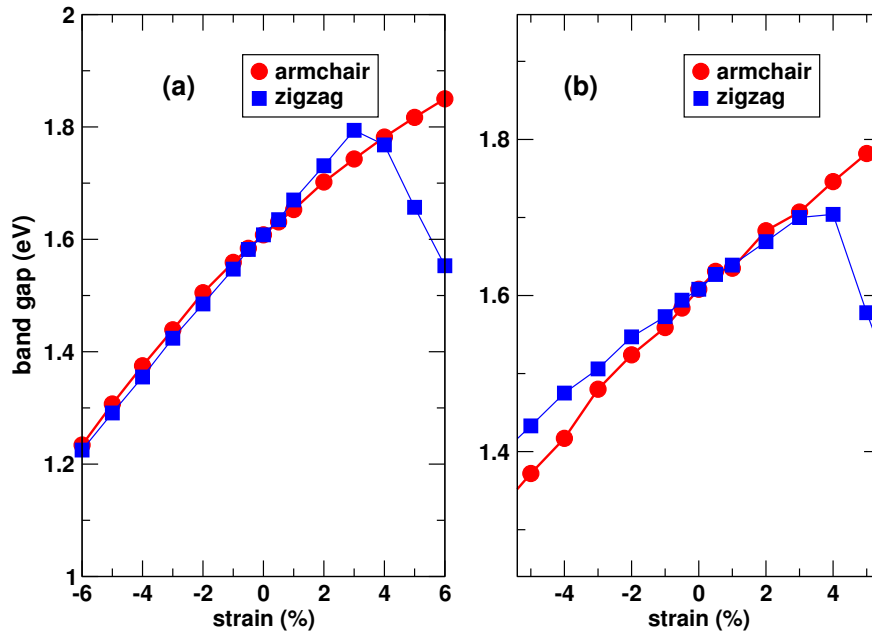


Figure 3.2: Variation of band gap with strain along different direction when (a) transverse directions are fixed, (b) transverse directions are relaxed .

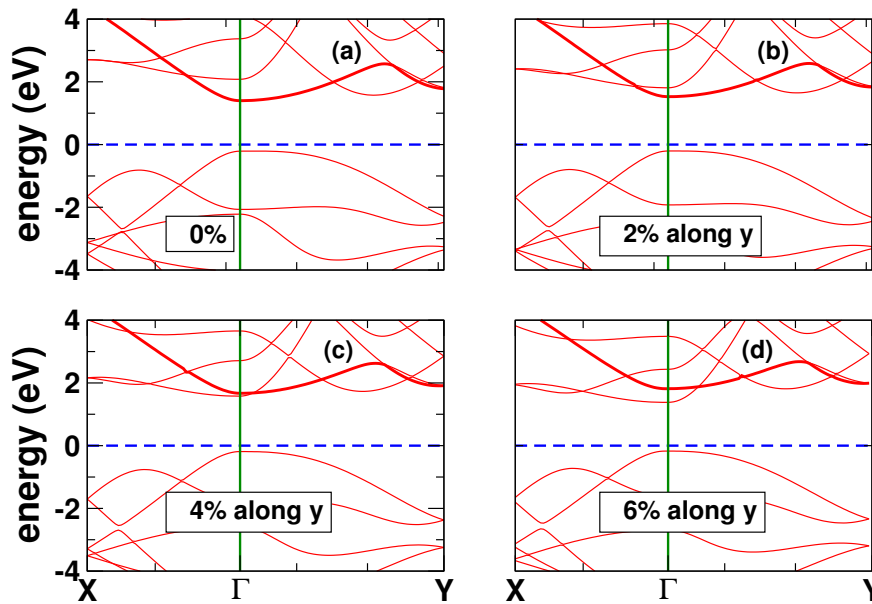


Figure 3.3: Band structure of mono-layer phosphorene under different strain conditions along the zigzag direction.

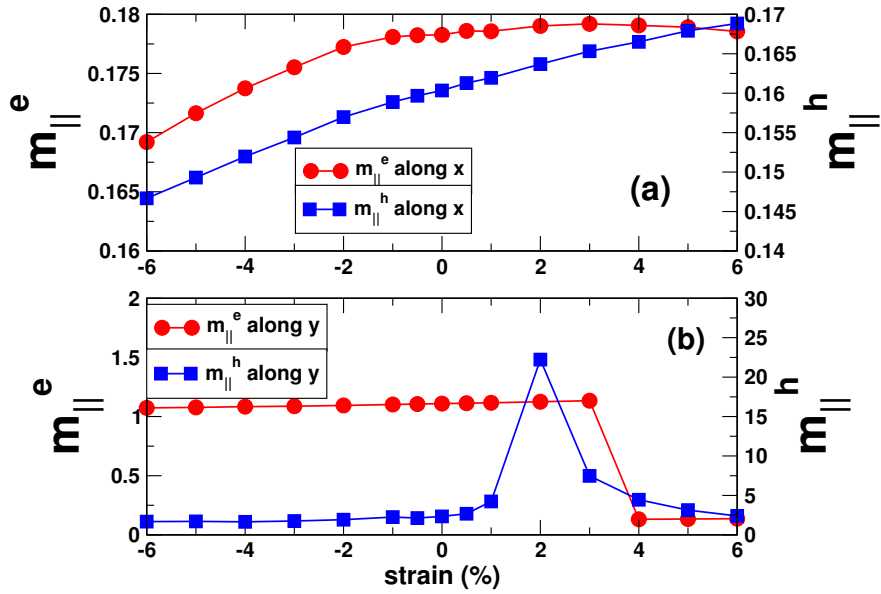


Figure 3.4: Variation of electron and hole effective mass with strain along different direction when transverse directions are fixed. Effective masses are calculated along the strain directions in each case.

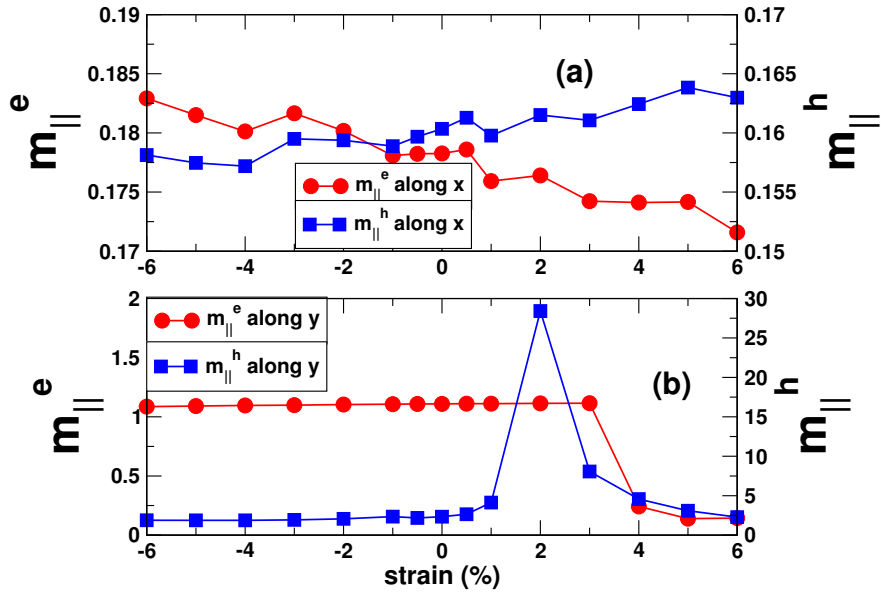
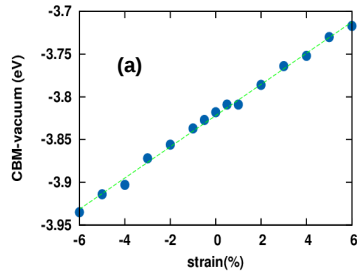
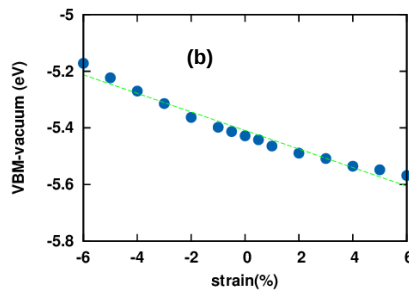


Figure 3.5: Variation of electron and hole effective mass with strain along different direction when transverse directions are relaxed. Effective masses are calculated along the strain directions in each case.

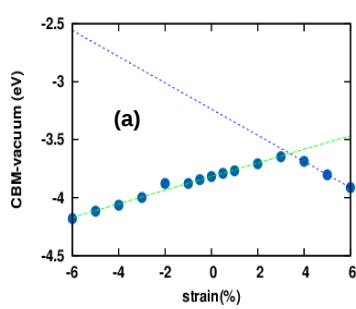


Slope of the straight line = 1.8 eV



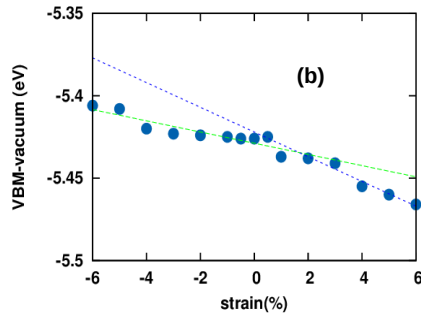
Slope of the straight line = -3.27 eV

Figure 3.6: Deformation potential of (a) electron and (b) hole along armchair direction when strain is along armchair direction and zigzag direction is fixed.



Slope of straight line (-6% to 3% strain) = 5.8 eV (green dotted line)

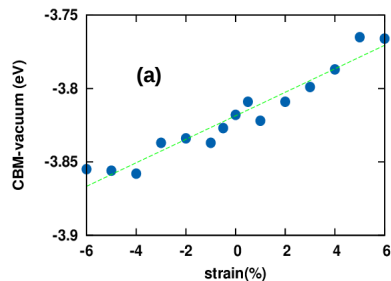
Slope of straight line (4% to 6% strain) = -11.3 eV (blue dotted line)



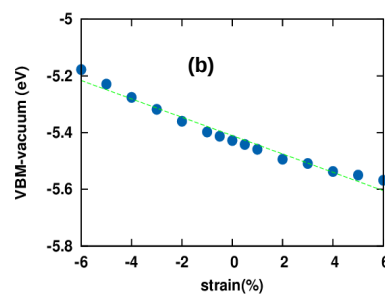
Slope of straight line (-6% to 1% strain) = -0.34 eV (green dotted line)

Slope of straight line (2% to 6% strain) = -0.75 eV (blue dotted line)

Figure 3.7: Deformation potential of (a) electron and (b) hole along zigzag direction when strain is along zigzag direction and armchair direction is fixed.



Slope of straight line = 0.8 eV



Slope of straight line = -3.24 eV

Figure 3.8: Deformation potential of (a) electron and (b) hole along armchair direction when strain is along armchair direction and zigzag direction is relaxed.

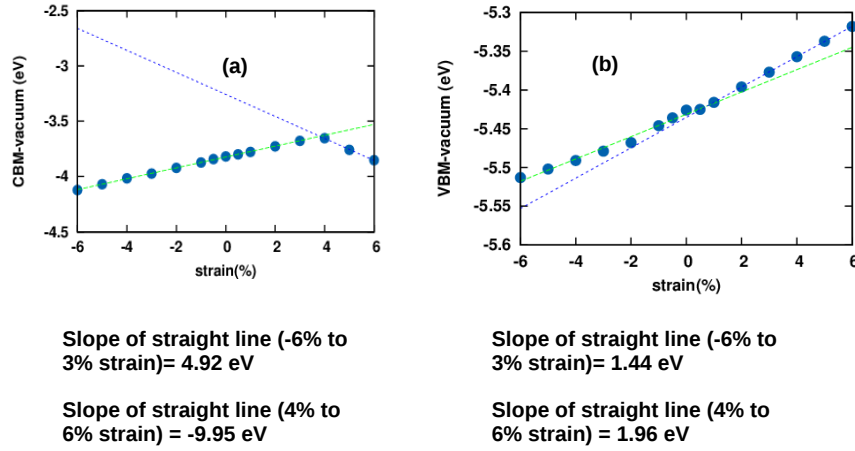


Figure 3.9: Deformation potential of (a) electron and (b) hole along zigzag direction when strain is along zigzag direction and armchair direction is relaxed.

higher. As the tensile strain increases, this higher-lying band comes down in energy, and the CBM is pushed up. Eventually, somewhere between 4% and 5% strain, the two bands cross each other at the  $\Gamma$ -point, and therefore, the character of the CBM changes. This is clearly seen in the band structure at the 6% strain in fig 3.3 (d).

As expected, strain affects the carrier effective masses also. Variation of effective mass with strain is shown in fig 3.4 and 3.5. The numerical values of effective masses are given in tables 3.3-3.10. Changes of hole and electron effective masses with strain are monotonic for strain along the armchair direction. However, changes in the effective mass is not always so benign. Particularly interesting variation in hole effective mass is observed beyond 2% tensile strain along zigzag direction, the point at which the VBM moves to the  $\Gamma$  point. Beyond this strain, the hole effective mass decreases with increase of strain up to 6%. Upto 2% strain along zigzag direction the VBM is in between  $\Gamma$  and Y and after that VBM is at  $\Gamma$ .

Crossover of the two conduction bands leads to significant changes in the electron effective mass. It is clear in fig 3.3 (a) that the CBM in pristine phosphorene is more dispersive along the armchair ( $\Gamma$ -X) direction than along the zigzag ( $\Gamma$ -Y) direction. This leads to a lower electron effective mass along  $\Gamma$ -X. But as seen in fig 3.3 (d), at 6% strain along the zigzag direction, the new CBM is more dispersive along  $\Gamma$ -X. This causes the electron effective mass along the zigzag

direction to become smaller than that along the armchair direction at strains 5% or higher.

Let us now discuss the effect of strain on the band edges which determine the DPs (shown in figures 3.6, 3.7, 3.8, 3.9). Strain along the armchair direction leads to monotonic shifts in both the conduction and valence band edges. Good straight line fits are obtained for the variation of band edge energies with strain and the numbers are given in table 3.1 and 3.2. Very interesting features are obtained for strain along the zigzag direction as shown in figures 3.7 and 3.9. Associated with the shift of the VBM to the  $\Gamma$  point at  $\sim 2\%$ , there is also a change in slope of the band edge energy (as shown in fig 3.7 (b) and 3.9 (b)). This changes the DP for holes for higher strains. Thus two different DPs given by slopes of the two different straight lines are used in different strain regimes for calculation of hole mobility. For the conduction band edge, the effect is even more dramatic (for both cases when armchair direction relaxed and fixed). Beyond 4% not only the value, the sign of the slope also changes (as shown in fig 3.7(a) and 3.9(a)). This is due to the fact that a different band now forms the CBM. Again, two different DPs are used for calculation of electron mobility in the two regimes. Beyond 4% strain, the slope and value of the DP changes.

Finally, we discuss the variation of electron and hole mobilities along the two principal directions due to uniaxial strain under two different conditions as mentioned above. Variation of both electron and hole mobilities along the armchair direction is rather featureless when the transverse direction is fixed as shown in fig 3.6 (a) and 3.7 (a). Since the DP remains a constant, and the effective masses increase monotonically, both electron and hole mobilities show monotonic decrease. The electron mobility changes from 2641.9  $\text{cm}^2/\text{V.s}$  to 2337.82  $\text{cm}^2/\text{V.s}$  over a strain range of  $-6\%$  to  $6\%$ . Variation of electron mobility along armchair direction when transverse direction is relaxed changes from 10898.06  $\text{cm}^2/\text{V.s}$  to 11584.7  $\text{cm}^2/\text{V.s}$  over a strain range of  $-6\%$  to  $6\%$ . In this case the DP is constant but the effective mass of electrons does not show monotonic change. This results a non-monotonic variation of mobility as shown in fig 3.7(a).

Variation of electron and hole mobility along the zigzag direction show interesting features as shown in fig 3.6 (b) and 3.7 (b). Electron mobility along zigzag direction when transverse direction is fixed decreases monotonically with increasing tensile strain from  $-6\%$  to  $3\%$ . It becomes 126.91

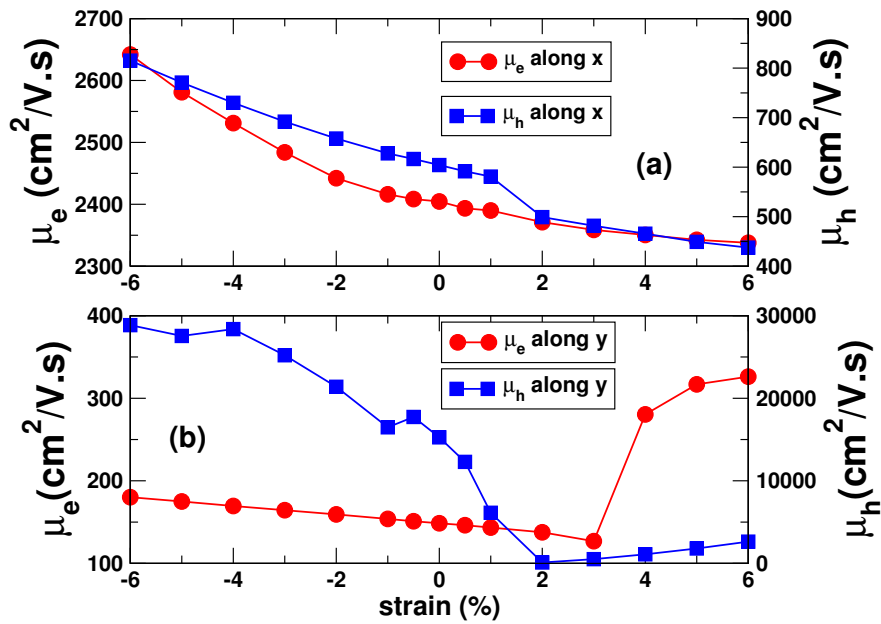


Figure 3.10: Variation of electron and hole mobility with strain along armchair and zigzag directions while transverse direction is fixed.

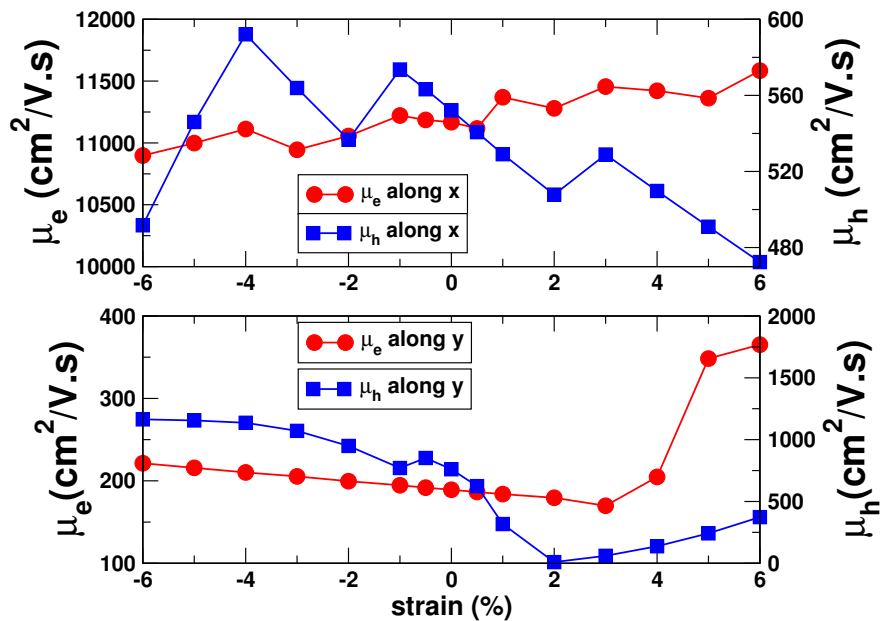


Figure 3.11: Variation of electron and hole mobility with strain along armchair and zigzag directions while transverse direction is relaxed.

$\text{cm}^2/\text{V.s}$  at 3% from  $180.19 \text{ cm}^2/\text{V.s}$  at  $-6\%$ . From 4% strain, due to change in the electron effective mass and DP, mobility shows a sudden increase, and becomes  $\sim 280.51 \text{ cm}^2/\text{V.s}$  at 4% strain. This increasing trend continues and the mobility becomes  $326.22 \text{ cm}^2/\text{V.s}$  at 6% strain. Electron mobility along zigzag direction when transverse direction is relaxed becomes  $221.34 \text{ cm}^2/\text{V.s}$  at  $-6\%$  strain and  $169.81$  at 3% strain. At 4% strain the electron mobility becomes  $204.74$  and increases upto  $365.27 \text{ cm}^2/\text{V.s}$  at 6% strain.

Variation of hole mobility along zigzag direction shows the most interesting features. Hole mobility along zigzag direction when transverse direction is fixed keeps decreasing, and becomes  $102.14 \text{ cm}^2/\text{V.s}$  at 2% strain. Beyond this due to a sudden increase in the hole DP, mobility suddenly jumps to  $511.17 \text{ cm}^2/\text{V.s}$  at 3%, and further increase in tensile strain, it keeps increasing due to decrease in effective mass discussed earlier. At 6% strain, the hole mobility becomes  $2629.88 \text{ cm}^2/\text{V.s}$ . Hole mobility along zigzag direction when transverse direction is relaxed varies from  $1164.42 \text{ cm}^2/\text{V.s}$  at  $-6\%$  strain to  $9.29 \text{ cm}^2/\text{V.s}$  at 2% strain. Beyond this mobility increases from  $60.05 \text{ cm}^2/\text{V.s}$  at 3% to  $373.22 \text{ cm}^2/\text{V.s}$  at 6% strain.

Some mention of the experimentally reported mobility values are in order here. Li et. al. [107] reported a hole mobility of  $984 \text{ cm}^2/\text{V.s}$  for a 10 nm thick sample. Liu et al [108] reported mobility of  $\sim 286 \text{ cm}^2/\text{V.s}$ . This was again, for few-layer samples. It should be noted that these for thicker samples, and are field-effect mobilities that are affected by the physics of phosphorene-metal lead contacts. Also, the mobilities may not be in the directions of easy flow. These could, in fact, be an average over a number of crystallographic directions.

### **3.3 Data of deformation potential, effective mass and mobility**

Table 3.1: Deformation potential while transeverse direction is fixed

electron	$\Gamma$ -X	1.83
electron	$\Gamma$ -Y	5.87
hole	$\Gamma$ -X	3.27
hole	$\Gamma$ -Y	0.34

Table 3.2: Deformation potential while transeverse direction is relaxed

electron	$\Gamma$ -X	0.80
electron	$\Gamma$ -Y	4.92
hole	$\Gamma$ -X	3.24
hole	$\Gamma$ -Y	1.44

Table 3.3: Effective mass of hole ( $m_h$ ) when strain is along x direction and y direction is fixed

strain (%)	$\Gamma$ -X	$\Gamma$ -Y
-6	0.147	1.677
-5	0.149	1.779
-4	0.152	1.881
-3	0.154	1.996
-2	0.157	2.102
-1	0.159	2.226
0.5	0.160	2.274
0.0	0.160	2.338
0.5	0.161	2.395
1	0.162	2.454
2	0.164	3.220
3	0.165	3.355
4	0.167	3.514
5	0.168	3.683
6	0.169	3.818

Table 3.4: Effective mass of electron ( $m_e$ ) when strain is along x direction and y direction is fixed

strain (%)	$\Gamma$ -X	$\Gamma$ -Y
-6	0.169	1.075
-5	0.172	1.079
-4	0.174	1.082
-3	0.176	1.089
-2	0.177	1.094
-1	0.178	1.102
-0.5	0.178	1.107
0.0	0.178	1.110
0.5	0.179	1.114
1	0.179	1.117
2	0.179	1.127
3	0.179	1.135
4	0.179	1.146
5	0.179	1.156
6	0.179	1.168

Table 3.5: Effective mass of hole ( $m_h$ ) when strain is along y direction and x direction is fixed

strain (%)	$\Gamma$ -X	$\Gamma$ -Y
-6	0.121	1.677
-5	0.127	1.704
-4	0.133	1.646
-3	0.140	1.752
-2	0.146	1.925
-1	0.153	2.256
-0.5	0.157	2.130
0.0	0.160	2.338
0.5	0.164	2.682
1	0.168	4.229
2	0.176	22.226
3	0.184	7.480
4	0.193	4.448
5	0.202	3.137
6	0.211	2.399

Table 3.6: Effective mass of electron ( $m_e$ ) when strain is along y direction and x direction is fixed

strain (%)	$\Gamma$ -X	$\Gamma$ -Y
-6	0.134	1.073
-5	0.140	1.077
-4	0.147	1.084
-3	0.155	1.087
-2	0.162	1.094
-1	0.170	1.102
-0.5	0.174	1.106
0.0	0.178	1.110
0.5	0.182	1.113
1	0.188	1.116
2	0.199	1.125
3	0.229	1.134
4	2.186	0.132
5	1.618	0.134
6	1.443	0.137

Table 3.7: Effective mass of hole ( $m_h$ ) when strain is along x direction and y direction is relaxed

strain (%)	$\Gamma$ -X	$\Gamma$ -Y
-6	0.158	3.072
-5	0.157	2.523
-4	0.157	2.156
-3	0.159	2.276
-2	0.159	2.518
-1	0.159	2.226
-0.5	0.159	2.274
0.0	0.160	2.338
0.5	0.161	2.395
1	0.160	2.573
2	0.162	2.703
3	0.161	2.513
4	0.162	2.637
5	0.164	2.771
6	0.163	3.040

Table 3.8: Effective mass of electron ( $m_e$ ) when strain is along x direction and y direction is relaxed

strain(%)	$\Gamma$ -X	$\Gamma$ -Y
-6	0.183	1.078
-5	0.182	1.084
-4	0.180	1.086
-3	0.182	1.092
-2	0.180	1.097
-1	0.178	1.102
-0.5	0.178	1.107
0.0	0.178	1.110
0.5	0.179	1.114
1	0.176	1.114
2	0.176	1.122
3	0.174	1.130
4	0.174	1.138
5	0.174	1.149
6	0.172	1.156

Table 3.9: Effective mass of hole ( $m_h$ ) when strain is along y direction and x direction is relaxed

strain (%)	$\Gamma$ -X	$\Gamma$ -Y
-6	0.130	1.889
-5	0.134	1.878
-4	0.139	1.877
-3	0.143	1.932
-2	0.149	2.068
-1	0.154	2.348
-0.5	0.157	2.181
0.0	0.160	2.338
0.5	0.164	2.649
1	0.167	4.128
2	0.174	28.415
3	0.182	8.075
4	0.190	4.571
5	0.199	3.094
6	0.209	2.282

Table 3.10: Effective mass of electron ( $m_e$ ) along y direction and x direction is relaxed

strain (%)	$\Gamma$ -X	$\Gamma$ -Y
-6	0.139	1.086
-5	0.144	1.091
-4	0.150	1.096
-3	0.156	1.099
-2	0.163	1.104
-1	0.170	1.107
-0.5	0.174	1.109
0.0	0.178	1.110
0.5	0.183	1.111
1	0.188	1.111
2	0.196	1.114
3	0.218	1.115
4	0.869	0.243
5	1.571	0.140
6	1.301	0.144

Table 3.11: Mobility of electron ( $\mu_e$ ) in the unit  $\text{cm}^2/\text{V.s}$  when transverse direction is fixed

strain (%)	$\Gamma$ -X	$\Gamma$ -Y
-6	2641.90	180.19
-5	2581.10	174.98
-4	2531.19	169.46
-3	2483.91	164.41
-2	2442.20	159.31
-1	2416.12	153.85
-0.5	2408.42	150.98
0.5	2393.55	146.19
1	2389.98	143.41
2	2371.16	137.59
3	2358.63	126.91
4	2350.49	280.51
5	2342.59	316.89
6	2337.82	326.22

Table 3.12: Mobility of hole ( $\mu_h$ ) in the unit  $\text{cm}^2/\text{V.s}$  when transverse direction is fixed

strain (%)	$\Gamma$ -X	$\Gamma$ -Y
-6	815.21	28863.27
-5	770.90	27546.04
-4	729.94	28376.25
-3	692.00	25216.20
-2	657.87	21393.61
-1	627.77	16478.35
-0.5	616.44	17734.14
0.5	591.74	12290.34
1	580.93	6129.75
2	499.11	102.14
3	481.70	511.17
4	465.68	1089.49
5	449.14	1798.55
6	437.53	2629.88

Table 3.13: Mobility of electron ( $\mu_e$ ) in the unit  $\text{cm}^2/\text{V.s}$  when transverse direction is relaxed

strain (%)	$\Gamma$ -X	$\Gamma$ -Y
-6	10898.06	221.34
-5	10998.62	215.82
-4	11112.17	210.23
-3	10944.37	205.46
-2	11056.00	199.61
-1	11221.56	194.64
-0.5	11185.79	191.72
0.5	11116.73	186.46
1	11369.75	183.91
2	11279.59	179.51
3	11455.60	169.81
4	11421.99	204.74
5	11361.81	348.37
6	11584.70	365.27

Table 3.14: Mobility of hole ( $\mu_h$ ) in the unit  $\text{cm}^2/\text{V.s}$  when transverse direction is relaxed

-6	491.69	1164.42
-5	546.03	1155.31
-4	592.13	1136.56
-3	563.86	1070.95
-2	536.71	949.04
-1	573.59	770.54
-0.5	563.24	851.69
0.5	540.67	623.86
1	529.07	317.30
2	507.83	9.29
3	528.89	60.05
4	509.73	137.87
5	490.94	242.03
6	472.37	373.22



# Chapter 4

## Density functional study of metal/Black phosphorus interface

### 4.1 Motivation

The central aim of this chapter is to understand the atomistic details of the interfaces of phosphorene (monolayer black phosphorus) with various metal surfaces, and to identify metal surfaces that give rise to small Schottky barrier height (SBH) and/or small tunneling barrier height (TBH). A brief description of experimental results were given in Chapter 1. An aspect where theory complements experiments is the following. In experiments, metal electrodes were grown on phosphorene channels using electronbeam lithography. In this process, there is no control over how the metal grows on phosphorene, which facet of the metal grows at the metal phosphorene interface (MPI). In fact, the metal surface may not be faceted at all, or may contain more than one crystallographic planes. There can be strain or other defects at the interface degrading its charge injection capacity. Theory can give an insight into which surfaces of which metal give the best contact in terms of the lowest SBH or the lowest TBH. Pan et al.[137] have studied contact of phosphorene with the (110) surfaces of Al, Ag, Au and Cr, the (111) surfaces of Ni, Pd and Cu and the Ti(0001) surface. Chanana et al.[138] have explored contact between Au(111), Pd(111), Ti(0001) and phosphorene.

Zhu et al.[139] have studied interfaces of the (111) surfaces of Al, Ag, Au, Cu, and Zn(0001) with phosphorene. Phosphorene monolayer was found to metallize in contact with all the metal surfaces studied so far. Pan et al.[137] found n-type Schottky contact between phosphorene and the Al(110), Ag(110) and Ti(0001), while p-type Schottky contact between phosphorene and Cr(110), Au(110), Cu(111) and Ni(111). An Ohmic contact was found in case of Pd. Chanana et al. also found an Ohmic contact between phosphorene and Pd(111). A Schottky barrier was found between phosphorene and Au(111), while phosphorene-Ti(0001) contact was nearly Ohmic. Zhu et al.[139] found Schottky barrier at the contacts between phosphorene and Al(111), Au(111), Zn(001). Ohmic contacts were found between phosphorene and Cu(111) and Ag(111).

In spite of broad agreements, there are some differences between different calculations. For example, Pan et al. found the Cu(111)phosphorene interface to have p-type Schottky barrier while Zhu et al. found it to be Ohmic. Again Pan et al. reported Ti(0001)-phosphorene interface to be n-type Schottky barrier but Chanana et al. found this to be close to Ohmic. It should also be pointed out that different theoretical works analyze the MPIs in different ways. Pan et al. have reported the so-called lateral SBH and the TBH at the interfaces. Their characterization of the interfaces is based on the lateral SBH values. Chanana et al. rely on the TBH, and the electron charge distribution at the interface. While the other authors hold the lattice constant of the metal layer fixed and strain the phosphorene layer at the interface, Chanana et al. strain the metal layers holding the lattice constant of the phosphorene fixed. This causes large strain in some of the systems they studied. Chanana et al. also do not optimize all the atomic positions at the interface, they only optimize the metal-phosphorene separation. This way they miss out on possible large distortions of the phosphorene layer on Pd and Ti as reported by Pan et al. Zhu et al. characterize the interfaces based on the TBH, the electron charge distribution, electron localization function and the SBH. The definition of TBH used by different authors is also different as discussed in more detail later.

Given this state of affairs, we think the question of MPI requires further examination. In this work, we have considered interfaces between phosphorene and the Pd(100), Pd(110), Pd(111),

Au(110), Ni(111), Ti(0001) metal surfaces. Choice of the metals is driven by the fact that these have been used as electrodes in experiments.

## 4.2 Metal adatom on phosphorene

Our main motivation for studying adsorption of metal atoms on phosphorene is to find out if dispersion forces are important in metal-phosphorene interactions. This is important because it has been shown that metal-graphene interactions are dominated by these forces, and a failure to correctly incorporate them leads to incorrect conclusions[140]. Our strategy is to calculate adsorption energies of metal adatoms on a phosphorene monolayer using different exchange-correlation functionals. If the metal-phosphorene bondings are dispersion dominated physisorption, then the adsorption energies would be small. A guide is the adsorption energies of metal atoms on graphene. These are typically a fraction of an eV in LDA, and methods that incorporate dispersion interactions. GGAs usually produce significantly smaller adsorption energies, and sometimes they fail to produce any metal-graphite binding. On the other hand, if there is indeed covalent metal-P bonding, the adsorption energies are expected to be much larger, and GGAs should produce adsorption energies in the same range as the other methods in this case.

The adsorption energy (AE) of a metal atom on a phosphorene monolayer is defined as

$$AE = E_c(M/ph) - E_c(ph) - E(M) \quad (4.1)$$

where  $E_c(M/ph)$  is the cohesive energy of the metal atom adsorbed phosphorene monolayer,  $E(M)$  is the ground state energy of an isolated atom, and  $E_c(ph)$  is the cohesive energy of the phosphorene monolayer. Our convention is that cohesive energies are positive for bound systems, and hence a larger AE would imply a stronger metal-phosphorene bonding.

For adsorption of metal adatoms, we consider three special symmetry sites on a phosphorene monolayer. These are (a) the top site, on top of a P atom on the upper sub-layer of P atoms, (b) the bridge site, above a P-P bond on the upper sub-layer, and (c) hollow site, directly above the

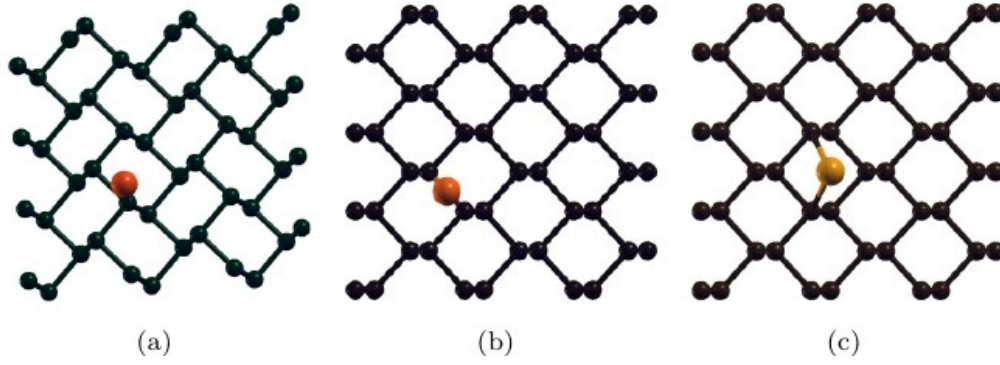


Figure 4.1: Metal atom on (a) top site, (b) bridge site and (c) hollow site of a phosphorene monolayer

Table 4.1: Strain in supercell of phosphorene along x direction ( $\epsilon_x$ ) and y direction ( $\epsilon_y$ ) when contact is made with metal surface

metal surface	size of metal slab	size of phosphorene	$\epsilon_x$	$\epsilon_y$
Pd(100)	$5 \times 6$	$3 \times 5$	0.76	0.76
Pd(110)	$5 \times 5$	$3 \times 6$	0.76	0.25
Pd(111)	$13.97 \times 9.68 \text{\AA}^2$	$3 \times 3$	0.76	2.3
Au(110)	$8 \times 4$	$5 \times 5$	2.1	1.0
Ti(0001)	$23.44 \times 10.15 \text{\AA}^2$	$5 \times 3$	1.5	2.5
Ni(110)	$4 \times 4$	$3 \times 3$	1.6	0.6

center of the rectangular unit cell of a phosphorene monolayer. These sites are indicated in fig 4.1. In all the four methods, the hollow site turns out to be the most favorable for all the metal atoms considered in this work, namely Pd, Ti, Au and Ni. This matches with the results of Kulish et al.[141] and Sui et al. [142]. However, Kulish et al. only used GGA, and did not explore whether dispersion interactions are important at metal-phosphorene interfaces. We show in Table 4.2 AE of these adatoms at the hollow site for all the four methods we used. From the AE data, it is seen that LDA gives the highest binding between metal and phosphorene. This is not surprising since LDA generally leads to over-binding. The AE obtained using PBE and DFT-D2 are nearly the same. Those using vdW-DF2 are slightly smaller, but are of the of same order. What is important is that AEs are few eV. In light of these results, we conclude that there is a significant covalent bonding between metal atoms and phosphorene, and therefore, PBE-GGA is an appropriate method to study MPI.

Table 4.2: Adsorption energy of metal atom on phopshorene surface using different method

Exchange-correlation	Pd	Ti	Au	Ni
LDA	4.68	4.98	2.76	5.52
PBE-GGA	3.50	4.44	1.61	4.32
DFT-D2 Grimme	3.83	4.61	1.97	4.56
vdW-DF2	2.65	2.64	1.14	3.13
favorable site	top site	valley site	top site	valley site

There is one important point where our results differ from those of Kulish et al. [141] and Sui et al.[142] Both these works found the AE of a Ni atom to be larger than that of a Ti atom. The Ti atom was found to have a moment of  $2 \mu_B$  after adsorption. We found that this is not the lowest energy state. The non magnetic state of a Ti atom on phosphorene is  $\sim 0.5$  eV lower which makes Ti to have the largest AE among the metal atoms studied in our work.

### 4.3 Atomic and electronic structure of MPI

In this section, we present results for atomic and electronic structure of a phosphorene monolayer on all the metal surfaces we have considered. Results in this section and the subsequent ones have

been obtained using PBE-GGA. First, we calculate the AEs of the phosphorene monolayer on various metal surfaces. AE of a phosphorene monolayer on a metal surface is defined as

$$AE = E_c(ph/M) - E_c(ph) - E_c(M) \quad (4.2)$$

$E_c(ph/M)$ ,  $E_c(M)$  and  $E_c(ph)$  are the cohesive energies of the combined metal slab-phosphorene system, bare metal slab and phosphorene monolayer, respectively. The AEs turn out to be 0.41, 0.38, 0.45, 0.64, 0.11 and 0.51 eV per P atom on the Pd(111), Pd(110), Pd(100), Ti(0001), Au(110) and Ni(110) surfaces, respectively. The MPIs studied here can be divided into two broad classes: phosphorene binds strongly with Pd, Ni and Ti surfaces, but it binds rather weakly with the Au surface. The AE of a phosphorene monolayer is the largest on Ti(0001) among the surfaces studied here. This is consistent with the fact that a Ti adatom has the largest AE on phosphorene. In fact, the ordering of AEs for different MPIs follows the same trend for AEs of metal adatoms on a phosphorene monolayer. The AE of a Ti adatom is followed by those of Ni, Pd and Au in this order. The AEs of a phosphorene monolayer on different metal surfaces are also ordered as Ti(0001), Ni(110), the three Pd surfaces, and Au(110). Since the strain in the phosphorene monolayer is small in every case, it is the strength of the metal-P bonding that largely determines the metal-phosphorene bonding. Largest AE on the Ti(0001) surface also leads to the largest deformation of the phosphorene monolayer on this surface as the P atoms try to optimize the local P-Ti bonding. This leads to good mix of phosphorene and Ti states which has important consequences for the tunneling barrier at this interface. Side views of all MPIs are given in Fig. 4.2 Large distortion of phosphorene on Ti(0001) is quite obvious. On the other hand, phosphorene has the weakest binding with Au(110), and also the metal-P distance is the largest in this case. The AE of a phosphorene monolayer, and the shortest metal-phosphorene distance in each case are given in Table 4.3.

Proximity of the metal substrate drives all metal-phosphorene systems metallic. This is in agreement with all the published results on these systems. This is clearly seen in the electronic densities of states (DOS) for these systems which are presented in fig. 4.3. It is worth noting

Table 4.3: Adsorption energy of per P atom (eV) of monolayer phosphorene on metal surfaces and the nearest metal phosphorus distance( $\text{\AA}$ )

Metal surface	AE	distance
Pd(111)	0.41	2.27
Pd(110)	0.38	2.24
Pd(100)	0.45	2.22
Au(110)	0.11	2.40
Ti(0001)	0.64	2.34
Ni(110)	0.51	2.08

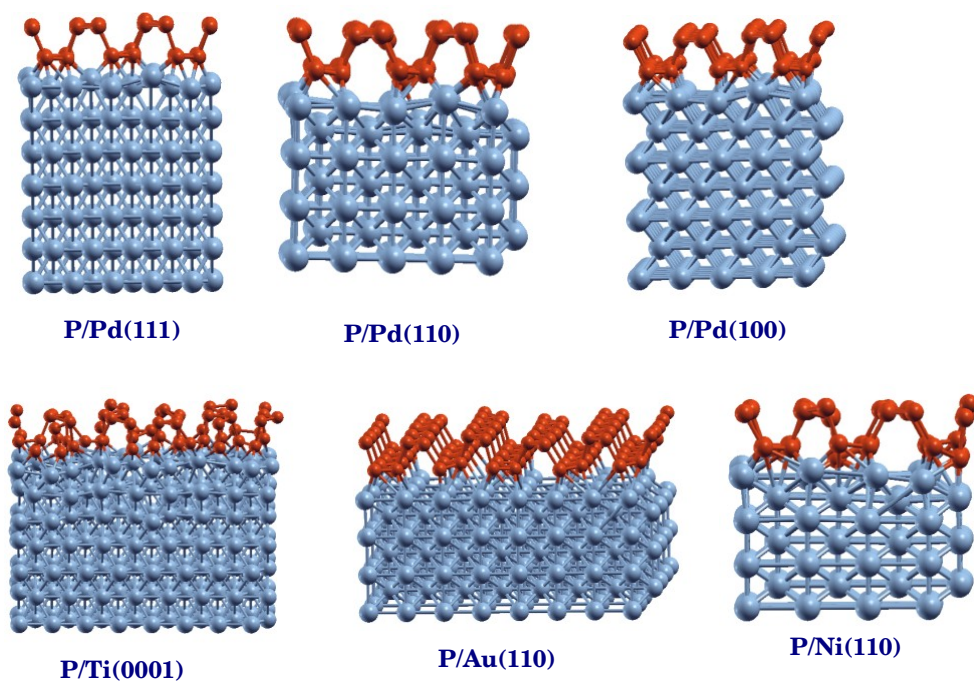


Figure 4.2: Side views of atomic structure of a phosphorene monolayer on various metal surfaces

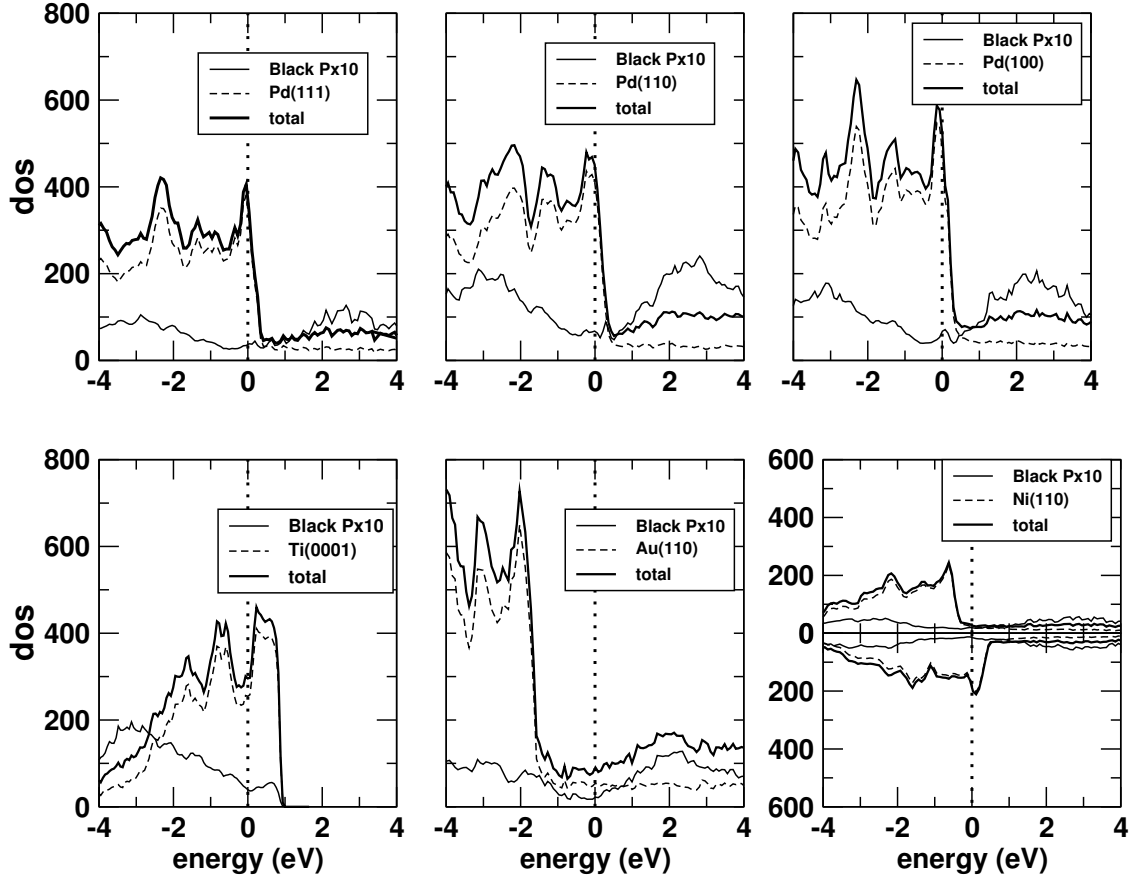


Figure 4.3: DOS for metalphosphorene systems. Total and atom projected DOSs are shown. Energies are plotted relative to the Fermi energy

that the Fermi energy lies at a peak in the DOS in all metal-P systems except for P/Au(110). In the other metal-phosphorene systems, the corresponding states have major contributions from the metal d states (3d for Ti and Ni and 4d for Pd). This leads to large DOS near the Fermi energy in these systems. Of the metal substrates we have considered, Ni is the only one that is magnetic. Ni remains magnetic even after adsorption of a phosphorene monolayer. The magnetic moment per atom changes marginally from  $0.68 \mu_B$  per atom in a Ni slab to  $0.56 \mu_B$  per atom after adsorption of phosphorene monolayer. As seen in fig 4.3, the magnetic moment is mostly contributed by the Ni atoms. There is very little moment on the P atoms.

## 4.4 SBHs at the interfaces

The barrier for charge injection at a metal-semiconductor interface is a fundamental issue that affects the performance of any semiconductor device. This issue has also challenged our understanding of such interfaces for the past few decades. Before first-principles calculations became a vogue, a number of phenomenological models were proposed, the aim of all these being to understand and estimate the barrier associated with charge injection across such interfaces. The simplest of these models is the so-called Schottky-Mott model. The basic assumptions of this model are (i) the metal-semiconductor contact is intimate, (ii) yet, there is no charge transfer across the metal-semiconductor interface, therefore, no dipole forms at the interface, (iii) there are no chemical reactions, or any physical strain in either of the two systems. The underlying principle of this model is the superposition principle of electrostatic potentials: if the vacuum level energies outside the metal and the semiconductor are aligned, the relative positions of the metal Fermi level ( $E_F$ ), and the conduction band minimum (CBM) and the valence band maximum (VBM) of the semiconductor give the relevant barrier heights. There were no effects of the proximity of the metal and semiconductor materials on the positions of the  $E_F$ , CBM and VBM relative to the vacuum level. Within this model, the barrier for an n-type semiconductor is the difference between the work function of the metal and the electron affinity (EA) of the semiconductor

$$\Phi_n = \phi_M - \chi_{SC} \quad (4.3)$$

Here,  $\Phi_n$  is the barrier height,  $\phi_M$  is the work function of the metal and  $\chi_{SC}$  is the EA of the semiconductor. EA is taken as the difference between the vacuum energy and the CBM. The barrier height at the interface of a metal and a p-type semiconductor is similarly given by

$$\Phi_p = I_{SC} - \phi_M \quad (4.4)$$

where  $\Phi_p$  is the barrier height and  $I_{SC}$  is the IP of the semiconductor. IP is the difference between the vacuum energy and the VBM.

The assumptions of the Schottky-Mott model are rather drastic. In particular, it is natural that some charge transfer takes place at the interface which creates an interface dipole. This gives an additional contribution to the barrier height. Formation of such dipoles has also been considered in more refined models for SBH: the finite separation model and the ideas of Fermi level pinning and metal-induced gap states, for example. Tung has discussed these ideas in considerable detail in a recent review[34].

With our ability to calculate properties of metal semiconductor interfaces from first-principles, these phenomenological models lose their primacy as the correct model should, in principle, emerge from the atomistic details provided by these calculations. Therefore, in addition to estimating the SBH within the Schottky-Mott model, we also calculate the TBH, the true microscopic potential barrier height experienced by an electron at the metalsemiconductor interface.

First, we discuss SBH as estimated by the Schottky-Mott model. For an interface between a bulk metal and a bulk semiconductor, one calculates the SBH by calculating the difference between the metal work function and the IP or EA of the semiconductor as discussed above. However, as we have already shown, a phosphorene monolayer gets metallized in contact with all the metal substrates considered here. Therefore, the Schottky barrier would appear during lateral charge injection from the metallic metal-phosphorene system to the phosphorene channel. The lateral SBH is the relevant energy barrier in such a scenario. We calculate this quantity by comparing the work function of the metal-phosphorene systems and the IP and EA of a monolayer phosphorene. The work functions of different metal-phosphorene systems are calculated as the difference between the vacuum level energy and the Fermi energy of the corresponding system. We have calculated the vacuum energy as follows. The effective local potential  $V_{eff}(r)$  experienced by an electron at any point  $r = (x, y, z)$  is obtained as a sum of three contributions: Hartree potential  $V_H$ , exchange-correlation potential  $V_{xc}$  and the external potential  $V_{ext}$  (due to the ion cores). The average of  $V_{eff}(r)$  over constant  $z$  planes is plotted as a function of  $z$ , the direction perpendicular to the

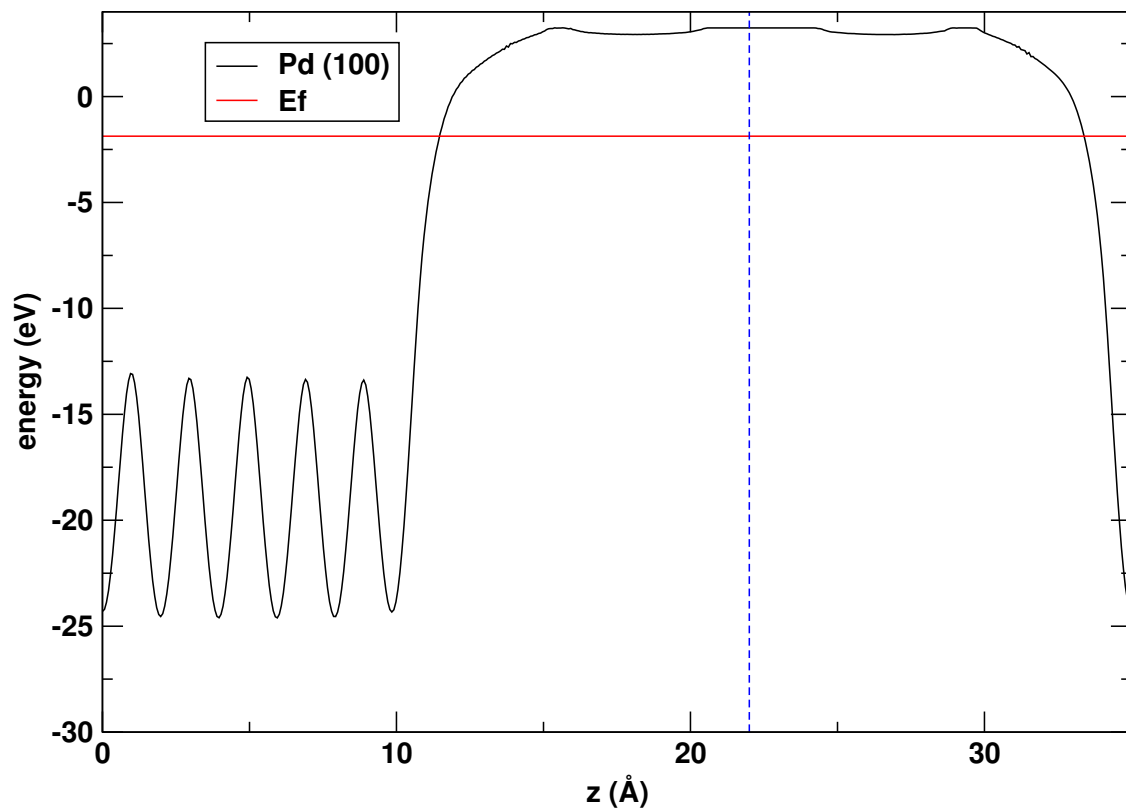


Figure 4.4: Variation of  $V_{eff}(z)$  within the Pd slab, and in the vacuum region. Value of  $V_{eff}(z)$  in the middle of the vacuum region, marked by the dotted vertical line, is the vacuum level energy. Difference between the vacuum level energy and  $E_f$  is the work function.

Table 4.4: electron schottky barrier height ( $e_{SBH}$  in eV) and hole schottky barrier height ( $h_{SBH}$  in eV) at metal/phosphorene interface

Metal surface/P	$e_{SBH}$	$h_{SBH}$
Pd(111)/P	0.93	Ohmic
Pd(110)/P	0.70	0.20
Pd(100)/P	0.97	Ohmic
Ti(0001)/P	0.41	0.49
Au(110)/P	0.89	0.01
Ni(110)/P	0.18	0.72

MPI. The value of this potential in the middle of the vacuum region, after the initial oscillations have died down, is taken as the the vacuum level energy. The case for the phosphorene-Pd(100) surface is shown in Fig. 4.4 to illustrate the point. The same procedure is followed in case of other phosphorene-metal systems to find their work functions.

Work functions of monolayer phosphorene adsorbed Pd(100), Pd(111), Pd(110), Au(110), Ti(0001) and Ni(110) are found to be 5.10, 5.06, 4.83, 5.02, 4.54 and 4.31 eV, respectively. This ordering of the work functions of phosphorene adsorbed metal surfaces is slightly different from that of the pure metal surfaces. Work functions of the metal surfaces considered here are in decreasing order, 5.24 eV for Pd(111), 5.11 eV for Pd(100), 4.84 eV for Pd(110), 4.75 eV for Au(110), 4.55 eV for Ni(110) and 4.38 eV for Ti(0001). The EA and IP of phosphorene are found to be 4.13 and 5.03 eV, respectively. The schematic energy diagrams for the locations of the composite metal-phosphorene Fermi energies, and the VBM and CBM of monolayer phosphorene are shown in Fig. 4.5 after their vacuum levels are aligned. We now look at the details of these energy level diagrams and find the SBH within the Schotky-Mott model. In case of Pd(111) and Pd(100), the Fermi energy of the phosphorene-metal composite is below the VBM of monolayer phosphorene as seen in Fig. 4.5. According to Eq. (4.4), the hole barrier height would be negative, implying that there are no barriers for hole injection from the metal to the semiconductor. On the other hand, there are finite barriers for electron injection according to Eq. (4.3). These barriers are found to be 0.93 and 0.97 eV, respectively, for Pd(111) and Pd(100). Fermi levels of phosphorene-adsorbed Pd(110), Ti(0001), Au(110) and Ni(110) are in the bandgap of phosphorene. Hence, there are fi-

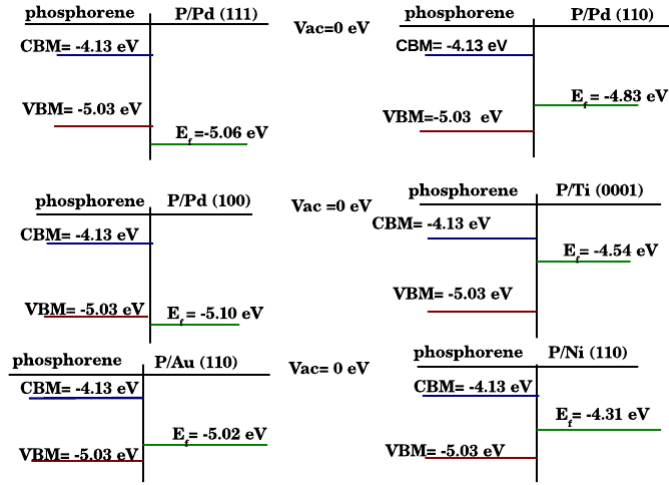


Figure 4.5: Location of the Fermi level in phosphorene-metal systems, and phosphorene VBM and CBM after aligning the vacuum levels. Electron and hole SBH can be inferred from these figures

nite barriers for both electron and hole injection. Using Eq. (4.3), the electron barrier heights turn out to be 0.97, 0.41, 0.89 and 0.18 eV for Pd(110), Ti(0001), Au(110) and Ni(110), respectively. From Eq. (8), the barrier heights for hole are found to be 0.2, 0.49, 0.01 and 0.72 eV for Pd(110), Ti(0001), Au(110) and Ni(110), respectively.

The values are listed in Table 4.4 for ready reference. The simplistic Schottky-Mott model thus predicts that there are significant barriers to charge injection from metal to phosphorene in many cases. Particularly, large barriers are predicted for electron injection from all the three surfaces of Pd, and Au(110). Electron barrier height for Ni(110) is relative small. Hole barrier height is large for Ti(0001) and Ni(110) and small for Pd(110) and Au(110). There are no barriers for holes for Pd(111) and Pd(100) as already noted.

## 4.5 TBHs at the interfaces

We now turn to the calculation of the TBH experienced by the electrons while getting injected from the metal to phosphorene. TBH is inferred from the variation of the planar-averaged electrostatic potential ( $v_e(z)$ ), which is the sum of  $V_H$  and  $V_{ext}$ , of an electron in a direction normal to the interface. Different authors have used  $v_e(z)$  to define the TBH at metal-semiconductor interfaces differently. Popov et al.[143] studied TBH at metal-MoS2 interfaces. The maximum value of  $v_e(z)$  between the metal and the semiconductor relative to its value at the top metal layer was taken as the height of the tunneling barrier. The full width at half maximum (FWHM) of the profile of  $v_e(z)$  was interpreted as the width of the barrier. Zhong et al. and Pan et al.,[144] on the other hand, define the maximum of  $v_e(z)$  relative to the  $E_F$  in the metal slab as the TBH, while the FWHM above  $E_F$  is defined as the width. Since the problem of charge injection from the metal to the semiconductor is one of an electron moving in one dimension (perpendicular to the interface) and experiencing a space-varying potential, whether it passes through unhindered, or has to tunnel through a barrier, depends on the height of the electrostatic potential barrier relative to the energy of the electron. Only if the kinetic energy of the electron is less than the height of the potential, it has to tunnel through, otherwise there are no barriers to its motion. Therefore, we believe that the idea in Refs. [18] and [36] is more appropriate, and use it for calculation of TBH at the MPIs.

Figure 4.6 presents variation of  $v_e(z)$  calculated for all the MPIs. We find that among all the metal surfaces we have studied,  $v_e$  is higher than the Fermi energy at the MPI only in case of Au(110). Thus, there is a finite tunneling barrier only in P/Au(110) interface. The TBH at the P/Au(110) interface is found to be 1.46 eV, and the barrier width, measured by its FWHM, is 0.66 Å. In all other cases, electrons get injected into the phosphorene layer without any barrier. This scenario is consistent with the fact that a phosphorene monolayer has the weakest binding to the Au(110) surface, and the metal-P distance is also the largest in this case as shown in Table 4.3. It has been shown [143] that barrier for charge injection at a metal-semiconductor interface depends on the degree of mixing between the metal and semiconductor states. We have already argued that mixing between phosphorene and Ti(0001) is the largest as this system has the largest AE.

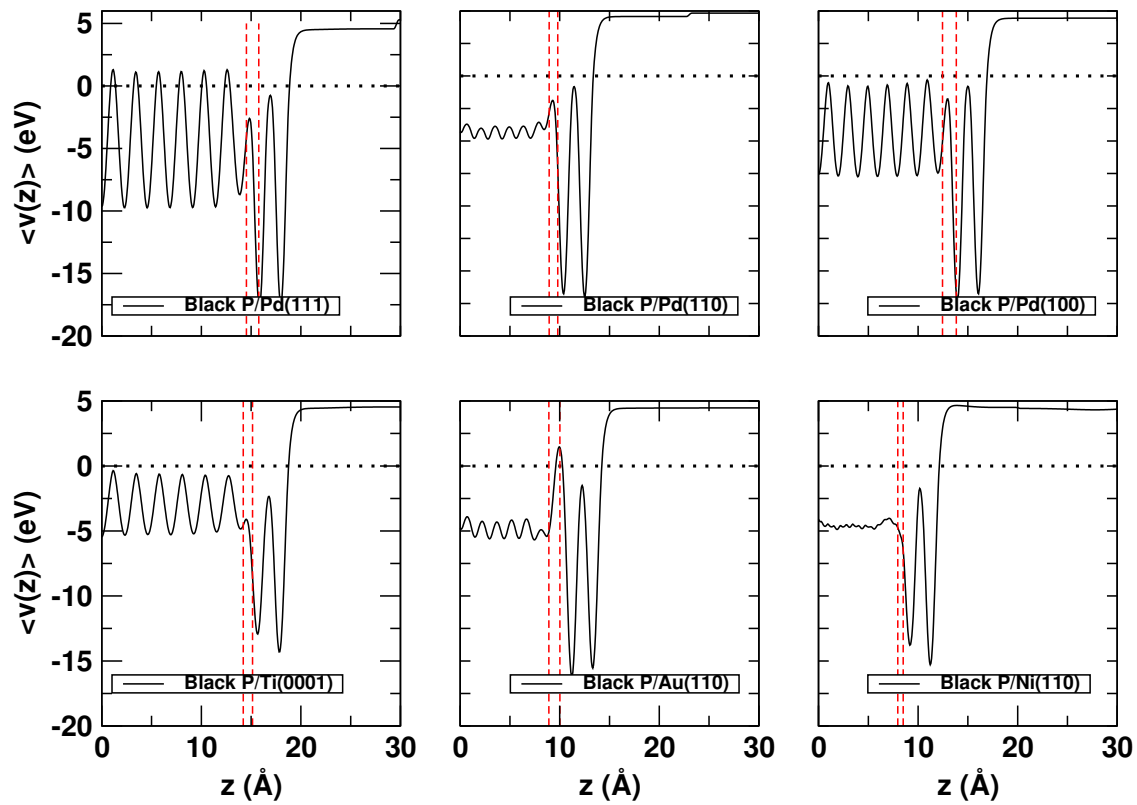


Figure 4.6: Location of the Fermi energy (dotted lines), and variation of the electrostatic potential for metalphosphorene systems

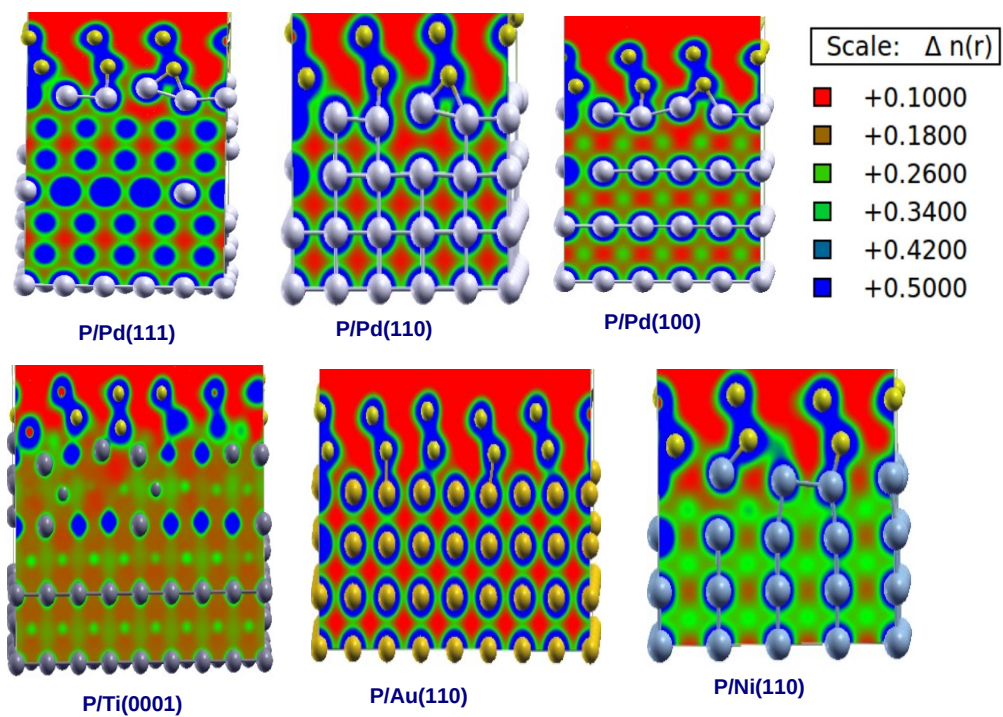


Figure 4.7: Charge density in a plane perpendicular to the MPI. Top two layers are phosphorus atoms, the lower ones are the metal atoms

On the other hand, it would be the smallest at the P/Au(110) interface. This is borne out by the electron charge density contours at the interfaces. Electron charge density in a plane perpendicular to the interface is shown for each metal-phosphorene system in Fig. 4.7. It is clear that there is a larger charge density at P/Ti(0001) and P/Ni(110) interfaces compared to the others. The charge density at the P/Au(110) interface is the lowest. The P/Pd interfaces fall in-between. Consistent with this picture,  $v_e(z)$  is the lowest in case of P/Ti and P/Ni interfaces, and is the highest at the P/Au interface. Its value at the P/Pd interfaces are intermediate to these, as seen in Fig. 4.5.

## 4.6 Discussions

We now briefly discuss our results in the context of the experimental and theoretical results reported in the literature. FET with Pd electrodes was found to behave as a p-type one by Du et al.[104]. Das et al. also found that hole injection from Pd to phosphorene was an efficient process. P/Ni interface was found to have a larger resistance compared to P/Pd interface. In agreement with these works, we found that hole injection at the P/Pd(111) and P/Pd(100) is barrier-less. The SBH for holes at the P/Pd(110) is also small, 0.2 eV. However, our calculated electron SBHs for Pd surfaces are larger than that for Ni(110). Hole SBH at the Au(110) interface turns out to be the lowest. However, this is in complete contrast to the picture obtained from the electronic structure and TBH calculations. One also has to keep in mind that the SBH values have been calculated using the simplistic Schottky-Mott model. Das et al., in another work, estimated the electron and hole SBH between bilayer phosphorene and Ni electrodes. Their estimates for electron and hole SBH are 0.49 and 0.18 eV, respectively. As already stated, we report the lateral SBH values for monolayer phosphorene-metal contacts. In experiments, few-layers phosphorene samples are used and those may not be completely metallized unlike a monolayer. Therefore, in such cases, the vertical SBH would be the relevant quantity. We cannot, therefore, directly compare our calculated lateral SBH values for monolayer phosphorene with these estimates. However, it is heartening to note that they are of the same order (Table 4.4). Ti was found to be an efficient electron injector by Das et

al.[105]. Perello et al.[106] also found FETs with thin phosphorene layers to be n-type, indicating easier electron injection. Indeed, our calculations show that the electron SBH at the P/Ti(0001) interface is marginally smaller than the hole SBH. The TBH also vanishes at this interface. Our results are thus in broad agreement with the experimental findings. Comparing with the theoretical works mentioned in Sec. 1, our results for SBH are in excellent qualitative agreement with those of Ref. 132, where they overlap with some small quantitative differences in case of the Pd(111) and Au(110) surfaces. Our TBH results also agree quite well. Finite TBH is found at the interface with Au(110), while that at the Pd(111) and Ti(0001) vanishes. Our results differ from those of Chanana et al.[138] in some cases perhaps because the metal substrate is strained and the lateral positions of the phosphorus atoms are not relaxed in their calculations. They found phosphorene-Pd(111) contact to be Ohmic. We find it Ohmic for holes, but not for electrons. They found phosphorene-Ti(0001) contact to be close to Ohmic, while we find reasonable SBH for both electrons and holes.

# Chapter 5

## Phosphorene Nanoribbon

One of the initial motivations for studying PNRs was to have an additional control over the band gap through manipulating the width of the PNRs. In any case, channel materials are finite in the direction perpendicular to the current, which gives a motivation for studying PNRs. It may be noted that it is possible to form PNRs with three different types of edges: zigzag (z-PNR), rugged (or armchair) (a-PNR), and linear (l-PNR) edges.

Although the excitement generated by phosphorene is due to its promising role as a channel material in FETs, we are aware of only two other theoretical works on transport ( $I$  -  $V$ ) characteristics of PNRs so far. Zhang et al. [145] have studied transport properties of zPNR devices of width 5 unit cells and lengths ranging from 3 to 6 units cells. More importantly, they calculated transport characteristics of layer-terminated (as obtained by truncating the monolayer), z-PNR devices without considering reconstruction. As we show later, edges of z-PNRs undergo structural reconstruction.

### 5.1 Computational details

The geometry and electronic structure calculations for phosphorene sheet and PNRs are performed within a plane wave density functional theory (DFT) formalism. An energy cutoff of 500 eV is used for the plane wave basis set. Interactions between the valence electrons and the ion cores

are represented by projector augmented wave (PAW) potentials. The PBE gradient corrected functional is used for the exchange-correlation energy. In a few cases we have also employed the hybrid HSE06 functional proposed by Hyde, Scuseria, and Ernzerhof to have a more accurate estimate of the band gap. An  $(8 \times 8 \times 1)$  Monkhorst-Pack (MP) k-point mesh is used for Brillouin zone (BZ) integration for electronic structure calculations of the monolayer. For the nanoribbons running along the x and y directions (defined below)  $(8 \times 1 \times 1)$  and  $(1 \times 8 \times 1)$  MP k-point meshes were employed. We kept a vacuum space of 15 Å in all the nonperiodic directions in the supercell. All the atoms in the supercells were relaxed using a conjugate gradient method till all the force components became less than 0.01 eV/Å. The VASP code was used for these calculations.

Atomic structure of phosphorene layer is shown in fig. 5.1. The direction along the trenches is designated as y in this work, while the perpendicular direction in the plane of the monolayer is designated as x. The direction perpendicular to the monolayer plane is designated as z. The optimum lattice constants of a monolayer along the x and y directions are found to be 4.62 and 3.3 Å (using GGA-PBE exchange-correlation functional), respectively, in good agreement with other DFT calculations[133]. One may have two different types of edges for PNRs that are periodic along y: edges with P atoms that are either onefold or twofold coordinated. We termed these as the l-PNR and z-PNR, respectively as shown in fig.5.5 (a) and (c) respectively. In case of PNRs periodic along x, only one type of edge is possible in which, of the four atoms at one edge of the unit cell, two are twofold coordinated and the other two are threefold coordinated. These have been called the rugged edges or armchair edges, and these PNRs the a-PNR as shown in fig. 5.2.

## 5.2 Electronic structure of phosphorene and PNRs

A phosphorene monolayer is found to have a direct gap of 0.9 eV in PBE. The CBM occurs exactly at the point in the Brillouin zone. The VBM occurs marginally away from the point towards Y . Therefore, a monolayer phosphorene can be considered practically to have a direct gap. This finding is in agreement with what has been reported by Sa et al.[146] and Tran et al.[72]. Using

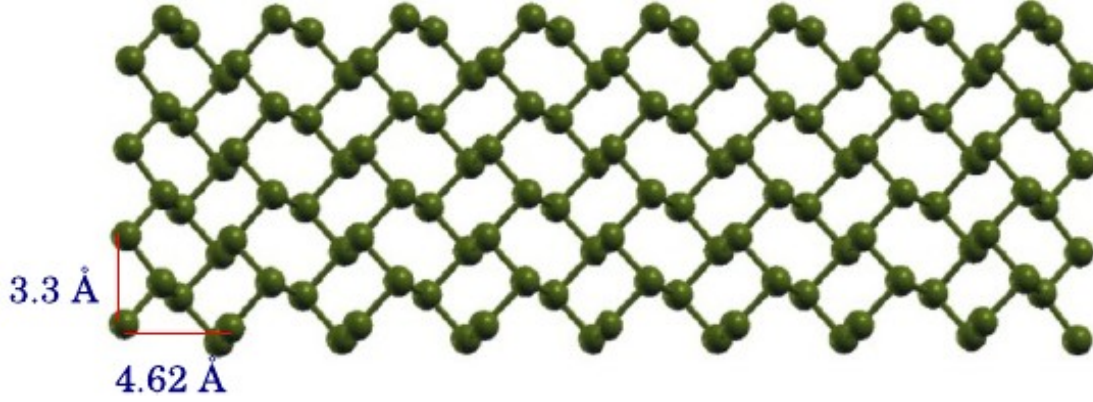


Figure 5.1: Structure of monolayer phosphorene.

HSE06 also, the VBM was found slightly away from the point, while the CBM was still at the point. The gap turned out to be 1.6 eV. These results are in very good agreement with the results published earlier. As we stated before, one can form three different types of PNRs. Energetic stability of PNRs are determined by their formation energies. Formation energy (FE) of a PNR is defined as

$$FE = E_T - n\mu_P \quad (5.1)$$

where  $E_T$  is the total energy of the PNR composed of  $n$  phosphorus atoms, and  $\mu_P$  is the chemical potential of a P atom in its reference state. In these calculations we have taken a phosphorene monolayer as the reference state. The larger the FE, the more energetically unfavorable is a structure. In their layer-terminated structures, the formation energies of the l-PNRs turn out to be 1.2 eV per edge atom, while that of z-PNRs is 0.67 eV per edge atom. The formation energy of the a-PNRs is much smaller, 0.31 eV per edge atom. These numbers are consistent with the fact that l-PNRs have the largest number of dangling bonds per edge atom, two. z-PNRs, on the other hand, have one dangling bond per edge atom, and hence have a smaller formation energy. a-PNRs have, on average, 1/2 dangling bond per edge atom. Consequently, it has the smallest FE. The l-PNRs have the highest formation energies, and their edges are highly unstable undergoing large reconstructions.

**a – PNR:** Having optimized the lattice constants, we studied electronic properties of a-PNRs of width 2 – 10 unit cells. The structure of a-PNR of width 4 is shown in fig 5.2. The electronic

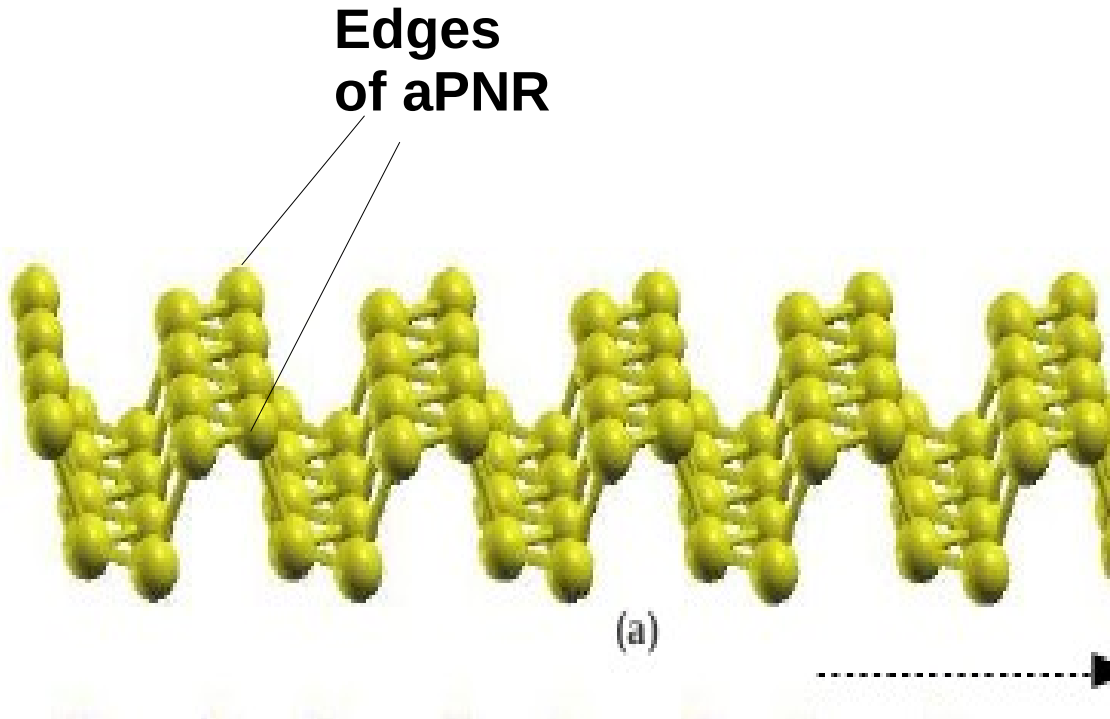


Figure 5.2: (a) Structure of a a-PNR of width 4. The arrow is the direction of periodicity.

structure of width 1 2 and 3 unit cell are shown in fig 5.3. All these turn out to be indirect band gap semiconductors (in PBE) except 1 unit cell wide nanoribbon (fig 5.2 (a)). For a-PNRs of widths 4 – 6, the VBM appears at the point and the CBM appears between  $\Gamma$  and the zone boundary. The band gap of a-PNRs of width 2 and 3 are 1.20 and 1.03 eV, respectively, larger than the gap of a monolayer. The band gap decreases monotonically with increasing width. At width 4, it falls below the gap of a monolayer, and is 0.70 eV. Calculated band gaps of all the a-PNRs are

Table 5.1: Lattice constants and calculated band gaps of a-PNRs of various widths

width	lattice constant ( $\text{\AA}$ )	band gap (eV)
2	5.07	1.20
3	4.75	1.03
4	4.69	0.70
5	4.67	0.53
6	4.66	0.48
8	4.65	0.42
10	4.64	0.42

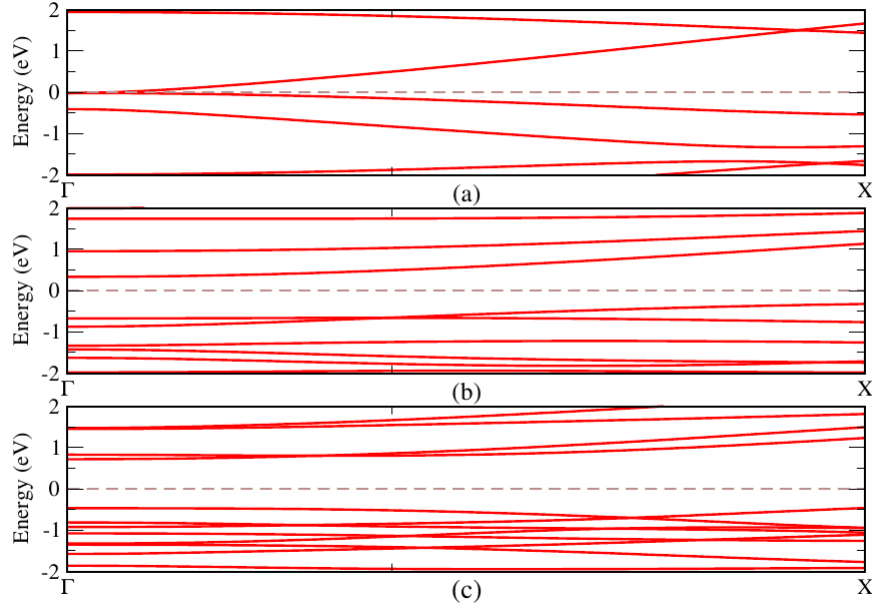


Figure 5.3: band structure of (a) 1 unit cell wide, (b) 2 unit cell wide and (c) 3 unit cell wide a-PNR

Table 5.2: Energy gain (meV/edge dimer) and gap value (eV) for edge reconstructed z-PNRs of different widths.

width	Energy gain	band gap
4	9.8	0.11
5	8.4	0.14
6	11.0	0.12
7	13.0	0.14
8	10.0	0.11

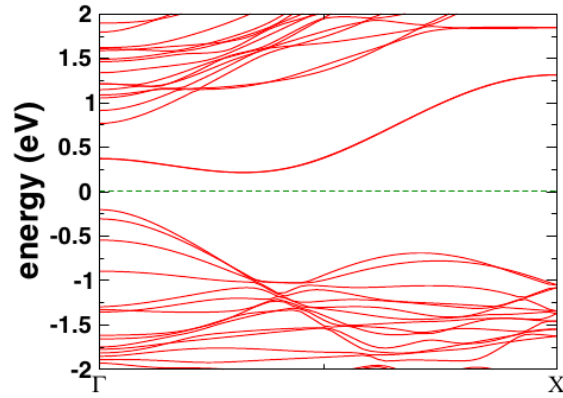


Figure 5.4: band structure of 8 unit cell wide a-PNR

given in Table 5.1. Guo et al.[147] have studied these nanoribbons of width 7 – 12 unit cells and have found them to be indirect gap semiconductors. Carvalho et al.[148] have also reported similar calculations. We calculated a ribbon of width 10, and this also turned out to be a semiconductor having an indirect gap of 0.42 eV in agreement with the results in. One may conclude that the bandgap of a-PNRs is not very sensitive to the width beyond 6 unit cells, and an indirect to direct gap transition occurs somewhere between a ribbon of width 12 unit cells and the monolayer. Band structure of an a-PNR of width 8 is shown in Fig. 5.4.

**z – PNR:** In contrast to the a-PNRs, the z-PNRs have metallic band structure at all widths between 1 – 8 in their layer-terminated structures. The structure of z-PNR is shown in fig 5.5 (c). In all of these, two bands cross the Fermi energy. The band structure turns out to be different in z-PNRs of width 1 – 3 and shown in figure 5.6 (a), (b) and (c) respectively.

The k-points at which these bands cross the Fermi energy depends on the width of the PNR. However, none of these crossings happens at simple fractions such a  $1/2$  or  $1/4$  from  $\Gamma$  to the zone boundary. For example, one of the bands in the z-PNR of width 1 crosses the Fermi energy at  $9/10$  to the zone boundary. In z-PNRs of width larger than 3 unit cells, both these bands are exactly half-filled. This is understandable because there is only one dangling bond per edge atom in the z-PNRs. The band structure turns out to be different for widths 1 – 3. The k points at which these bands cross the Fermi energy depend on the width of the PNR. However, none of these crossings

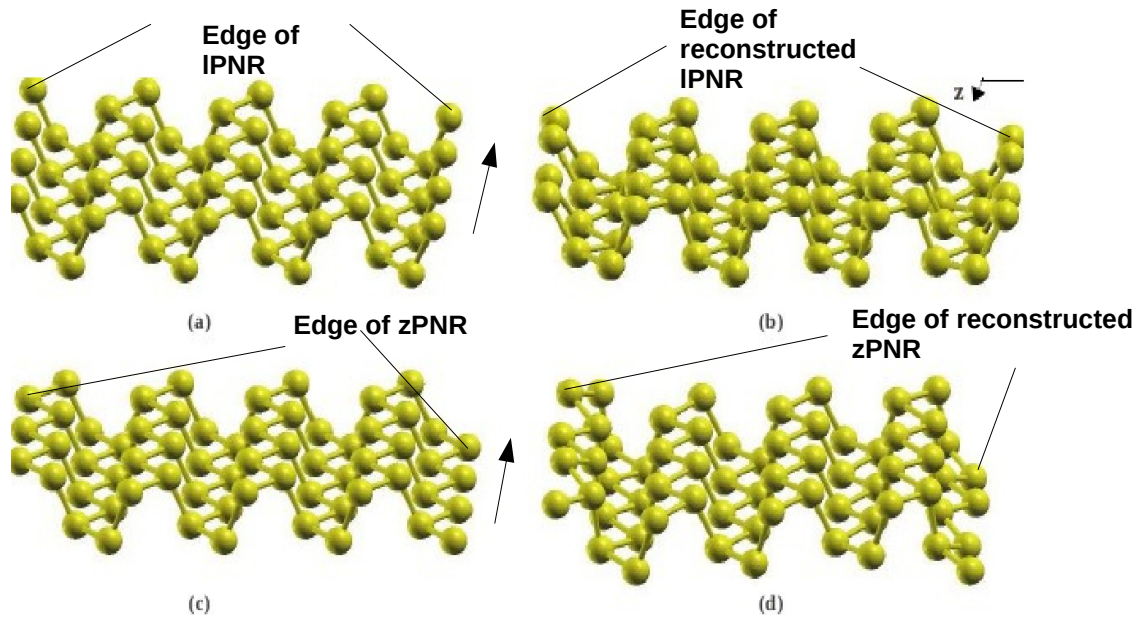


Figure 5.5: Structure of (a) layer-terminated l-PNR, (b) edge reconstructed l-PNR, (c) layer-terminated z-PNR, (d) Peierls distorted z-PNR. Arrow shows the direction of periodicity.

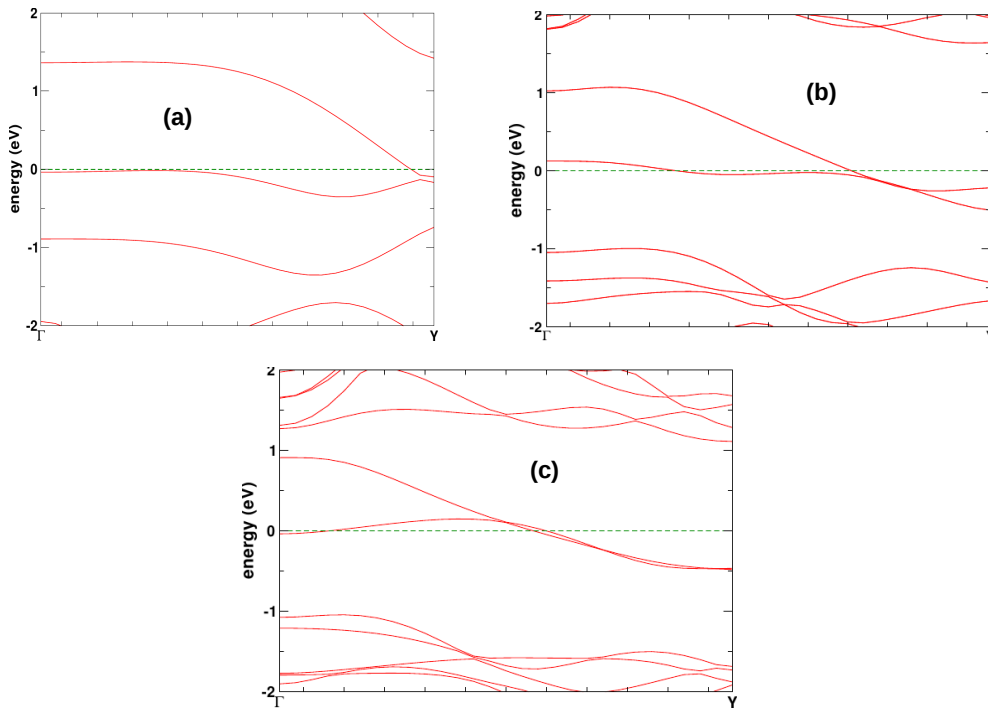


Figure 5.6: band structure of (a) one unit cell (b) two unit cell and (c) three unit cell wide z-PNR

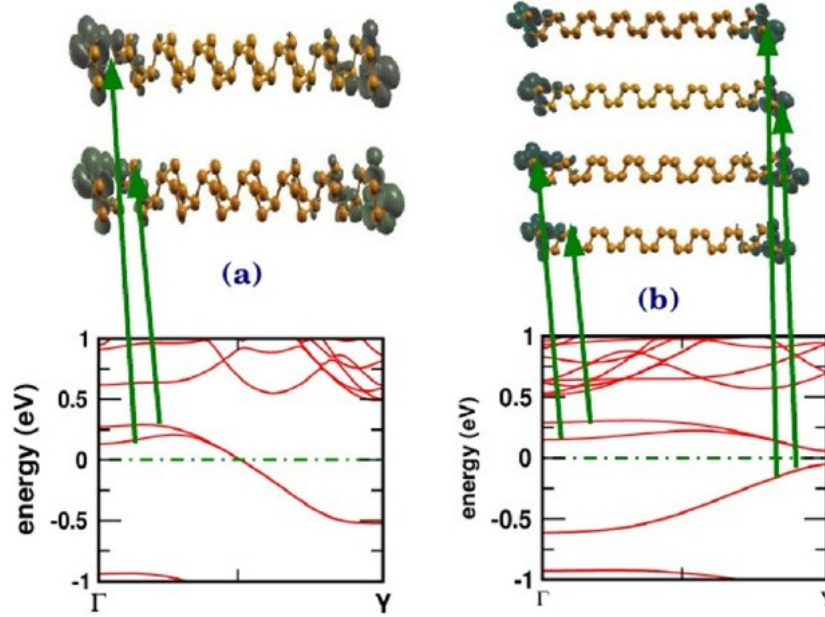


Figure 5.7: Isosurfaces of charge density from (a) the half-filled bands in the layer-terminated and (b) VBM and CBM of edge reconstructed z-PNR. These figures show that the charge density is localized at the edges.

happens at simple fractions such a  $1/2$  or  $1/4$  from to the zone boundary. We focus on z-PNRs of width 4 and more as these are likely to be practically important. Isosurface of charge density and band structure of a layer-terminated z-PNR of width 4 is shown in fig 5.7(a). The bands crossing the Fermi energy are formed of the  $p_x$  and  $p_z$  orbitals of the edge atoms, and interestingly, both the bands have contributions from P atoms at both edges. Therefore the metallic nature is due to the one-dimensional (1D) chain of P atoms at the two edges.

The half-filled bands due to the 1D chain of edge atoms present an unstable situation. It is well known that such 1D metallic systems undergo structural distortion through dimerization of successive atom pairs. The consequent doubling of the unit cell halves the BZ, leading to the opening of a small gap at the new zone boundary. This phenomenon, proposed by Peierls, is known as Peierls transition. To find out if the edges of z-PNRs indeed undergo such a Peierls transition, we performed calculations with a supercell consisting of two primitive unit cells along the length of the z-PNR. After relaxation, two successive atoms along the edges were indeed found to dimerize. In particular, the distance between successive atoms in the periodic direction along

the first few rows of atoms (first, second, and third for width 8) starting from the edges decreases marginally to  $3.27\text{\AA}$  from  $3.3\text{\AA}$  in the layer-terminated structure. For other atomic rows in the interior of the PNR, the atoms have a separation of  $3.3\text{\AA}$ , as in a monolayer. Structure of such a layer terminated and edge reconstructed z-PNR is shown in fig. 5.5 (c) and (d). This small distortion decreases the total energy of a z-PNR, and also opens a gap. The exact value of energy gain and gap depends on the width for the PNR. These values for z-PNRs of width from 4 up to 8 unit cells are given in Table 5.2. The energy gain and gap values are nearly the same for all widths in this range. Band structure of a z-PNR of width 8 after gap opening is shown in fig. 5.7 (b). If this phenomenon of gap opening is indeed a Peierls transition, one expects the atomic character of the VBM and the CBM after gap opening to be the same as the character of the edge bands crossing the Fermi energy in the layer-terminated metallic nanoribbons. Indeed, the VBM at the zone boundary is formed of the  $p_x$  and  $p_z$  orbitals of the edge atoms in the edge reconstructed PNR. The CBM has contributions from some of the interior atoms in addition to dominant contribution from the edge atoms. The charge density originating from the half-filled bands before reconstruction, and the VBM and CBM after reconstruction are shown in fig. 5.7 (a) and (b). It is obvious that these bands are localized along the two edges.

**1 – PNR:** We calculated band structure of l-PNRs of widths ranging from 1 – 6, and 8 unit cells taking the same unit cell in the periodic direction as in a monolayer. The structure of l-PNR is shown in fig 5.5(a). We call these the layer-terminated PNRs in contrast to structurally distorted PNRs that have different unit cells in the periodic direction. An l-PNR of width 1 (shown in fig 5.8 (a)) turns out to be a semiconductor with an indirect gap of 1.38 eV. The CBM is at the  $\Gamma$ -point and the VBM is between  $\Gamma$  and the zone boundary. l-PNR of width 2 in its layer-terminated structure presents an interesting case where two bands cross each other at the Fermi energy. The band structure plot is shown in fig 5.8 (b). Ribbons of widths 3 – 6 turn out to be metallic with four bands crossing the Fermi energy in each case. Two of these bands are  $\sim 1/4$  filled and two others are  $\sim 3/4$  filled. Band structure for a l-PNR of width 4 is shown in Fig.5.9. The topmost valence band and the lowest conduction band in the monolayer have mainly  $p_z$ , and

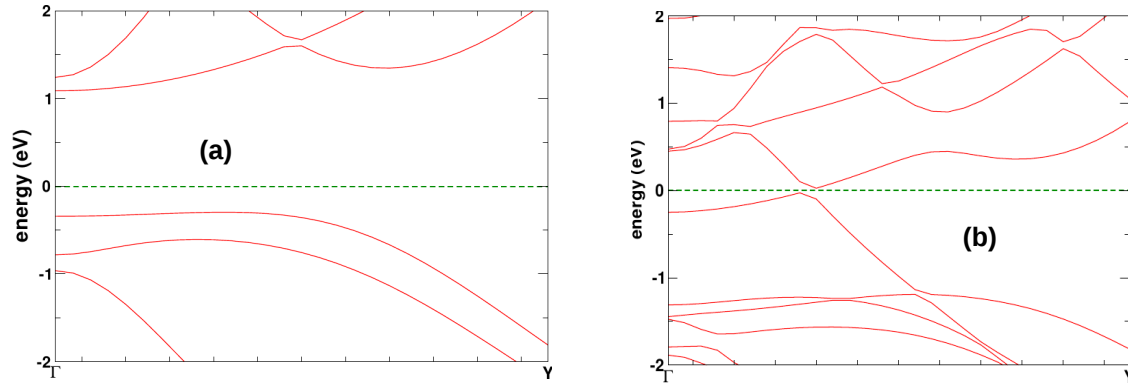


Figure 5.8: band structure of (a) one unit cell (b) two unit cell wide 1-PNR

$p_z + p_x$  characters respectively. The bands crossing the Fermi energy have major contributions from the  $p_x$  and  $p_z$  orbitals of the edge atoms only. So clearly, these are edge states with different bonding characteristics than states in the monolayer. These originate from  $\sigma$  overlap of the  $p_y$  orbitals, and  $\pi$  overlap of the  $p_x$  orbitals on the neighboring atoms and form metallic channels running along the edges. A charge density isosurface plot (fig 5.9 (a)) for one of these bands clearly show that it is localized at the edges in the transverse direction but is delocalized along both the edge channels. Other bands crossing the Fermi energy give similar pictures. This metallic band structure is similar to those obtained in many bulk terminated semiconductor surfaces. Such metallic surface states result within the bulk band gap due to weak overlap between orbitals of nearest neighbor surface atoms that are actually next nearest neighbors in the bulk. This is exactly what happens in the 1-PNRs. Successive edge atoms in the periodic direction are in fact next nearest neighbors in the monolayer having a separation of 3.3 compared to the nearest neighbor distance of  $\sim 2.2\text{\AA}$ . It is well known that many semiconductor surfaces, for example, C(100), Si(100), Ge(100), undergo reconstructions through dehybridization of the  $sp^3$  hybrid orbitals on the surface atoms and formation of new bonds. The end result is the formation of surface dimers that leads to doubling or quadrupling of the surface unit cell. The natural question to ask is whether such an edge reconstruction is possible in the 1-PNRs. To test this, we studied 1-PNRs of widths 1 – 6 and 8 taking supercells having two primitive cells along the periodic  $y$  direction. After atomic relaxation, the two neighboring atoms on each edge move towards each other and form an edge

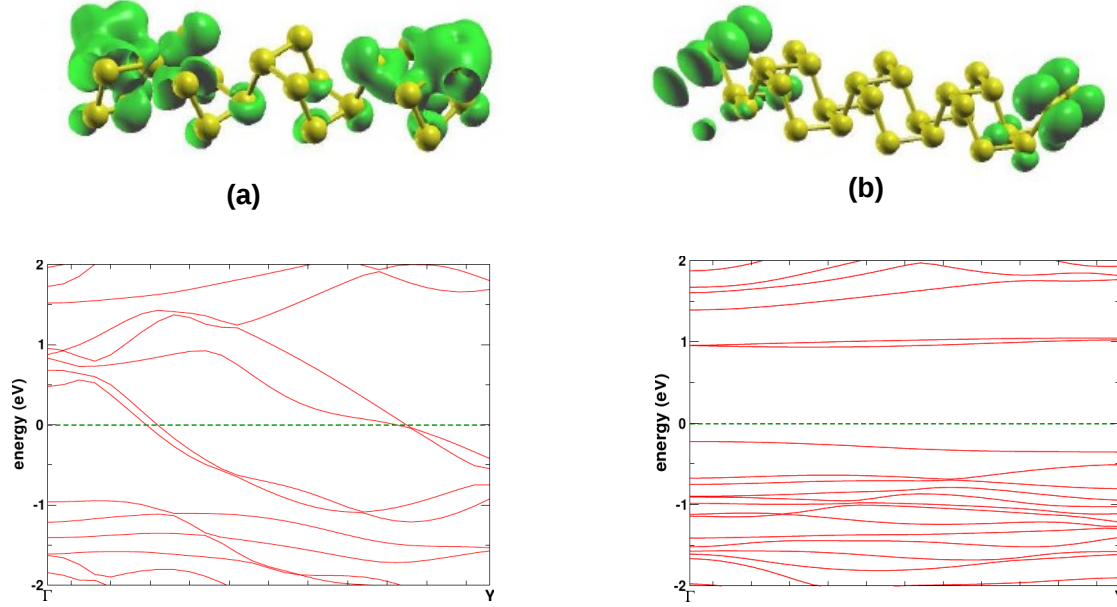


Figure 5.9: Isosurfaces of charge density from (a) the partially filled band in the layer-terminated and (b) VBM and CBM of edge reconstructed IPNR. These figures show that the charge density is localized at the edges.

dimer. The structure of layer terminated and edge reconstructed l-PNR are shown in fig 5.5 (a) and (b) respectively. The dimer bond length is only  $\sim 2\text{\AA}$ , even smaller than the nearest neighbor bond length in the monolayer. This is a consequence of the fact that each edge P atom makes only one bond in the layer-terminated structure which gives it a large degree of structural flexibility. Hence, there is a significant reconstruction at the edges with a consequent doubling of the unit cell along the periodic direction. This indeed opens a gap in the band structure and leads to a reduction in total energy. The gap in a 4 unit cell wide l-PNR is 1.11 eV (direct gap) and the reduction in total energy is 1.44 eV per edge dimer. The energy gain due to edge reconstruction is substantial when compared to the energy gain in the well studied  $(2 \times 1)$  reconstruction of the Si(100) surface ( $\sim 2$  eV per surface dimer). The band structure of an edge reconstructed l-PNR of width 3 is shown in fig.5.8 (b). This is the result of a dehybridization process on the edge atoms. The edge bands crossing the Fermi energy are formed of the  $p_x$  and  $p_z$  orbitals as already stated. But after reconstruction, two degenerate CBMs are formed by the  $p_x$  and  $p_z$  orbitals of the edge atoms. These bands have very little dispersion because these are localized on the dimers and have very little amplitude in between two successive edge dimers. This can be understood

from the fact that the smallest separation between two successive edge dimers is  $4.6\text{\AA}$ . We have illustrated the difference between the metallic edge bands and the CBM after edge reconstruction in the isosurface plots of fig. 5.9(a) and (b). The l-PNR of width 2, which showed a crossing of bands, also undergoes the same edge reconstruction that opens an indirect gap of 1.31 eV as found in PBE.

### 5.3 Conclusion

In summary, our first-principles electronic structure calculations based on DFT show that all PNRs except for z-PNRs of 1-3 and l-PNR having width 2, are semiconducting. It is possible that these PNRs also become semiconducting with complicated structural deformations. However, it is difficult to guess the exact nature of such structural deformations. Experimental investigations can reveal the nature of atomic and electronic structure of these nanoribbons. As we have clearly demonstrated, l-PNRs undergo edge reconstruction and z-PNRs undergo Peierls distortion to open gaps in their band structures. These phenomena make PNRs an interesting class of materials from a fundamental point of view. This information will also be useful for any electronic applications of this material. We hope that these results will motivate experimental search for these effects in PNRs.

Here I will mention some properties of PNRs. Zhang et al.[145] studied the electronic properties of PNRs having different widths and edge configurations and reported that PNRs with armchair edges are semiconductors, while the zigzag PNRs are metallic. For armchair PNRs, it was shown that the bandgap decreases as the width of the NR increases. After H-passivation of the edges, zigzag PNRs become semiconducting, while the bandgap of the armchair PNR gets larger than for bulk phosphorene. In addition, it was demonstrated that all the semiconducting NRs exhibit very large values of Seebeck coefficient (SC) and are tunable upon hydrogen passivation of the edges. Ding et al. [149] also investigated the effect of edge passivation on the electronic structure of BPNRs. The edges of PNRs are highly active and can be bonded easily with oxygen atoms

and hydroxyl groups demonstrating that PNRs can be easily oxidized. In addition, it was shown that a transition from semimetallic character to semiconducting can be achieved in both zigzag and armchair PNRs upon oxidation.

In another study, Sorkin and Zhang<sup>[144]</sup> investigated the mechanical properties PNRs under uniaxial tensile strain and reported that the deformation and failure of PNRs are highly anisotropic. It was reported that PNRs have a high failure strain ( $\epsilon = 0.5$ ) along the armchair direction with a low failure stress ( $\sigma = 50$  GPa), while along the zigzag direction the failure occurs at early stages of tensile strain ( $\epsilon = 0.1$ ) but with a relatively high failure stress ( $\sigma = 100$  GPa). For both directions, the value of the failure stress is sensitive to the width of the PNRs, while the failure strain is unaffected.



# Chapter 6

## Density functional study of metal/blue phosphorene interface

By theoretical means we are able to understand the charge density, voltage drop, barrier height at the metal/blue phosphorene interface which help to choose the suitable metal surface to make contact. So far no experimental or theoretical studies have been done about blueP/metal interfaces. Motivated by the results of monolayer black phosphorus/metal interface calculation we have calculated the tunnel barrier height (TBH) and Schottky barrier height (SBH) between low index metal surface and blue phosphorene. We choose Pd(111), Pd(110), Pd(100), Al(111), Au(110) and Ni(100) to perform the barrier height calculation.

### 6.1 Computational method

The results of interfacial properties are obtained from first principle calculations using plane wave based density functional theory (DFT) code Vienna ab-initio simulation package (VASP). The implementation of DFT involves the solution of the Kohn-Sham equations, which are one-electron Schrodinger equations in the presence of an effective one-electron self-consistent potential. The single particle Kohn-Sham orbitals are represented in plane wave basis. The kinetic energy cutoff for the plane wave basis was taken to be 500 eV. Interaction between valence electrons and ions

are implemented using projector augmented wave method (PAW).

The adsorption energy of metal atom on blue phosphorene slab was calculated by using local density approximation (LDA) and generalized gradient approximation (GGA-PBE). To understand the van-der Waals interaction between metal atom and blue phosphorene, dispersion corrected Grimme method (DFT-D2) and non local correlation method (vdW-DF2) has been used. The description of LDA, GGA-PBE, dispersion corrected Grimme method (DFT-D2) and non local correlation method (vdW-DF2) was discussed in method section.

The primitive cell of blue phosphorene is hexagonal. To calculate the adsorption energy of metal atom on blue phosphorene slab a rectangular supercell of size  $11.36 \times 9.28 \text{ \AA}^2$  was taken. The atoms are relaxed until the forces on atoms are less than  $0.01 \text{ eV/\AA}$ . Brillouin zone integration is performed with Monkhorst-pack k-mesh of size  $6 \times 8$ . A vacuum of  $23 \text{ \AA}$  is used to avoid any interaction between periodic images. The metals chosen to know the binding with blue phosphorene are Al, Au, Pd, Ni.

For monolayer blue phosphorene interface calculation we choose rectangular supercells of metals and blue phosphorene. To match the lateral sizes of metal and blue phosphorene, blue phosphorene is strained in both x and y direction keeping in mind that the strain should be less than 3% in individual direction. For rectangular or square surface primitive cells like Au(110), Pd(110), Pd(100) and Ni(100), a supercell of size  $n_1 \times m_1$  is taken. The rectangular supercell for blue phosphorene for the corresponding metals were given in Table 6.1. In the composite system of metal and blue phosphorene the bottom three atomic layers of metal were kept fixed and top three atomic layer of metal and blue phosphorene atoms were relaxed. The force convergence criteria to relax the atoms in composite system was taken as  $0.01 \text{ eV/\AA}$ .

Table 6.1: Strain in supercell of phosphorene along x direction ( $\epsilon_x$ ) and y direction ( $\epsilon_y$ ) when contact is made with metal surface

metal surface	$\epsilon_x$	$\epsilon_y$
Pd(111)	1.7	1.7
Pd(110)	1.7	0.3
Pd(100)	1.7	2.2
Au(110)	2.7	2.1
Al(111)	0.6	0.6
Ni(100)	1.4	1.2

## 6.2 Results

### 6.2.1 Pristine blue phosphorene

Having a hexagonal primitive cell, blue phosphorene shows  $D_{3d}^3$  space group symmetry[148]. The interaction between layers is very weak and of value 6 meV/atom. The interlayer distance is 5.63 Å. The AB hexagonal stackings and ABC rhombohedral stacking differ energetically by less than 1 meV/atom[115]. The consecutive atoms in blue phosphorene are in different sublayers and the bond length is 2.26 Å. The optimized lattice constant using PBE exchange-correlation functional is 3.28 Å. The lattice structure and PBE band structure of monolayer blue phosphorus is shown figure 6.1. The conduction band minimum is in between  $\Gamma$  and M point. The valence band maximum occur in between K and  $\Gamma$  point. Therefore blue phosphorene is an indirect semiconductor with band gap  $\sim 2$  eV. The lattice constant and band gap are in good agreement with literature[110].

### 6.2.2 Metal adatom on blue phosphorene

Interlayer interaction in bulk blue phosphorus is due to weak van-der Waals force. Therefore the absence of out of plane dangling bonds in monolayer blue phosphorus motivates us to find if the interaction between one metal atom and blue phosphorene is dispersion dominated or not. In metal-graphene system it has been seen that without incorporation of dispersion force, the binding energy between metal and graphene gives inaccurate result. Therefore we perform a systematic study of

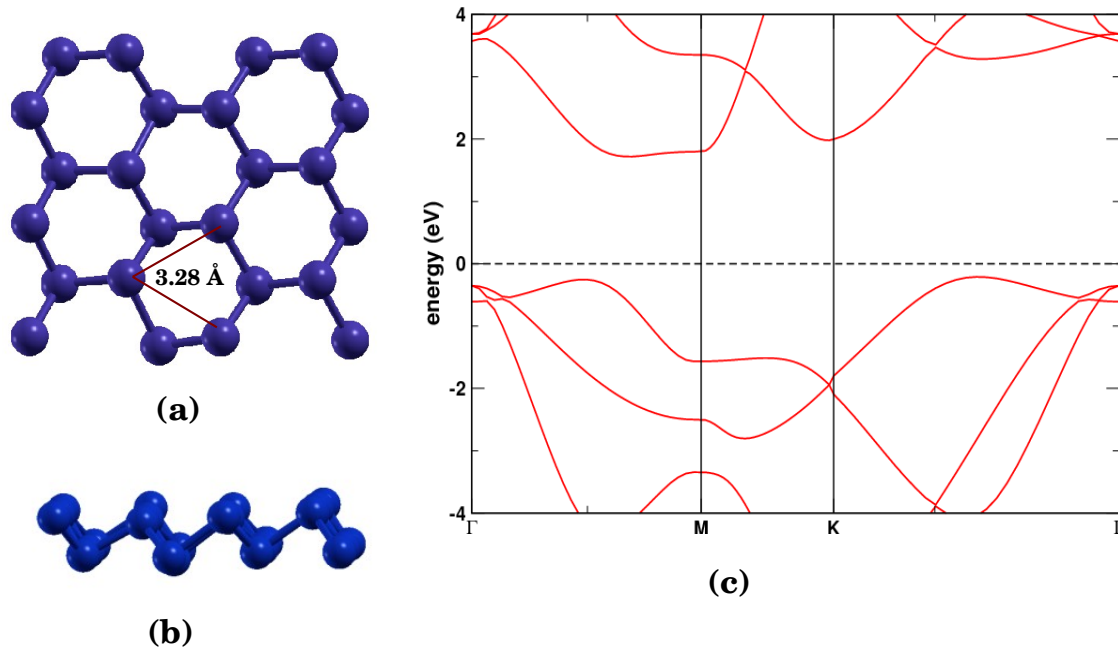


Figure 6.1: Monolayer blue phosphorus (a) top view, (b) side view, (c) band structure with PBE

adsorption energy of metal atom with blue phosphorene using LDA (local density approximation), GGA -PBE, DFT-D2 and vdW-DF2 method.

The adsorption energy (AE) of metal adatom on the monolayer blue phosphorus is defined as

$$AE = E_c(M) - E_c(\text{BlueP}) - E_c(M/\text{BlueP}) \quad (6.1)$$

$E_c(M/\text{BlueP})$  is the cohesive energy of composite system consisting of single metal atom and blue phosphorene.  $E_c(M)$  is the ground state energy of metal atom and  $E_c(\text{BlueP})$  is the cohesive energy of the blue phosphorene slab. Adsorption energy positive infers metal atom binds with blue phosphorene slab. The higher adsorption energy implies strong binding of metal atom and blue phosphorene. The adsorption energy of different metals using various methods are summarized in table 6.2.

Four high symmetry sites are used to calculate the adsorption energy of metal adatom on blue phosphorene as shown in figure 6.2. The sites are (a) bridge site: top of the P-P bond of upper sublayer of the blue phosphorene, (b) hollow site: above the center of hexagonal cell when there is no phosphorus atom at the bottom of metal atom, (c) top site: top of the upper layer phosphorus

atom of the blue phosphorene slab, (d) valley site: at the center of hexagonal cell where there is a phosphorus atom at the bottom of metal atom. The hollow site is the favorable site for Au and Pd atom. For Ni and Al atom the valley site is favorable. The LDA results give largest adsorption energy between metal adatom with blue P slab. This happens because LDA leads to overbinding. The Grimme DFT-D2 method shows slightly higher adsorption energy than PBE-GGA. The vdW-DF2 method shows fraction of eV lower adsorption energy than PBE-GGA. This implies that the adsorption energy between metal atom and blue P layer is captured by using only PBE-GGA method. Therefore for metal slab/blue P interface calculation the PBE-GGA method is sufficient.

Table 6.2: Adsorption energy of metal atom on blue P surface using different method

Exchange-correlation	Au	Al	Pd	Ni
LDA	2.52	2.25	4.11	5.28
PBE-GGA	1.53	1.76	3.00	3.94
DFT-D2 Grimme	1.86	1.92	3.31	4.20
vdW-DF2	1.14	1.36	2.23	2.88
favorable site	top site	valley site	top site	valley site

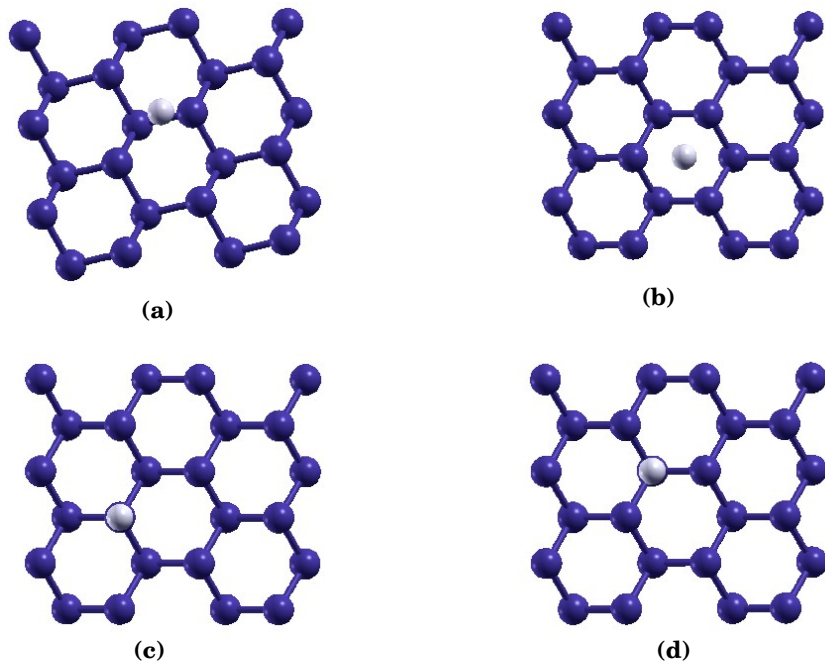


Figure 6.2: The adsorption sites for metal atom on (a) bridge site, (b) hollow site, (c) top site, (d) valley site

The magnetic moment of all atoms are found zero after adsorption. Here we will be only focussing

on studying the binding of metal adatom on blue phosphorene and we will limit ourselves to use only PBE-GGA method.

### 6.2.3 Atomic and electronic structure of metal/blue phosphorene interface

Now we will discuss the atomic and electronic structure of the metal/blue phosphorene (M/Blue P) system which is shown in figure 6.3 and 6.4. The results of this section and subsequent sections are based on PBE-GGA exchange-correlation functional. We have already discussed about the calculation details of M/blue P composite structure in computational method. The adsorption energy (AE) of blue phosphorene on metal is defined as

$$AE = E_c(M) - E_c(\text{BlueP}) - E_c(M/\text{BlueP}) \quad (6.2)$$

$E_c(M/\text{BlueP})$ ,  $E_c(M)$ ,  $E_c(\text{BlueP})$  are cohesive energies of metal slab and blue phosphorene composite system, bare metal slab and monolayer blue P respectively. The adsorption energy and the minimum distance between atoms of metal surface and blue phosphorene are listed in table 6.3. The adsorption energy are 0.42, 0.36, 0.44, 0.18, 0.59, 0.075 eV/P atom on Pd(111), Pd(110), Pd(100), Au(110), Ni(100) and Al(111) surface respectively. Ni(100) surface shows largest binding with blue P slab. This is consistent with the Ni adatom on blue P slab result which shows larger binding than Au, Al, Pd atom on blue P. Al atom on blue P slab shows slightly higher binding energy than Au atom. But Al(111) surface shows smaller binding with blue P than Au(110).

Due to the proximity of metal substrate the metal/blue phosphorene is becoming metallic. As seen from figure 6.4 a peak of density of states (DOS) lie at the Fermi energy for different Pd surfaces and Blue P/Ni(100) surface. The major contributions are coming from 3d states of Ni and 4d states of Pd. The magnetic moment per atom changes marginally from 0.66  $\mu_B$  per atom in a Ni slab to 0.57  $\mu_B$  per atom after adsorption of phosphorene monolayer. As seen in fig 4, the magnetic moment is mostly contributed by the Ni atoms. There is very little moment on the P atoms.

Table 6.3: Adsorption energy of per P atom (eV) of blue P on metal surfaces and the nearest metal phosphorus distance( $\text{\AA}$ )

Metal surface	AE	distance
Pd(111)	0.42	2.25
Pd(110)	0.36	2.22
Pd(100)	0.44	2.24
Au(110)	0.18	2.39
Al(111)	0.075	2.53
Ni(100)	0.59	2.10

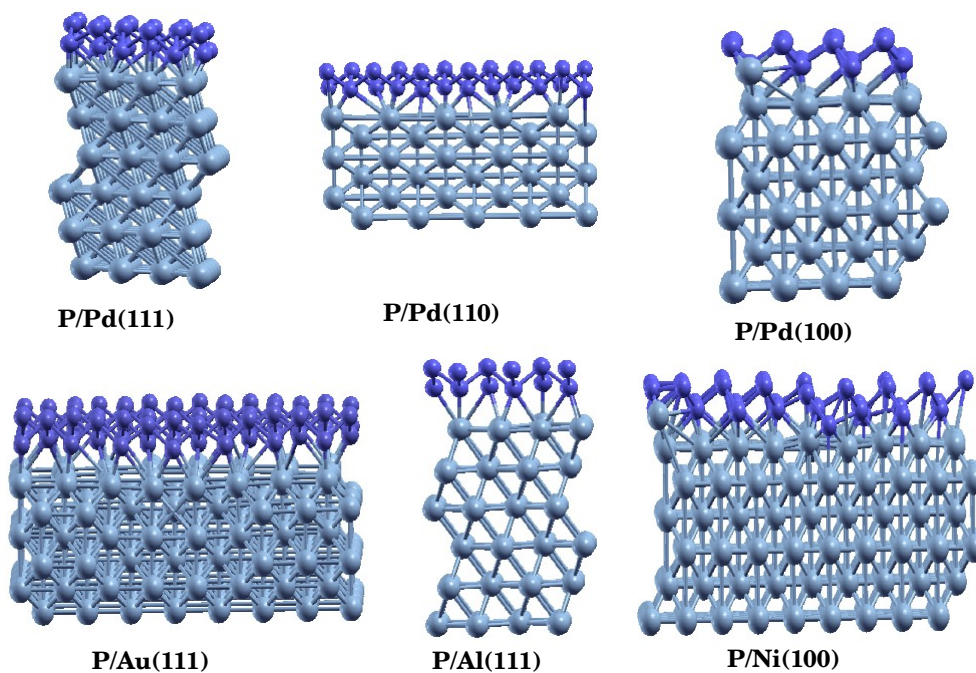


Figure 6.3: side views of blue phosphorene on different metal surfaces

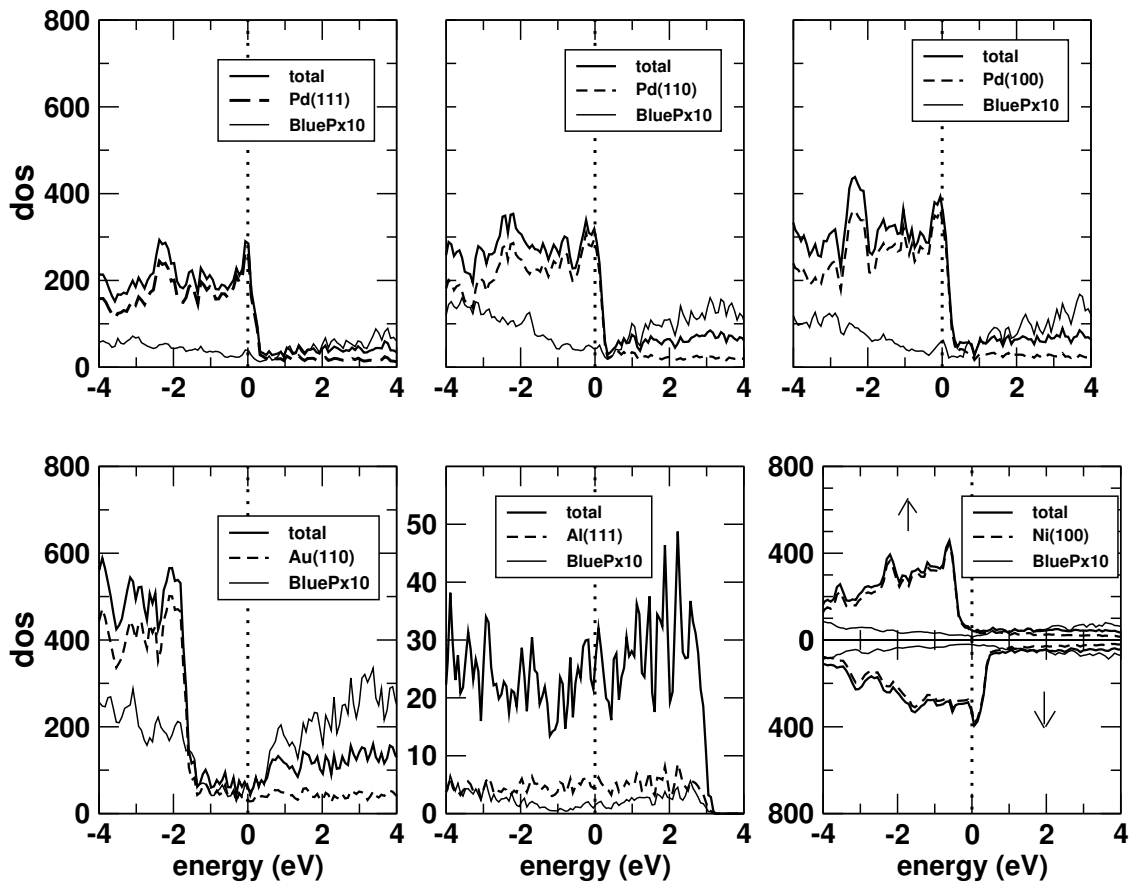


Figure 6.4: Density of states of metal/blue phosphorene system. Projected density of states of metal are shown. Energies are drawn with respect to Fermi system

## 6.2.4 Schottky barrier height at metal/blue phosphorene interface

The charge carrier injection efficiency and the contact behavior, i.e. p-type or n-type can be understood from Schottky barrier height. Schottky barrier height (SBH) is determined from the simple Schottky-Mott model. This model is based on few assumptions: (a) The surface dipole does not affect the (i) work function of the metal (ii) the electron affinity and (iii) ionization potential of the semiconductor, (b) There are no localized states at the surface of the semiconductor and thus forming a perfect contact with metal, (c) No chemical reaction occurs between metal-semiconductor and the surfaces are strain free. The work function of the metal is defined as the difference between vacuum level and the fermi energy of the metal. The electron affinity (ionization potential) is defined as the difference between vacuum level and CBM (VBM) of the semiconductor.

According to Schottky-Mott model if the vacuum level of metal and semiconductor are aligned, the SBH for n-type (p-type) semiconductor is defined as the difference between Fermi level of the metal and electron affinity (ionization potential) of the semiconductor.

$$\Phi_n = \Phi_M - \chi_{sc} \quad (6.3)$$

$$\Phi_p = I_{sc} - \Phi_M \quad (6.4)$$

where  $\chi_{sc}$  and  $I_{sc}$  are the electron affinity and ionization potential of the semiconductor, respectively. The method to calculate the vacuum energy is given extensively in chapter 4.

Smoluchowski[93] argued that different packing density on different surfaces of a metal leads to different values of the "smoothing" dipole moment. Eventually this affects the work function of that surface. Densely packed surface shows less smoothing which results in large work function. According to this theory Pd(111) surface is more densely packed surface than Pd(110) and Pd(100) surfaces. Therefore, the work functions in ascending order are 5.24, 5.11 and 4.79 eV for Pd(111), Pd(100), Pd(110) respectively. Work functions of Au(110), Al(111) and Ni(100) are 4.75, 4.02 and 4.70 eV respectively.

In case of bulk semiconductor and bulk metal interface, a space charge layer is formed at the

Table 6.4: electron schottky barrier height ( $e_{SBH}$  in eV) and hole schottky barrier height ( $h_{SBH}$  in eV) at metal/blue phosphorene interface

Metal surface/BlueP	$e_{SBH}$	$h_{SBH}$
Pd(111)/P	0.32	1.61
Pd(110)/P	0.40	1.53
Pd(100)/P	0.39	1.54
Al(110)/P	0.00	4.46
Au(110)/P	0.26	1.67
Ni(100)/P	1.17	1.30

Table 6.5: Tunnel barrier height (TBH in eV) and tunnel barrier width (TBW in Å) in metal surface/ blue phosphorene interface

Metal surface/Blue P	TBH	TBW
Pd(111)/P	0.00	0.00
Pd(110)/P	0.46	0.86
Pd(100)/P	0.28	0.96
Au(110)/P	1.80	0.99
Al(111)/P	2.33	1.19
Ni(100)/P	0.00	0.00

semiconductor side. This layer affects the Schottky barrier height value which is the difference of metal work function and EA and IP of the semiconductor. Monolayer blue phosphorene metallizes after making contact with metal as shown in partial DOS of blue P in fig 6.4. Therefore, there is no vertical barrier height found which injects carrier from metal to phosphorene. Here we are calculating the lateral Schottky barrier height which describes the lateral charge injection from metal/monolayer blue phosphorene composite to monolayer blue phosphorene. The definition of Schottky barrier height is modified as follows: the electron (hole) SBH is the difference between Fermi level of metal/ monolayer blue phosphorene composite system and CBM (VBM) of semiconductor.

The results of lateral SBH are given in table 6.4 and the energy diagram of lateral SBH is shown in fig 6.5. Except Al all other surfaces show finite SBH for both electrons and holes. For all surfaces electron SBH is smaller than hole SBH. Therefore, all the surfaces are made good n-type contact with blue phosphorene.

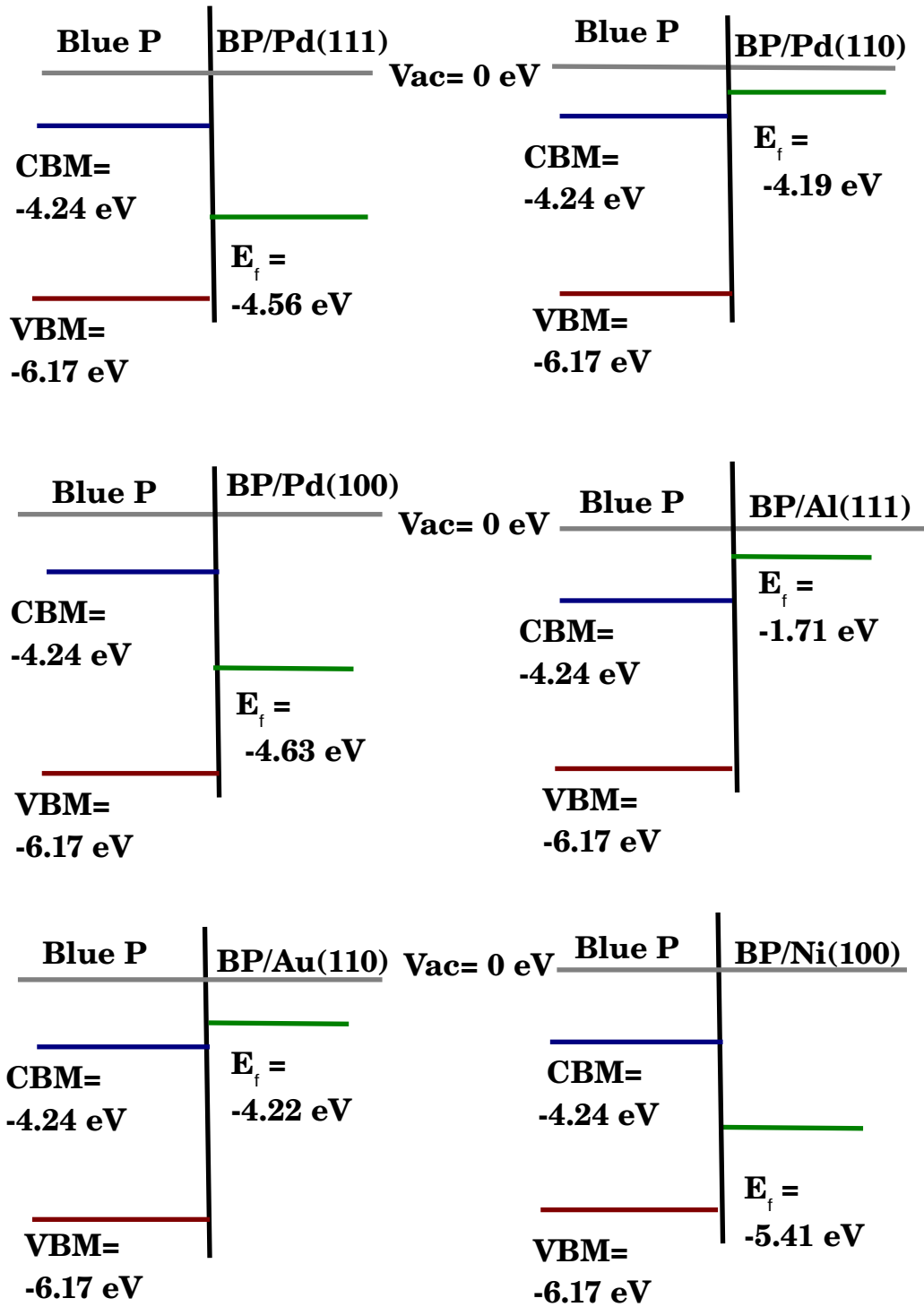


Figure 6.5: Electron and hole lateral SBH are shown in figure. Green lines are fermi level for the metal/blue P composite system, Blue and red lines are conduction band minima and valence band maxima of blue phosphorene

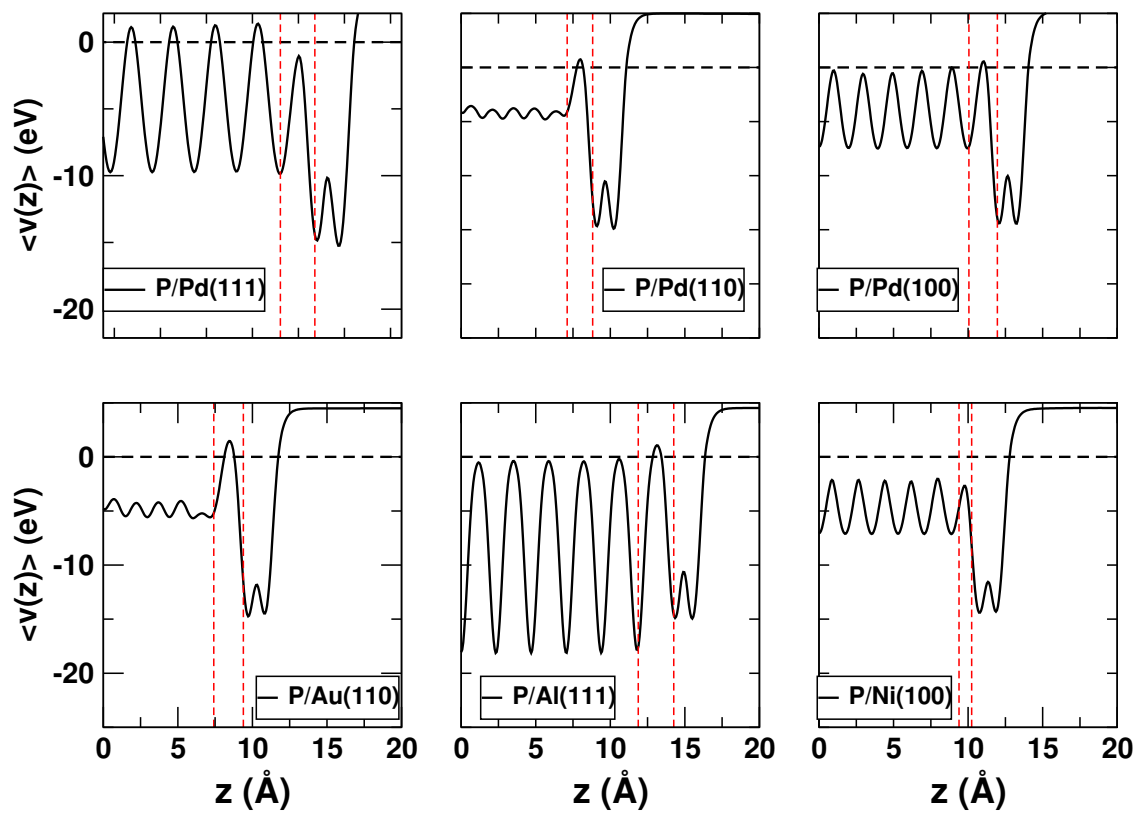


Figure 6.6: Variation of average electrostatic potential normal to interface, black dotted line is Fermi energy and red dotted lines are showing interface

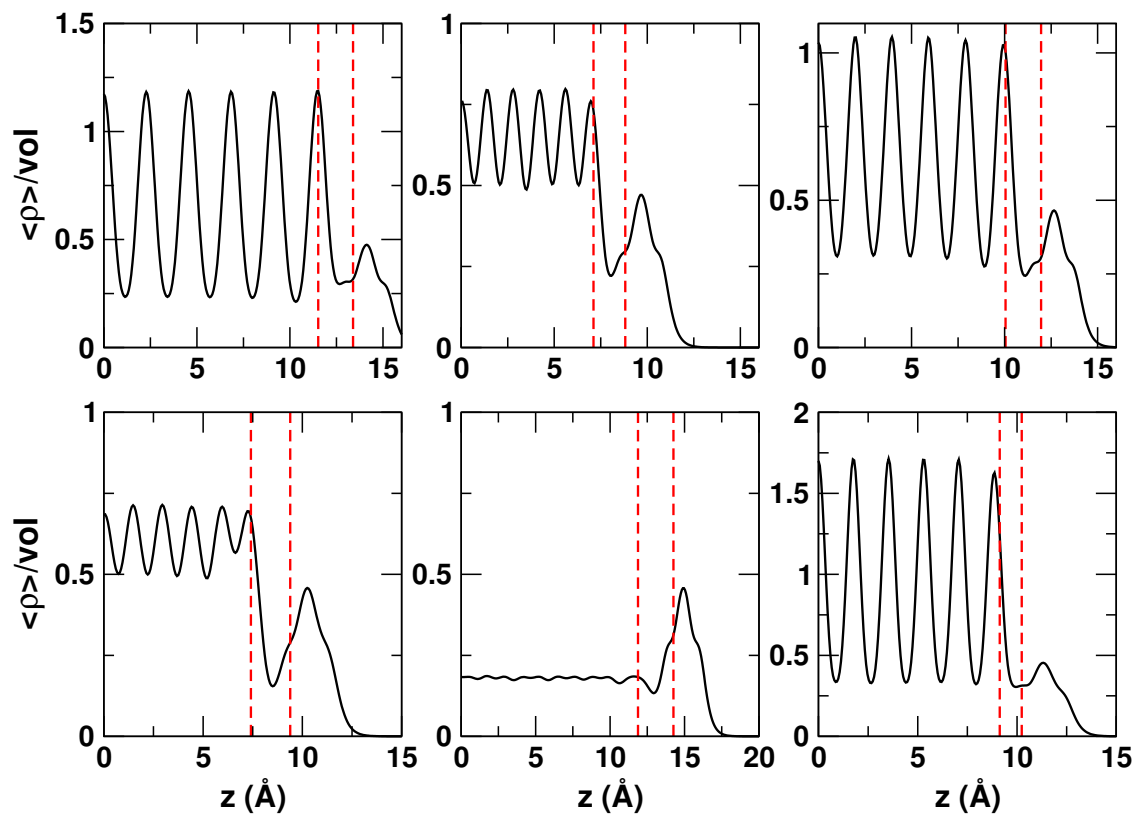


Figure 6.7: Variation of average charge density normal to interface, red dotted lines are showing interface

## 6.2.5 Tunnel barrier height at metal/blue phosphorene interface

Tunnel barrier height gives more microscopic description of metal/ monolayer blue phosphorene interfacial properties than Schottky barrier height. In ab-initio method, tunnel barrier height (TBH) is inferred from the variation of planar averaged electrostatic potential ( $v_e(z)$ ), which is the sum of Hartree potential ( $V_H$ ) and external potential ( $V_{ext}$ ) of an electron in a direction normal to the interface. The tunneling occurs with the electrons at the Fermi level. The TBH is defined as the maximum of  $v_e(z)$  at the metal/blue phosphorene interface with respect to Fermi energy ( $E_F$ ). If  $E_F$  of electrons is less than the highest value of the potential barrier at the interface, quantum mechanical tunnelling occurs through the barrier. On the other hand if  $E_F$  of electrons is larger than the highest value of the potential at the interface it will not be hindered by any barrier.

The results of TBH and the barrier width are given in table 6.5 and the profile of  $v_e(z)$  is shown in figure 6.6. We find that only the interfaces made by Pd(111) and Ni(100) with blue phosphorene show no tunneling. The reason behind no tunneling is the  $E_F$  of the system is higher than  $v_e(z)$  at the interface. In all other cases i.e. the interfaces made by Pd(110), Pd(100), Au(110) and Al(111) with blue phosphorene has finite tunnel barrier height and width. From table 6.2 it is seen that the Al(111) surface shows weak binding (0.075 eV/P atom) with blue phosphorene than other metal surface which may be the reason of largest TBH at the interface. Au(110) and Pd(110) shows better binding in ascending order with blue P than Al(111) (0.18 eV/P atom for Au(110)/P and 0.36 eV/P atom for Pd(110)/P). This results smaller TBH (1.80 eV for Au(110)/blue P and 0.46 eV for Pd(110)/blue P) at the interface. Pd(111) gives marginally smaller binding energy (0.42 eV/P atom) with blue P than Pd(100)/blue P system (0.44 eV/P atom). But Pd(111) has the same hexagonal lattice structure as the blue P, whereas Pd(100) has rectangular lattice structure. This causes maximum overlap of orbitals in Pd(111) than Pd(100). This may be the reason that in spite of smaller binding energy between Pd(111)/blue P than Pd(100)/P, the former one shows no TBH whereas the later shows finite TBH. The maximum binding energy occurs in between Ni(100)/blue P system (0.59 eV/P atom) and also from the fig 6.3 it is seen that blue P is maximally distorted on the Ni(100) surface. This may result zero TBH at Ni(100)/blue P interface. From figure 6.7 it is

seen that the charge density at the interface is larger for Pd(111) and Ni(100) surfaces than others. This may be the reason that P/Pd(111) and P/Ni(100) interfaces has zero TBH. For Al(111) the interfacial charge is lowest which may be the reason of finite tunnel barrier at the interface.

### 6.3 Discussion

We compare now the results of tunnel barrier height between blue phosphorene and black phosphorene (monolayer black phosphorus). Pd(111), Pd(110), Pd(100) surfaces gives zero TBH for black phosphorene. On the contrary only Pd(111) surface gives zero TBH with blue phosphorene, whereas finite TBH with Pd(110) and Pd(100). Al(111) surface has shown finite TBH with black phosphorene. In our result we have found that Al(111)/blue phosphorene interface also give large TBH. The Au(110)/blue phosphorene shows non zero TBH, which has also found in Au(110)/black phosphorene interface.

In experimental studies Pd surface was found as p-type contact with few layer black phosphorus. In case of blue phosphorene, Pd(111) and Pd(100) surface shows finite SBH for both electrons and holes. The SBH for electrons and holes of Pd(111) and Pd(100) are marginally different. Pd(110)/blue phosphorene interface shows finite SBH for electrons, whereas Pd(110)/black phosphorus gives finite SBH for both electrons and holes. Au(110) and Al(111) surfaces make n-type contact with blue phosphorene by making zero electron SBH. On the other hand Au(110) shows very small (0.01 eV) hole SBH and 0.89 eV electron SBH with black phosphorene.

### 6.4 Conclusion

We have studied tunnel barrier height and Schottky barrier height between blue phosphorene with Pd(111), Pd(110), Pd(100), Al(111), Au(110) and Ni(100) surfaces. The mobility of electron and hole is small in blue phosphorene, whereas the band gap is large. By tuning the mobility or concentration of carrier externally, blue phosphorene can be used in devices. In the presence of high electric field, instead of mobility, the saturation velocity is an important factor in FET devices.

There is no experimental report till now about the saturation velocity of blue phosphorene.

Nevertheless, we have found that all the metal surfaces we have chosen shows finite Schottky barrier height for electrons and hole at the interface with blue phosphorene. Pd(111) and Ni(100) surface gives zero TBH among all the surfaces. These results are assumed to be helpful to choose metal surface to make contact with blue phosphorene.





# Bibliography

- [1] K. S. Novoselov, A. K. Geim, S. V. Morozov, D. Jiang, Y. Zhang, S. V. Dubonos, I. V. Grigorieva, and A. A. Firsov, “Electric field effect in atomically thin carbon films,” *Science* **306** no. 5696, (2004) 666–669, <http://science.sciencemag.org/content/306/5696/666.full.pdf>.
- [2] N. et al., “Two-dimensional gas of massless dirac fermions in graphene,” *Nature* **438** no. 197, (2005) 1.
- [3] Z. et al., “Experimental observation of the quantum hall effect and berry’s phase in graphene,” *Nature* **438** no. 201, (2005) 1.
- [4] S. V. Morozov, K. S. Novoselov, M. I. Katsnelson, F. Schedin, D. C. Elias, J. A. Jaszczak, and A. K. Geim, “Giant intrinsic carrier mobilities in graphene and its bilayer,” *Phys. Rev. Lett.* **100** (Jan, 2008) 016602.
- [5] A. A. Balandin, S. Ghosh, W. Bao, I. Calizo, D. Teweldebrhan, F. Miao, and C. N. Lau, “Superior thermal conductivity of single-layer graphene,” *Nano Letters* **8** no. 3, (2008) 902–907. PMID: 18284217.
- [6] C. Lee, X. Wei, J. W. Kysar, and J. Hone, “Measurement of the elastic properties and intrinsic strength of monolayer graphene,” *Science* **321** no. 5887, (2008) 385–388, <http://science.sciencemag.org/content/321/5887/385.full.pdf>.

- [7] B. Lalmi, H. Oughaddou, H. Enriquez, A. Kara, S. Vizzini, B. Ealet, and B. Aufray, “Epitaxial growth of a silicene sheet,” *Applied Physics Letters* **97** no. 22, (2010) 223109.
- [8] P. De Padova, C. Quaresima, C. Ottaviani, P. M. Sheverdyaeva, P. Moras, C. Carbone, D. Topwal, B. Olivieri, A. Kara, H. Oughaddou, B. Aufray, and G. Le Lay, “Evidence of graphene-like electronic signature in silicene nanoribbons,” *Applied Physics Letters* **96** no. 26, (2010) 261905.
- [9] M. Rachid Tchalala, H. Enriquez, A. J. Mayne, A. Kara, S. Roth, M. G. Silly, A. Bendounan, F. Sirotti, T. Greber, B. Aufray, G. Dujardin, M. Ait Ali, and H. Oughaddou, “Formation of one-dimensional self-assembled silicon nanoribbons on au(110)-(2x1),” *Applied Physics Letters* **102** no. 8, (2013) 083107.
- [10] L. Meng, Y. Wang, L. Zhang, S. Du, R. Wu, L. Li, Y. Zhang, G. Li, H. Zhou, W. A. Hofer, and H.-J. Gao, “Buckled silicene formation on ir(111),” *Nano Letters* **13** no. 2, (2013) 685–690. PMID: 23330602.
- [11] C. Daniele, S. Emilio, C. Eugenio, G. Carlo, van den Broek Bas, F. Marco, H. Michel, and M. Alessandro, “Two-dimensional si nanosheets with local hexagonal structure on a mos<sub>2</sub> surface,” *Advanced Materials* **26** no. 13, 2096–2101.
- [12] A. Fleurence, R. Friedlein, T. Ozaki, H. Kawai, Y. Wang, and Y. Yamada-Takamura, “Experimental evidence for epitaxial silicene on diboride thin films,” *Phys. Rev. Lett.* **108** (Jun, 2012) 245501.
- [13] C. Volders, E. Monazami, G. Ramalingam, and P. Reinke, “Alternative route to silicene synthesis via surface reconstruction on h-mosi<sub>2</sub> crystallites,” *Nano Letters* **17** no. 1, (2017) 299–307. PMID: 27997208.
- [14] T. Morishita, S. P. Russo, I. K. Snook, M. J. S. Spencer, K. Nishio, and M. Mikami, “First-principles study of structural and electronic properties of ultrathin silicon nanosheets,” *Phys. Rev. B* **82** (Jul, 2010) 045419.

- [15] C.-C. Liu, W. Feng, and Y. Yao, “Quantum spin hall effect in silicene and two-dimensional germanium,” *Phys. Rev. Lett.* **107** (Aug, 2011) 076802.
- [16] J.-T. Sun, Z. Wang, S. Meng, S. Du, F. Liu, and H.-J. Gao, “Spin-polarized valley hall effect in ultrathin silicon nanomembrane via interlayer antiferromagnetic coupling,” *2D Materials* **3** no. 3, (2016) 035026.
- [17] M. Pal, U. Pal, J. M. G. Y. Jiménez, and F. Pérez-Rodríguez, “Effects of crystallization and dopant concentration on the emission behavior of tio<sub>2</sub>:eu nanophosphors,” *Nanoscale Research Letters* **7** no. 1, (Jan, 2012) 1.
- [18] C.-w. Zhang and S.-s. Yan, “First-principles study of ferromagnetism in two-dimensional silicene with hydrogenation,” *The Journal of Physical Chemistry C* **116** no. 6, (2012) 4163–4166.
- [19] Y. Guo, S. Zhou, Y. Bai, and J. Zhao, “Tunable thermal conductivity of silicene by germanium doping,” *Journal of Superconductivity and Novel Magnetism* **29** no. 3, (Mar, 2016) 717–720.
- [20] R. wu Zhang, C. wen Zhang, S. shi Li, W. xiao Ji, P. ji Wang, F. Li, P. Li, M. juan Ren, and M. Yuan, “Design of half-metallic ferromagnetism in germanene/silicene hybrid sheet,” *Solid State Communications* **191** (2014) 49 – 53.
- [21] W.-S. Kim, Y. Hwa, J.-H. Shin, M. Yang, H.-J. Sohn, and S.-H. Hong, “Scalable synthesis of silicon nanosheets from sand as an anode for li-ion batteries,” *Nanoscale* **6** (2014) 4297–4302.
- [22] H. L. Zhuang and R. G. Hennig, “Theoretical perspective of photocatalytic properties of single-layer sns<sub>2</sub>,” *Phys. Rev. B* **88** (Sep, 2013) 115314.
- [23] M. E. Dvila, L. Xian, S. Cahangirov, A. Rubio, and G. L. Lay, “Germanene: a novel

- two-dimensional germanium allotrope akin to graphene and silicene,” *New Journal of Physics* **16** no. 9, (2014) 095002.
- [24] M. Derivaz, D. Dentel, R. Stephan, M.-C. Hanf, A. Mehdaoui, P. Sonnet, and C. Pirri, “Continuous germanene layer on al(111),” *Nano Letters* **15** no. 4, (2015) 2510–2516. PMID: 25802988.
- [25] A. OHare, F. V. Kusmartsev, and K. I. Kugel, “A stable ”flat” form of two-dimensional crystals: Could graphene, silicene, germanene be minigap semiconductors?,” *Nano Letters* **12** no. 2, (2012) 1045–1052. PMID: 22236130.
- [26] M. Houssa, G. Pourtois, V. V. Afanasev, and A. Stesmans, “Electronic properties of two-dimensional hexagonal germanium,” *Applied Physics Letters* **96** no. 8, (2010) 082111.
- [27] O. Pulci, P. Gori, M. Marsili, V. Garbuio, R. D. Sole, and F. Bechstedt, “Strong excitons in novel two-dimensional crystals: Silicane and germanane,” *EPL (Europhysics Letters)* **98** no. 3, (2012) 37004.
- [28] X.-S. Ye, Z.-G. Shao, H. Zhao, L. Yang, and C.-L. Wang, “Intrinsic carrier mobility of germanene is larger than graphene’s: first-principle calculations,” *RSC Adv.* **4** (2014) 21216–21220.
- [29] X.-S. Ye, Z.-G. Shao, H. Zhao, L. Yang, and C.-L. Wang, “Intrinsic carrier mobility of germanene is larger than graphene’s: first-principle calculations,” *RSC Adv.* **4** (2014) 21216–21220.
- [30] L. Zhang, P. Bampoulis, A. van Houselt, and H. J. W. Zandvliet, “Two-dimensional dirac signature of germanene,” *Applied Physics Letters* **107** no. 11, (2015) 111605.
- [31] Davila, M. E. L. Lay, and G, “Few layer epitaxial germanene: a novel two-dimensional dirac material,” *Scientific Reports* **6** no. 20714, (2016) 1.

- [32] J.-A. Yan, R. Stein, D. M. Schaefer, X.-Q. Wang, and M. Y. Chou, “Electron-phonon coupling in two-dimensional silicene and germanene,” *Phys. Rev. B* **88** (Sep, 2013) 121403.
- [33] Y. Han, J. Dong, G. Qin, and M. Hu, “Phonon transport in the ground state of two-dimensional silicon and germanium,” *RSC Adv.* **6** (2016) 69956–69965.
- [34] L.-F. Huang, P.-L. Gong, and Z. Zeng, “Phonon properties, thermal expansion, and thermomechanics of silicene and germanene,” *Phys. Rev. B* **91** (May, 2015) 205433.
- [35] B. Bishnoi and B. Ghosh, “Spin transport in silicene and germanene,” *RSC Adv.* **3** (2013) 26153–26159.
- [36] R.-w. Zhang, W.-x. Ji, C.-w. Zhang, S.-s. Li, P. Li, P.-j. Wang, F. Li, and M.-j. Ren, “Controllable electronic and magnetic properties in a two-dimensional germanene heterostructure,” *Phys. Chem. Chem. Phys.* **18** (2016) 12169–12174.
- [37] F. Bechstedt, L. Matthes, P. Gori, and O. Pulci, “Infrared absorbance of silicene and germanene,” *Applied Physics Letters* **100** no. 26, (2012) 261906.
- [38] W. Wei, Y. Dai, B. Huang, and T. Jacob, “Many-body effects in silicene, silicane, germanene and germanane,” *Phys. Chem. Chem. Phys.* **15** (2013) 8789–8794.
- [39] F. Bechstedt, L. Matthes, P. Gori, and O. Pulci, “Infrared absorbance of silicene and germanene,” *Applied Physics Letters* **100** no. 26, (2012) 261906.
- [40] Z. Ni, Q. Liu, K. Tang, J. Zheng, J. Zhou, R. Qin, Z. Gao, D. Yu, and J. Lu, “Tunable bandgap in silicene and germanene,” *Nano Letters* **12** no. 1, (2012) 113–118. PMID: 22050667.
- [41] Zhu, C. Feng-feng, X. Wei-jiong, G. Yong, G. Chun-lei, L. Dan-dan, Q. Can-hua, Z. Dong, J. Shou-Cheng, and Jin-feng, “Epitaxial growth of two-dimensional stanene,” *Nature Materials* **14** no. 1020, (2015) 1.

- [42] L. Tao, C. Yang, L. Wu, L. Han, Y. Song, S. Wang, and P. Lu, “Tension-induced mechanical properties of stanene,” *Modern Physics Letters B* **30** no. 12, (2016) 1650146.
- [43] M. J. Cherukara, B. Narayanan, A. Kinaci, K. Sasikumar, S. K. Gray, M. K. Chan, and S. K. R. S. Sankaranarayanan, “Ab initio-based bond order potential to investigate low thermal conductivity of stanene nanostructures,” *The Journal of Physical Chemistry Letters* **7** no. 19, (2016) 3752–3759. PMID: 27569053.
- [44] A. S. Nissimagoudar, A. Manjanath, and A. K. Singh, “Diffusive nature of thermal transport in stanene,” *Phys. Chem. Chem. Phys.* **18** (2016) 14257–14263.
- [45] B. van den Broek, M. Houssa, E. Scalise, G. Pourtois, V. V. Afanasev, and A. Stesmans, “Two-dimensional hexagonal tin: ab initio geometry, stability, electronic structure and functionalization,” *2D Materials* **1** no. 2, (2014) 021004.
- [46] M. Houssa, B. van den Broek, K. Iordanidou, A. K. A. Lu, G. Pourtois, J.-P. Locquet, V. Afanas’ev, and A. Stesmans, “Topological to trivial insulating phase transition in stanene,” *Nano Research* **9** no. 3, (Mar, 2016) 774–778.
- [47] S. Rachel and M. Ezawa, “Giant magnetoresistance and perfect spin filter in silicene, germanene, and stanene,” *Phys. Rev. B* **89** (May, 2014) 195303.
- [48] Y. Shaidu and O. Akin-Ojo, “First principles predictions of superconductivity in doped stanene,” *Computational Materials Science* **118** (2016) 11 – 15.
- [49] H. Zhang, J. Zhang, B. Zhao, T. Zhou, and Z. Yang, “Quantum anomalous hall effect in stable dumbbell stanene,” *Applied Physics Letters* **108** no. 8, (2016) 082104.
- [50] A. J. Mannix, X.-F. Zhou, B. Kiraly, J. D. Wood, D. Alducin, B. D. Myers, X. Liu, B. L. Fisher, U. Santiago, J. R. Guest, M. J. Yacaman, A. Ponce, A. R. Oganov, M. C. Hersam, and N. P. Guisinger, “Synthesis of borophenes: Anisotropic, two-dimensional boron polymorphs,” *Science* **350** no. 6267, (2015) 1513–1516.

- [51] Feng, Z. B., Z. J., L. Q., L. W., L. S., C. H., M. P., C. S., W. L., and K., “Experimental realization of two-dimensional boron sheets,” *Nature Chemistry* **8** no. 563, (2016) 1.
- [52] T. Guoan, H. Tingsong, Z. Yungang, W. Xufeng, K. Jizhou, Z. Tian, Y. Yuncheng, and W. Qin, “Synthesis of atomically thin boron films on copper foils,” *Angewandte Chemie International Edition* **54** no. 51, 15473–15477, <https://onlinelibrary.wiley.com/doi/pdf/10.1002/anie.201509285>.
- [53] B. Zheng, H. tao Yu, Y. fu Lian, and Y. Xie, “Novel  $\alpha$ - and  $\beta$ -type boron sheets: Theoretical insight into their structures, thermodynamic stability, and work functions,” *Chemical Physics Letters* **648** (2016) 81 – 86.
- [54] X.-F. Zhou, A. R. Oganov, Z. Wang, I. A. Popov, A. I. Boldyrev, and H.-T. Wang, “Two-dimensional magnetic boron,” *Phys. Rev. B* **93** (Feb, 2016) 085406.
- [55] J. Li, H. Zhang, and G. Yang, “Ultrahigh-capacity molecular hydrogen storage of a lithium-decorated boron monolayer,” *The Journal of Physical Chemistry C* **119** no. 34, (2015) 19681–19688.
- [56] S. H. Mir, S. Chakraborty, P. C. Jha, J. Wrn, H. Soni, P. K. Jha, and R. Ahuja, “Two-dimensional boron: Lightest catalyst for hydrogen and oxygen evolution reaction,” *Applied Physics Letters* **109** no. 5, (2016) 053903.
- [57] C. Wu, H. Wang, J. Zhang, G. Gou, B. Pan, and J. Li, “Lithiumboron (lib) monolayers: First-principles cluster expansion and possible two-dimensional superconductivity,” *ACS Applied Materials & Interfaces* **8** no. 4, (2016) 2526–2532. PMID: 26732306.
- [58] H.-S. Tsai, S.-W. Wang, C.-H. Hsiao, C.-W. Chen, H. Ouyang, Y.-L. Chueh, H.-C. Kuo, and J.-H. Liang, “Direct synthesis and practical bandgap estimation of multilayer arsenene nanoribbons,” *Chemistry of Materials* **28** no. 2, (2016) 425–429.

- [59] M. Zeraati, S. M. Vaez Allaei, I. Abdolhosseini Sarsari, M. Pourfath, and D. Donadio, “Highly anisotropic thermal conductivity of arsenene: An ab initio study,” *Phys. Rev. B* **93** (Feb, 2016) 085424.
- [60] H. Zhang, Y. Ma, and Z. Chen, “Quantum spin hall insulators in strain-modified arsenene,” *Nanoscale* **7** (2015) 19152–19159.
- [61] A. Pablo, A.-G. Fernando, R.-S.-M. David, A. D. A., D.-T. Sergio, A. Manuel, M. Fernando, G.-H. Julio, and Z. Flix, “Mechanical isolation of highly stable antimonene under ambient conditions,” *Advanced Materials* **28** no. 30, 6332–6336, <https://onlinelibrary.wiley.com/doi/pdf/10.1002/adma.201602128>.
- [62] G. Carlos, R.-S.-M. David, A. Pablo, G.-H. Julio, V. Maria, G. Roland, M. Janina, H. Frank, H. Andreas, A. Gonzalo, and Z. Flix, “Few-layer antimonene by liquid-phase exfoliation,” *Angewandte Chemie International Edition* **55** no. 46, 14345–14349, <https://onlinelibrary.wiley.com/doi/pdf/10.1002/anie.201605298>.
- [63] W. Xu, S. Yan, L. Hang, F. Zili, W. Ye-Liang, S. Jia-Tao, L. Chen, W. Jia-Ou, L. Zhong-Liu, Z. Shi-Yu, W. Yu-Qi, D. Shi-Xuan, S. You-Guo, I. Kurash, and G. Hong-Jun, “Epitaxial growth and air-stability of monolayer antimonene on pdte<sub>2</sub>,” *Advanced Materials* **29** no. 11, 1605407, <https://onlinelibrary.wiley.com/doi/pdf/10.1002/adma.201605407>.
- [64] Ji, S. J., L. X., Y. J., H. Z., Z. C., S. S., L. M., W. L., and e. a. W.; Ni and Z., “Two-dimensional antimonene single crystals grown by van der waals epitaxy,” *Nature Communications* **7** (2016) 1.
- [65] L. Yang, Y. Song, W. Mi, and X. Wang, “The electronic structure and spinorbit-induced spin splitting in antimonene with vacancy defects,” *RSC Adv.* **6** (2016) 66140–66146.
- [66] S. K. Gupta, Y. Sonvane, G. Wang, and R. Pandey, “Size and edge roughness effects on

- thermal conductivity of pristine antimonene allotropes,” *Chemical Physics Letters* **641** (2015) 169 – 172.
- [67] Y. Hu, Y. Wu, and S. Zhang, “Influences of stonewales defects on the structure, stability and electronic properties of antimonene: A first principle study,” *Physica B: Condensed Matter* **503** (2016) 126 – 129.
- [68] D. Singh, S. K. Gupta, Y. Sonvane, and I. Lukaevi, “Antimonene: a monolayer material for ultraviolet optical nanodevices,” *J. Mater. Chem. C* **4** (2016) 6386–6390.
- [69] G. Wang, R. Pandey, and S. P. Karna, “Atomically thin group v elemental films: Theoretical investigations of antimonene allotropes,” *ACS Applied Materials & Interfaces* **7** no. 21, (2015) 11490–11496. PMID: 25955131.
- [70] Z. Shengli, Y. Zhong, L. Yafei, C. Zhongfang, and Z. Haibo, “Atomically thin arsenene and antimonene: Semimetalsemiconductor and indirect-direct band-gap transitions,” *Angewandte Chemie International Edition* **54** no. 10, 3112–3115, <https://onlinelibrary.wiley.com/doi/pdf/10.1002/anie.201411246>.
- [71] Nagao, Y. T., S. S., K. M., S. T., O. J. T., H. T., S. S., and T, “Strong lateral growth and crystallization via two-dimensional allotropic transformation of semi-metal bi film,” *Surf. Sci.* **590** no. 1, (2005) 247252.
- [72] V. Tran and L. Yang, “Scaling laws for the band gap and optical response of phosphorene nanoribbons,” *Phys. Rev. B* **89** (Jun, 2014) 245407.
- [73] P. W. Bridgman, “Two new modifications of phosphorus.,” *Journal of the American Chemical Society* **36** no. 7, (1914) 1344–1363.
- [74] E. N. Rissi, E. Soignard, K. A. McKiernan, C. J. Benmore, and J. L. Yarger, “Pressure-induced crystallization of amorphous red phosphorus,” *Solid State Communications* **152** no. 5, (2012) 390 – 394.

- [75] S. Endo, Y. Akahama, S. ichi Terada, and S. ichiro Narita, "Growth of large single crystals of black phosphorus under high pressure," *Japanese Journal of Applied Physics* **21** no. 8A, (1982) L482.
- [76] W. K. Krebs H, Weitz H, "Die katalytische darstellung des schwarzen phosphors [The catalytic preparation of black phosphorus]," *Acta Crystallographica* **280** no. 1-3, (1955) 119133.
- [77] A. Brown and S. Rundqvist, "Refinement of the crystal structure of black phosphorus," *Acta Crystallographica* **19** no. 4, (Oct, 1965) 684–685.
- [78] S. Lange, P. Schmidt, and T. Nilges, "Au<sub>3</sub>Sn<sub>7</sub> black phosphorus: An easy access to black phosphorus," *Inorganic Chemistry* **46** no. 10, (2007) 4028–4035. PMID: 17439206.
- [79] T. Nilges, M. Kersting, and T. Pfeifer, "A fast low-pressure transport route to large black phosphorus single crystals," *Journal of Solid State Chemistry* **181** no. 8, (2008) 1707 – 1711.
- [80] M. Kpf, N. Eckstein, D. Pfister, C. Grotz, I. Krger, M. Greiwe, T. Hansen, H. Kohlmann, and T. Nilges, "Access and in situ growth of phosphorene-precursor black phosphorus," *Journal of Crystal Growth* **405** (2014) 6 – 10.
- [81] Xia, W. Fengnian, J. Han, and Yichen, "Rediscovering black phosphorus as an anisotropic layered material for optoelectronics and electronics," *Nature Communications* **5** no. 4458, (2014) 1.
- [82] H. Liu, A. T. Neal, Z. Zhu, Z. Luo, X. Xu, D. Tomnek, and P. D. Ye, "Phosphorene: An unexplored 2d semiconductor with a high hole mobility," *ACS Nano* **8** no. 4, (2014) 4033–4041. PMID: 24655084.
- [83] S. P. Koenig, R. A. Doganov, H. Schmidt, A. H. Castro Neto, and B. zyilmaz, "Electric field effect in ultrathin black phosphorus," *Applied Physics Letters* **104** no. 10, (2014) 103106.

- [84] Z. Xiao, X. Haiming, L. Zhengdong, T. Chaoliang, L. Zhimin, L. Hai, L. Jiadan, S. Liqun, C. Wei, X. Zhichuan, X. Linghai, H. Wei, and Z. Hua, “Black phosphorus quantum dots,” *Angewandte Chemie International Edition* **54** no. 12, 3653–3657, <https://onlinelibrary.wiley.com/doi/pdf/10.1002/anie.201409400>.
- [85] Y. Poya, K. Bijandra, F. Tara, W. Canhui, A. Mohammad, T. David, I. J. Ernesto, K. R. F., and S.-K. Amin, “High-quality black phosphorus atomic layers by liquid-phase exfoliation,” *Advanced Materials* **27** no. 11, 1887–1892, <https://onlinelibrary.wiley.com/doi/pdf/10.1002/adma.201405150>.
- [86] V. Sresht, A. A. H. Pdua, and D. Blankschtein, “Liquid-phase exfoliation of phosphorene: Design rules from molecular dynamics simulations,” *ACS Nano* **9** no. 8, (2015) 8255–8268. PMID: 26192620.
- [87] A. H. Woomer, T. W. Farnsworth, J. Hu, R. A. Wells, C. L. Donley, and S. C. Warren, “Phosphorene: Synthesis, scale-up, and quantitative optical spectroscopy,” *ACS Nano* **9** no. 9, (2015) 8869–8884. PMID: 26256770.
- [88] Hanlon and D. et al., “Liquid exfoliation of solvent-stabilized few-layer black phosphorus for applications beyond electronics,” *Nature Communications* **6** no. 8563, (2015) 1.
- [89] J. R. Brent, N. Savjani, E. A. Lewis, S. J. Haigh, D. J. Lewis, and P. O’Brien, “Production of few-layer phosphorene by liquid exfoliation of black phosphorus,” *Chem. Commun.* **50** (2014) 13338–13341.
- [90] H. Wang, X. Yang, W. Shao, S. Chen, J. Xie, X. Zhang, J. Wang, and Y. Xie, “Ultrathin black phosphorus nanosheets for efficient singlet oxygen generation,” *Journal of the American Chemical Society* **137** no. 35, (2015) 11376–11382. PMID: 26284535.
- [91] J. Jia, S. K. Jang, S. Lai, J. Xu, Y. J. Choi, J.-H. Park, and S. Lee, “Plasma-treated thickness-controlled two-dimensional black phosphorus and its electronic transport properties,” *ACS Nano* **9** no. 9, (2015) 8729–8736. PMID: 26301840.

- [92] R. Hultgren, N. S. Gingrich, and B. E. Warren, “The atomic distribution in red and black phosphorus and the crystal structure of black phosphorus,” *The Journal of Chemical Physics* **3** no. 6, (1935) 351–355.
- [93] R. Smoluchowski, “Anisotropy of the electronic work function of metals,” *Phys. Rev.* **60** (Nov, 1941) 661–674.
- [94] J.-W. Jiang and H. S. Park, “Mechanical properties of single-layer black phosphorus,” *Journal of Physics D: Applied Physics* **47** no. 38, (2014) 385304.
- [95] S. e. a. Lee, “Anisotropic in-plane thermal conductivity of black phosphorus nanoribbons at temperatures higher than 100k,” *Nature Communications* **6** no. 8673, (2015) 351–355.
- [96] G. Qin, Q.-B. Yan, Z. Qin, S.-Y. Yue, M. Hu, and G. Su, “Anisotropic intrinsic lattice thermal conductivity of phosphorene from first principles,” *Phys. Chem. Chem. Phys.* **17** (2015) 4854–4858.
- [97] Z. e. a. Luo, “Anisotropic in-plane thermal conductivity observed in few-layer black phosphorus,” *Nature Communications* **6** no. 8572, (2015) 1.
- [98] T. Low, A. S. Rodin, A. Carvalho, Y. Jiang, H. Wang, F. Xia, and A. H. Castro Neto, “Tunable optical properties of multilayer black phosphorus thin films,” *Phys. Rev. B* **90** (Aug, 2014) 075434.
- [99] H. Liu, A. T. Neal, Z. Zhu, Z. Luo, X. Xu, D. Tomnek, and P. D. Ye, “Phosphorene: An unexplored 2d semiconductor with a high hole mobility,” *ACS Nano* **8** no. 4, (2014) 4033–4041. PMID: 24655084.
- [100] L. Kou, T. Frauenheim, and C. Chen, “Phosphorene as a superior gas sensor: Selective adsorption and distinct iv response,” *The Journal of Physical Chemistry Letters* **5** no. 15, (2014) 2675–2681. PMID: 26277962.

- [101] M. Z. Rahman, C. W. Kwong, K. Davey, and S. Z. Qiao, “2d phosphorene as a water splitting photocatalyst: fundamentals to applications,” *Energy Environ. Sci.* **9** (2016) 709–728.
- [102] H. Y. Lv, W. J. Lu, D. F. Shao, and Y. P. Sun, “Enhanced thermoelectric performance of phosphorene by strain-induced band convergence,” *Phys. Rev. B* **90** (Aug, 2014) 085433.
- [103] A. Sibari, A. Marjaoui, M. Lakhal, Z. Kerrami, A. Kara, M. Benaissa, A. Ennaoui, M. Hamedoun, A. Benyoussef, and O. Mounkachi, “Phosphorene as a promising anode material for (li/na/mg)-ion batteries: A first-principle study,” *Solar Energy Materials and Solar Cells* **180** (2018) 253 – 257.
- [104] Y. Du, H. Liu, Y. Deng, and P. D. Ye, “Device perspective for black phosphorus field-effect transistors: Contact resistance, ambipolar behavior, and scaling,” *ACS Nano* **8** no. 10, (2014) 10035–10042. PMID: 25314022.
- [105] S. Das, M. Demarteau, and A. Roelofs, “Ambipolar phosphorene field effect transistor,” *ACS Nano* **8** no. 11, (2014) 11730–11738. PMID: 25329532.
- [106] P. et. al, “High-performance n-type black phosphorus transistors with type control via thickness and contact-metal engineering,” *Nature Communications* **6** no. 7809, (2015) 1.
- [107] L. et. al, “Black phosphorus field-effect transistors,” *Nature Nanotechnology* **9** no. 372, (2014) 1.
- [108] H. Liu, A. T. Neal, Z. Zhu, Z. Luo, X. Xu, D. Tomnek, and P. D. Ye, “Phosphorene: An unexplored 2d semiconductor with a high hole mobility,” *ACS Nano* **8** no. 4, (2014) 4033–4041. PMID: 24655084.
- [109] P. Masih Das, G. Danda, A. Cupo, W. M. Parkin, L. Liang, N. Kharche, X. Ling, S. Huang, M. S. Dresselhaus, V. Meunier, and M. Drndi, “Controlled sculpture of black phosphorus nanoribbons,” *ACS Nano* **10** no. 6, (2016) 5687–5695. PMID: 27192448.

- [110] Z. Zhu and D. Tománek, “Semiconducting layered blue phosphorus: A computational study,” *Phys. Rev. Lett.* **112** (May, 2014) 176802.
- [111] J. L. Zhang, S. Zhao, C. Han, Z. Wang, S. Zhong, S. Sun, R. Guo, X. Zhou, C. D. Gu, K. D. Yuan, Z. Li, and W. Chen, “Epitaxial growth of single layer blue phosphorus: A new phase of two-dimensional phosphorus,” *Nano Letters* **16** no. 8, (2016) 4903–4908. PMID: 27359041.
- [112] N. Han, N. Gao, and J. Zhao, “Initial growth mechanism of blue phosphorene on au(111) surface,” *The Journal of Physical Chemistry C* **121** no. 33, (2017) 17893–17899.
- [113] L.Z.Liu, X.L.Wu, X.X.Liu, and P. K.Chu, “Strain-induced band structure and mobility modulation in graphitic blue phosphorus,” *Applied Surface Science* **356** no. 17, (2015) 626 – 630.
- [114] Peng and Q. et al., “Electronic structures and enhanced optical properties of blue phosphorene/transition metal dichalcogenides van der waals heterostructures,” *Scientific Reports* **6** no. 31994, (2016) 1.
- [115] P. Hohenberg and W. Kohn, “Inhomogeneous electron gas,” *Phys. Rev.* **136** (Nov, 1964) B864–B871.
- [116] W. Kohn and L. J. Sham, “Self-consistent equations including exchange and correlation effects,” *Phys. Rev.* **140** (Nov, 1965) A1133–A1138.
- [117] D. M. Ceperley and B. J. Alder, “Ground state of the electron gas by a stochastic method,” *Phys. Rev. Lett.* **45** (Aug, 1980) 566–569.
- [118] S. H. Vosko, L. Wilk, and M. Nusair, “Accurate spin-dependent electron liquid correlation energies for local spin density calculations: a critical analysis,” *Canadian Journal of Physics* **58** no. 8, (1980) 1200–1211.

- [119] J. P. Perdew and Y. Wang, “Accurate and simple analytic representation of the electron-gas correlation energy,” *Phys. Rev. B* **45** (Jun, 1992) 13244–13249.
- [120] J. P. Perdew, K. Burke, and M. Ernzerhof, “Generalized gradient approximation made simple,” *Phys. Rev. Lett.* **77** (Oct, 1996) 3865–3868.
- [121] J. Heyd, G. E. Scuseria, and M. Ernzerhof, “Hybrid functionals based on a screened coulomb potential,” *The Journal of Chemical Physics* **118** no. 18, (2003) 8207–8215.
- [122] N. Troullier and J. L. Martins, “Efficient pseudopotentials for plane-wave calculations,” *Phys. Rev. B* **43** (Jan, 1991) 1993–2006.
- [123] N. Troullier and J. L. Martins, “Efficient pseudopotentials for plane-wave calculations. ii. operators for fast iterative diagonalization,” *Phys. Rev. B* **43** (Apr, 1991) 8861–8869.
- [124] G. P. Kerker, “Non-singular atomic pseudopotentials for solid state applications,” *Journal of Physics C: Solid State Physics* **13** no. 9, (1980) L189.
- [125] D. R. Hamann, M. Schlüter, and C. Chiang, “Norm-conserving pseudopotentials,” *Phys. Rev. Lett.* **43** (Nov, 1979) 1494–1497.
- [126] D. Vanderbilt, “Soft self-consistent pseudopotentials in a generalized eigenvalue formalism,” *Phys. Rev. B* **41** (Apr, 1990) 7892–7895.
- [127] S. Goedecker, M. Teter, and J. Hutter, “Separable dual-space gaussian pseudopotentials,” *Phys. Rev. B* **54** (Jul, 1996) 1703–1710.
- [128] P. E. Blöchl, “Projector augmented-wave method,” *Phys. Rev. B* **50** (Dec, 1994) 17953–17979.
- [129] G. Kresse and D. Joubert, “From ultrasoft pseudopotentials to the projector augmented-wave method,” *Phys. Rev. B* **59** (Jan, 1999) 1758–1775.
- [130] R. P. Feynman, “Forces in molecules,” *Phys. Rev.* **56** (Aug, 1939) 340–343.

- [131] S. Grimme, “Semiempirical gga type density functional constructed with a long-range dispersion correction,” *Journal of Computational Chemistry* **27** no. 15, 1787–1799.
- [132] M. Dion, H. Rydberg, E. Schröder, D. C. Langreth, and B. I. Lundqvist, “Van der waals density functional for general geometries,” *Phys. Rev. Lett.* **92** (Jun, 2004) 246401.
- [133] e. Qiao, “High-mobility transport anisotropy and linear dichroism in few-layer black phosphorus,” *Nature Communications* **5** no. 4475, (2016) 1.
- [134] M. Elahi, K. Khaliji, S. M. Tabatabaei, M. Pourfath, and R. Asgari, “Modulation of electronic and mechanical properties of phosphorene through strain,” *Phys. Rev. B* **91** (Mar, 2015) 115412.
- [135] R. Fei and L. Yang, “Strain-engineering the anisotropic electrical conductance of few-layer black phosphorus,” *Nano Letters* **14** no. 5, (2014) 2884–2889. PMID: 24779386.
- [136] A. Priyadarshi, Y. S. Chauhan, S. Bhowmick, and A. Agarwal, “Strain-tunable charge carrier mobility of atomically thin phosphorus allotropes,” *Phys. Rev. B* **97** (Mar, 2018) 115434.
- [137] Y. Pan, Y. Wang, M. Ye, R. Quhe, H. Zhong, Z. Song, X. Peng, D. Yu, J. Yang, J. Shi, and J. Lu, “Monolayer phosphorene-metal contacts,” *Chemistry of Materials* **28** no. 7, (2016) 2100–2109.
- [138] A. Chanana and S. Mahapatra, “First principles study of metal contacts to monolayer black phosphorous,” *Journal of Applied Physics* **116** no. 20, (2014) 204302.
- [139] S. Zhu, Y. Ni, J. Liu, and K. Yao, “The study of interaction and charge transfer at black phosphorus-metal interfaces,” *Journal of Physics D: Applied Physics* **48** no. 44, (2015) 445101.
- [140] J.-P. Jalkanen, M. Halonen, D. Fernandez-Torre, K. Laasonen, and L. Halonen, “A computational study of the adsorption of small ag and au nanoclusters on graphite,” *The Journal of Physical Chemistry A* **111** no. 49, (2007) 12317–12326. PMID: 17973466.

- [141] V. V. Kulish, O. I. Malyi, C. Persson, and P. Wu, “Adsorption of metal adatoms on single-layer phosphorene,” *Phys. Chem. Chem. Phys.* **17** (2015) 992–1000.
- [142] X. Sui, C. Si, B. Shao, X. Zou, J. Wu, B.-L. Gu, and W. Duan, “Tunable magnetism in transition-metal-decorated phosphorene,” *The Journal of Physical Chemistry C* **119** no. 18, (2015) 10059–10063.
- [143] I. Popov, G. Seifert, and D. Tománek, “Designing electrical contacts to  $\text{mos}_2$  monolayers: A computational study,” *Phys. Rev. Lett.* **108** (Apr, 2012) 156802.
- [144] V. Sorkin and Y. W. Zhang, “Mechanical properties of phosphorene nanotubes: a density functional tight-binding study,” *Nanotechnology* **27** no. 39, (2016) 395701.
- [145] Z. et al., “Phosphorene nanoribbon as a promising candidate for thermoelectric applications,” *Sci. Rep.* **4** no. 6452, (2014) 1.
- [146] B. Sa, Y.-L. Li, J. Qi, R. Ahuja, and Z. Sun, “Strain engineering for phosphorene: The potential application as a photocatalyst,” *The Journal of Physical Chemistry C* **118** no. 46, (2014) 26560–26568.
- [147] H. Guo, N. Lu, J. Dai, X. Wu, and X. C. Zeng, “Phosphorene nanoribbons, phosphorus nanotubes, and van der waals multilayers,” *The Journal of Physical Chemistry C* **118** no. 25, (2014) 14051–14059.
- [148] A. Carvalho, A. S. Rodin, and A. H. C. Neto, “Phosphorene nanoribbons,” *EPL (Europhysics Letters)* **108** no. 4, (2014) 47005.
- [149] B. Ding, W. Chen, Z. Tang, and J. Zhang, “Tuning phosphorene nanoribbon electronic structure through edge oxidization,” *The Journal of Physical Chemistry C* **120** no. 4, (2016) 2149–2158.